A Modelling Workflow for Seismic Characterization of Paleokarst Reservoirs

by
Martin Kyrkjebø Johansen

Master of Science Thesis in
Petroleum Geoscience

Department of Earth Science
University of Bergen

November 2018

Abstract

Karst is a type of landscape formed by dissolution of soluble rocks such as carbonates. Caves are common subsurface karst features and develop where water percolates through the host rock and creates cave-passages through dissolution. With time and burial, the cave-passages may collapse or fill in with sediments, but drill bit-drops indicating open cavities have been registered at large depths (up to 5 km).

This type of reservoir has the potential of containing substantial hydrocarbon accumulations. The complexity of these carbonate paleokarst reservoirs makes it very difficult for interpreters to identify any clear characteristics in seismic sections. Therefore, a thorough investigation is needed to establish a guideline to help interpreters knowing what characteristics to look for and what they represent in terms of "real" geology.

By performing seismic forward modelling of a paleokarst system, an understanding of the seismic of these types of reservoirs can be achieved. The representation of a paleokarst system can be obtained by building models from good paleokarst outcrops, from modern active cave systems or by developing generic models. To account for the range of heterogeneities common in paleokarst reservoirs, an implementation of a suitable rock physics model to compute the elastic properties, is essential. A sensitivity study of modelled seismic images with respect to various petrophysical conditions is best obtained by using an effective and robust modelling approach. A suitable option for such efficient seismic modelling approach is a Point-Spread Function based 2(3)D convolution method which is applied to the whole input model at once and has more realistic illumination and resolution effects compared to the standard 1D convolution method.

This study demonstrates a modelling workflow relevant for seismic characterization of paleokarst reservoirs. The input models used in this work consist of an outcrop-based 2D model of a paleokarst structure located in the Franklin Mountains, Texas, and a 3D reservoir model representing a modern cave system called the Setergrotta cave, which is located near Mo i Rana, Norway.

The comparison between different rock physics parameters added to the paleokarst models indicated that the pore geometry has a major influence on the seismic velocity, especially in low-porosity cases. The seismic forward modelling approach proved to be efficient and convenient in terms of providing sufficiently realistic seismic images, and therefore providing a good approach for testing and comparing various paleokarst reservoir conditions.

Acknowledgements

First of all, I would like to express my gratitude to my main supervisor Isabelle Lecomte for guidance, discussions and encouragement during the time working on my master thesis, it has been highly appreciated. I would also like to thank my co-supervisors Jan Tveranger (NORCE) and Åsmund Drottning (Rock Physics Technology) for discussions and feedback on my thesis. Also, thank you to Bjarte Lønøy for great inputs on the paleokarst part.

Thanks to FOPAK research group ("Forecasting of architecture, seismic characteristics and flow behaviour in paleokarst reservoirs"; PETROMAKS2 project 267634; Research Council of Norway; for funding this master project and providing the Setergrotta model). Also, thanks to NORSAR Innovation AS for the academic license for the SeisRoX software, and to Rock Physics Technology for providing the rock physics modelling programme, ENTER.

A special thanks to my fellow geophysics students at the University of Bergen for good times and great memories. Without you, this would not have been possible. Also, a big thanks to the guys at Grotten for encouragement, meaningful discussions and good sense of humour for the last couple of months.

At last, I would like to say thank you to my family and friends, specially my parents for continuous support and encouragement.

Contents

List of Figures

List of Tables

List of Abbreviations

AI	*Acoustic Impedance*
AVO	*Amplitude Versus Offset*
CCT	*Contact Cement Theory*
DEM	*Differential Effective Medium*
FOPAK	*Forecasting of Architecture, Seismic Characteristics and Flow Behaviour in Paleokarst Reservoirs*
FT	*Fourier Transform*
GMS	*Great McKelligon Sag*
HSUB	*Hashin-Shtrikman Upper Bound*
PSDM	*Prestack Depth Migration*
PSF	*Point-Spread Function*
RP	*Rock Physics*
S/N	*Signal-to-Noise*
SR	*Source-Receiver*

Chapter 1

Introduction

1.1 Motivation

Carbonate paleokarst reservoirs are relatively common globally (e.g. Middle East, USA, Southeast Asia), but have not been found on the Norwegian continental shelf until recently (Elvebakk et al., 2003; Hunt et al., 2003; Sayago et al., 2012; Stemmerik et al., 1999). Considerably large discoveries were made by Lundin Norway AS at the Gotha and Alta prospects at Loppa High, in the Barents Sea. They can potentially be the first producing oil-fields from paleokarst reservoirs, on the Norwegian continental shelf.

Carbonate rocks can be affected by karstification, which means that rocks such as limestone and dolomite dissolve after influence of aggressive carbon dioxide (CO_2)-saturated water and characteristic features such as caves, dolines (sinkholes) and karst towers (figure 1.1-1), can dominate the carbonate formation (Ford and Williams, 2013). The term paleokarst is used for the karst features that no longer are connected to any active karst processes (Loucks, 1999). These types of formations can potentially contain a high amount of hydrocarbon deposits.

Meter-scale bit-drops have been registered at several kilometers depths, which indicates cavities (Loucks, 1999). However, in most cases the caves have been subjected to high overburden pressure due to burial and the cave ceiling has collapsed, and the caves are filled with collapse material. The potential of these types of reservoirs is high, but they are very complex and difficult to interpret. Because of the high seismic velocity in carbonate rocks, compared to siliciclastic rocks, the horizontal and vertical seismic resolution are low (Janson and Fomel, 2011). The complexity of carbonate rocks is a result of the variety of the deposition processes with early cementation and the subsequent alterations by dissolution and diagenesis.

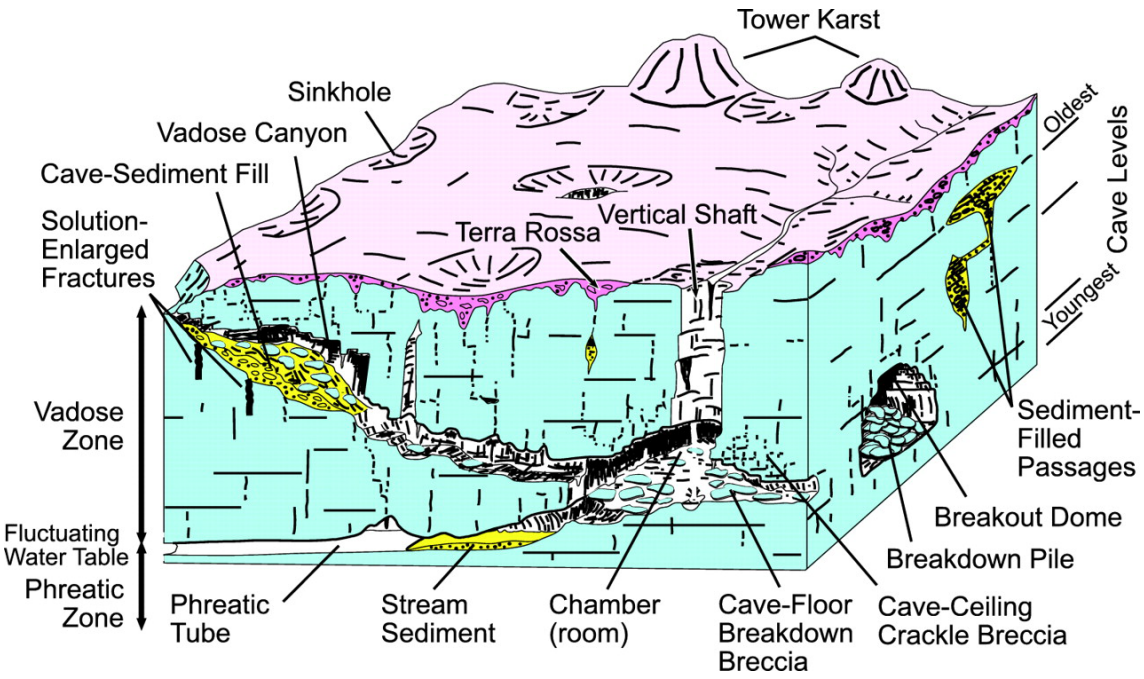

Figure 1.1-1: *Several types of karst features that may occur in carbonate rocks (Zeng et al., 2011a).*

These factors of deposition and subsequent alterations will also affect the pores in terms of shape and size. Compared with siliciclastic rocks, which mainly have one pore type, carbonate rocks have a variety of different pore types (Xu and Payne, 2009). The dissolution (karstification) of carbonate rocks will affect the size of these pores, which then may vary from small microcracks to large cave-features. Predicting the spatial distribution of the different porosity types is a key problem for reservoir characterization aimed at forecasting production behaviour.

The variety in pore geometry and size will affect the seismic and petrophysical properties. In carbonate rock physics, the pore shape appears to be the most dominant factor for controlling acoustic properties, such as P-wave velocity, where this can change as much as 40% due to pore type for a given porosity (Xu and Payne, 2009). Due to the heterogeneities in carbonate rocks, finding a suitable rock physics model can be challenging, especially for the karstified carbonate features.

Another challenge is the interpretation of seismic data gathered from an area with a complex geology such as paleokarst. One way of dealing with this challenge, is to make realistic models of known examples of karst features and then do seismic forward modelling to generate synthetic seismic. By comparing the model with the synthetic seismic, seismic characteristics of the different geological features can be established. These characteristics from synthetic seismic data can then be compared with real seismic data to try to find similarities. The model can then be modified

such that the synthetic seismic simulates the real seismic data (Kearey et al., 2013).

The process of making these synthetic seismic models, includes adding and varying the model parameters in a systematic manner to look at what impact the changes will have on the output seismic response. Variation of the petrophysical properties (fluid-type and saturation, porosity, permeability, pore-type, mineralogy etc.) can have a significant impact on the seismic response.

1.2 Aim of study

Because of the high lateral and vertical heterogeneity in paleokarst reservoirs, correlation between well-data will not determine production forecast as well as it does for siliciclastic reservoirs. Therefore, the mapping of such complex structures is mostly based on seismic data. The complexity will however make the interpretation of the seismic data challenging. Today, there are very few guidelines for identifying paleokarst structures in seismic data.

The aim of this study is to present a modelling workflow for seismic characterization of paleokarst reservoirs, which could potentially provide interpreters with a tool to establish guidelines on how to recognize paleokarst structures in seismic data. Both geo-models replicating realistic paleokarst reservoir features (in terms of structures and petrophysical parameters), and a suitable set of rock physics models (specified for carbonates) are needed to get the right elastic properties in the models. The elastic properties will then be used to perform a seismic forward modelling. The present work will consist of investigating how the different model parameters may influence the seismic response, and how the seismic data will look for the specific geological setting. The SeisRoX modelling software from the NORSAR Software Suite 2018 will be used to perform the seismic forward modelling.

SeisRoX uses a simple but efficient seismic modelling method. The modelling process is based on Fast Fourier Transform and 2(3)D convolution between the geological model and a point-spread function (PSF), which basically is a migration signature of a point scatterer. The PSF is defined by its source-receiver pair configurations and the background model (Lecomte, 2008). Such PSF-based modelling will allow you to include more complete resolution and illumination effects than what the 1D convolution approach would do.

Chapter 2

Carbonates and Karst

2.1 Carbonates

Calcite ($CaCO_3$), dolomite ($CaMg(CO_3)_2$) ($CaCO_3$) and aragonite ($CaCO_3$) are the most common carbonate minerals. There are two types of carbonate sedimentary rocks based on mineralogy, which are limestone and dolomite. Limestones consist mainly of calcite, while dolomites consist mainly of dolomite minerals (Boggs, 2006).

Figure 2.1-1: *Biochemical limestone with shell fragments (Fossen, 2008).*

2.2 Depositional environment

Carbonate sediments originate from both biological and chemical processes (Boggs, 2006). Organic carbonate production involves different kinds of processes, such as organisms extracting $CaCO_3$ for skeletal growth and later when these organisms die, the remains will be deposited as carbonate material (Boggs, 2006). Also, processes involving reduction of the amount of CO_2 in the water, such as photosynthetic activities in the shallow parts, will lead to $CaCO_3$ precipitation (Boggs, 2006). Inorganic processes where $CaCO_3$ are precipitated directly from seawater can occur, but this process is often assisted by organic processes (Boggs, 2006). Conditions like high temperature, lower water pressure and decreasing salinity enhance the $CaCO_3$ precipitation (Boggs, 2006).

The carbonate production is dependent on what kind of environment the sediments are produced in. The production is high in warm, clear tropical waters, where the carbonate producers thrive (Moore, 2001). Carbonate production is also possible in cold waters. In these areas, organisms like molluscs, bryozoa, foraminifers and barnacles support the carbonate production, but also through settling of pelagic particles above the carbonate compensation depth (CCD) (Coe, 2003). The CCD is the water depth (between 3500-5500 m) where the rate of dissolution of $CaCO_3$ equals the supply of $CaCO_3$ (Boggs, 2006).

Carbonate deposits initially exhibit a very wide range of porosity types in terms of size and shape, which is closely linked to depositional facies (Lønøy, 2006). These depositional facies may vary due to different depositional environment. Based on how the carbonate production processes occur and where the sediments are deposited, will influence texture, porosity, permeability and therefore also controls carbonate reservoir potential (Wilson, 1975).

2.3 Diagenesis

Diagenesis is used as a term for post-depositional alterations of sediments. Broadly speaking it involves compaction, dissolution and cementation. Diagenesis will cause changes in porosity, mineralogy and chemical composition in carbonate sediments (Lucia, 1992). Diagenesis will differ depending on whether it occurs in a marine, meteoric or subsurface regime (Boggs, 2006). The different regimes are illustrated in figure 2.3-1.

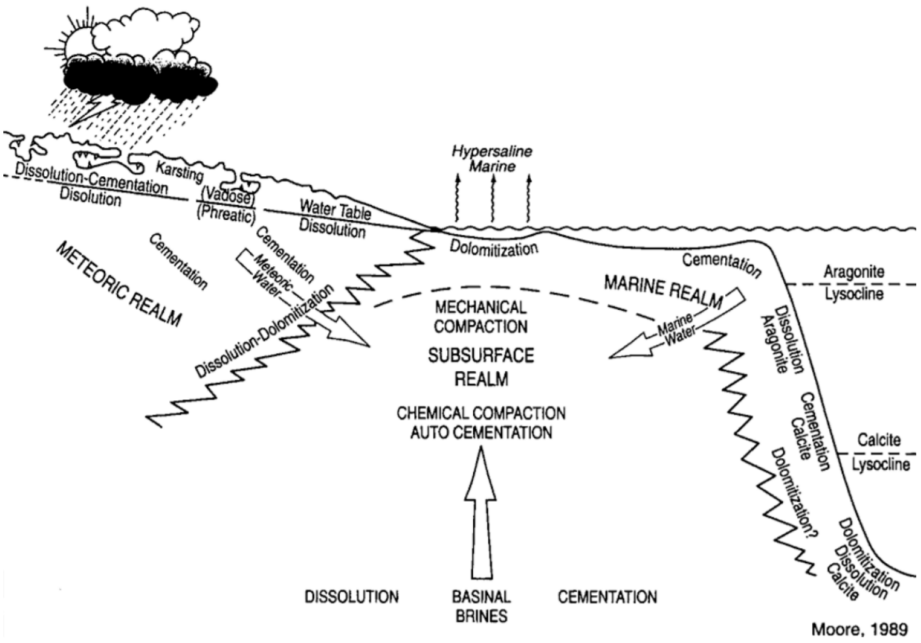

Figure 2.3-1: *Different diagenetic processes occurring in different regimes (Moore, 2001).*

The marine diagenetic regime is located near or on the surface of the seafloor (Boggs, 2006). Dependent on the depositional environment of the sediments, circulating water in the sediment pore system in this area is generally supersaturated with carbonate minerals and enhancing cementation between carbonate grains, which leads to a decrease in porosity (Moore, 2001). Bioturbation (which means reworking of sediments by organisms) and modification of carbonate shells are also diagenetic processes associated with the marine regime (Boggs, 2006).

The meteoric diagenetic regime is located near-surface or at the surface and the carbonate rocks that are influenced in this regime, originate from the marine regime (Boggs, 2006). Meteoric water typically has a high concentration of dissolved CO_2, which will enhance the dissolution process of the carbonate rocks (Boggs, 2006). There are also factors that can make the meteoric water supersaturated, which will lead to precipitation of calcite cement, which may occur when both calcite and aragonite are present in the meteoric water (Moore, 2001). This means that both dissolution and cementation can occur in this diagenetic regime (Boggs, 2006).

The last diagenetic regime is the subsurface regime and occurs after the sediments are buried. In this regime, temperatures and pressures increase, and pore fluids change in composition (Boggs, 2006). The diagenetic processes that may dominate here are chemical and physical compaction, cementation and dissolution, but the exact processes that occur depend on the conditions of the burial environment, such

as temperature, pore-fluid composition and pH (Boggs, 2006).

Since the carbonate sediments consist of soluble material, they are more easily affected by some diagenetic processes compared to siliciclastic sediments, such as reduction of porosity by cementation between grain contacts. This leads to a low porosity of the carbonate rock. But because of the soluble nature of the carbonate material, secondary porosity may occur by dissolution of carbonate material in pore spaces and fractures. This effect will then again enhance the porosity and permeability of the carbonate rock.

Considerably higher dissolution of the carbonate rock may lead to larger cavities inside carbonate formations and may serve as good hydrocarbon reservoirs. The features created by the heavier dissolution are called karst, which will be further explained in section 2.5.

2.4 Porosity and pore types

Carbonate rocks have a complex texture, where grains have different shapes and sizes due to the in-situ deposition, which will lead to a complex mixture of different types of pores. Diagenetic alterations will affect the pores, but they will still vary in terms of shape and size after diagenetic processes. The porosity can either be of primary or secondary origin based on how the pore-space was developed (Moore, 2001). Primary porosity is the porosity determined at sediment deposition, while secondary porosity is the porosity that develops a time after deposition (Moore, 2001).

Choquette and Pray (1970) developed a classification system on carbonate porosities. Their system was further developed by Lønøy (2006), which is largely used in the description of pore types presented in this section. The different porosity types are illustrated in figure 2.4-1.

Interparticle and intercrystalline porosities

Interparticle pores are spaces between particles, while intercrystalline pores are spaces between crystals. These types of porosities are mainly primary porosities, but porosities between crystals of secondary origin may occur (Lønøy, 2006).

Intraparticle and intracrystalline porosities

Intraparticle and intracrystalline porosities occurs within grains and crystals. These pore types are characteristic for carbonate rocks and are not found in siliciclastic rocks (Moore, 2001). This type of porosity could be developed by primary porosity,

where primary intraparticle/ intracrystalline porosity is mainly from small chambers inside carbonate material, or be developed through decay of organic material in carbonate skeletons (Lønøy, 2006).

Moldic porosities

Moldic porosity is developed by selective, complete or partial dissolution and recrystallization of carbonate constituent and is developed as a secondary porosity (Lønøy, 2006).

Vuggy porosities

Vuggy pores are large not-fabric selective pores (pores that have cut through cement boundaries) and are usually developed by enlarging fabric selective pores (pores with no connectivity) through dissolution, such as moldic pores (Lønøy, 2006).

Channel porosities

Channel porosities are of secondary origin and may be created by dissolution along fractures.

Cavernous porosities

Cavernous porosities are much larger versions of channel and vuggy pores.

Framework and fenestral porosities

Framework porosity is of primary origin and is developed through the deposition of frame-builders in reef environment such as corals, coralline algae or sponges (Moore, 2001). Fenestral porosities are related to larger openings than inter-grain openings and are basically of secondary origin. They are created by decay of sediment-covered algal mats and after accumulation of pockets of gas or water (Wang, 1997).

Fracture porosities

Because carbonate rocks are very brittle, they will fracture due to higher pressures and fracture porosity occurs.

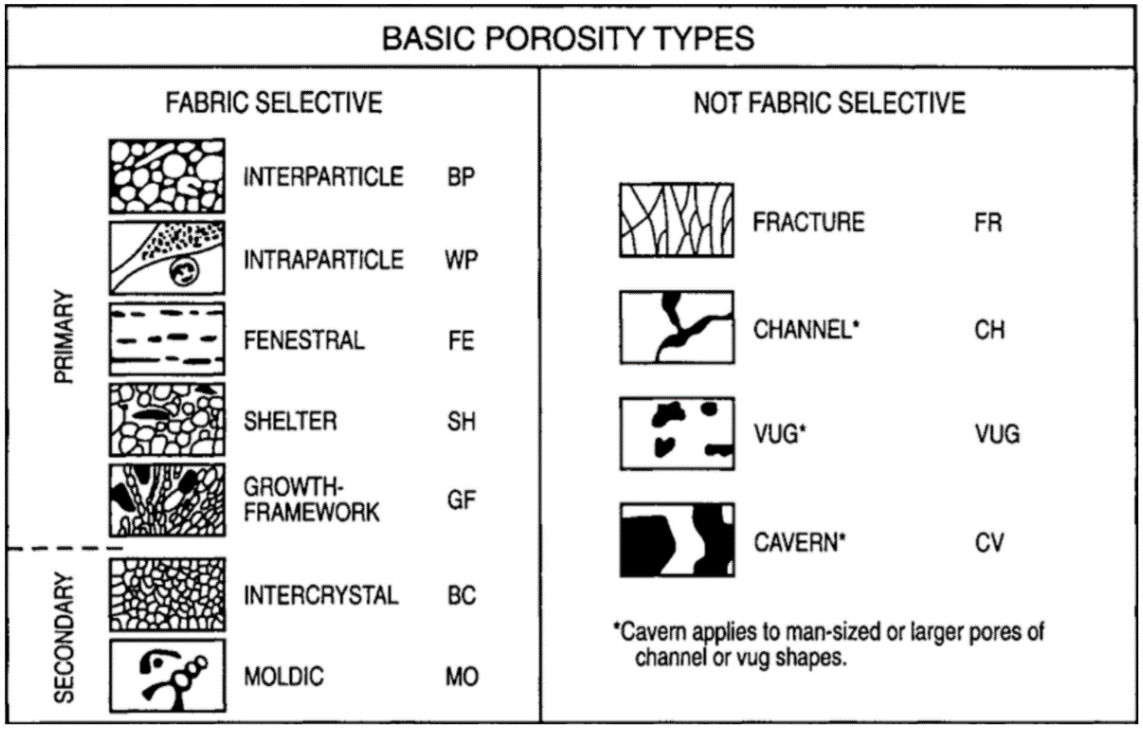

Figure 2.4-1: *Different types of porosity that may occur in carbonate rocks (Moore, 2001).*

2.5 Karst

Karst is defined by Ford and Williams (2013) as "...a special style of landscape containing caves and extensive underground water systems that is developed on especially soluble rocks..." (p. 1). Soluble rocks such as carbonate rocks and evaporites can therefore develop karst features. In this thesis the focus will be on karst development in carbonate rocks.

Figure 2.5-1: *Exposed karstified limestone showing cavities. Both karst development along permeable beds (horizontal) and along fractures (vertical features) are displayed in the photo (Setså, 2018).*

Karst development occurs when carbonate rocks dissolve by the influence of aggressive water. Continental karst development is influenced by water containing dissolved carbon dioxide (CO_2), where the CO_2 originates from the released CO_2 when organic matter decay in the soil (Ford and Williams, 2013). The meteoric water (rainwater) moves further down through the soil and into fractures or along faults in the carbonate rock (Ford and Williams, 2013). This water will over time create cavities along these fractures or faults that can result in extensive karst-networks that cover large subsurface areas (Loucks, 1999). When a cave conduit has developed a diameter of 5-11 mm, the water flowing through is able to transport sediment, and the conduit is regarded as a true cave conduit (Loucks, 1999).

In marine coastal conditions, a subsurface mixing of marine and meteoric freshwater will result in what are called "flank margin caves" (Mylroie and Carew, 1990). The

geometries of these caves is distinctly different from network-type caves developed by meteoric water.

Cave passages can be divided into several types based on their geometry and on their development history. If the cave development occurs below or at the water table, the dissolution will be the same in every direction inside the conduit and the shape of the conduit is hydraulically controlled (Lauritzen and Lundberg, 2000). This zone is called the phreatic zone and the conduits can be called phreatic tubes or conduits.

If further cave development occurs above the water table, the dissolution will be unidirectional (one direction) downwards and therefore controlled by gravity (Lauritzen and Lundberg, 2000). This zone is called the vadose zone and canyon formations are typical for this zone (Lauritzen and Lundberg, 2000). Both the phreatic and vadose zones are illustrated in figure 1.1-1 in chapter 1.

During the development of a cave passage, there are many factors to be aware of, e.g. several changes in the water table position as well as the amount of cave sediment deposits and distribution inside the cave passage. This causes a dynamic development environment for the cave passages and will influence the shape of the cave (figure 2.5-2).

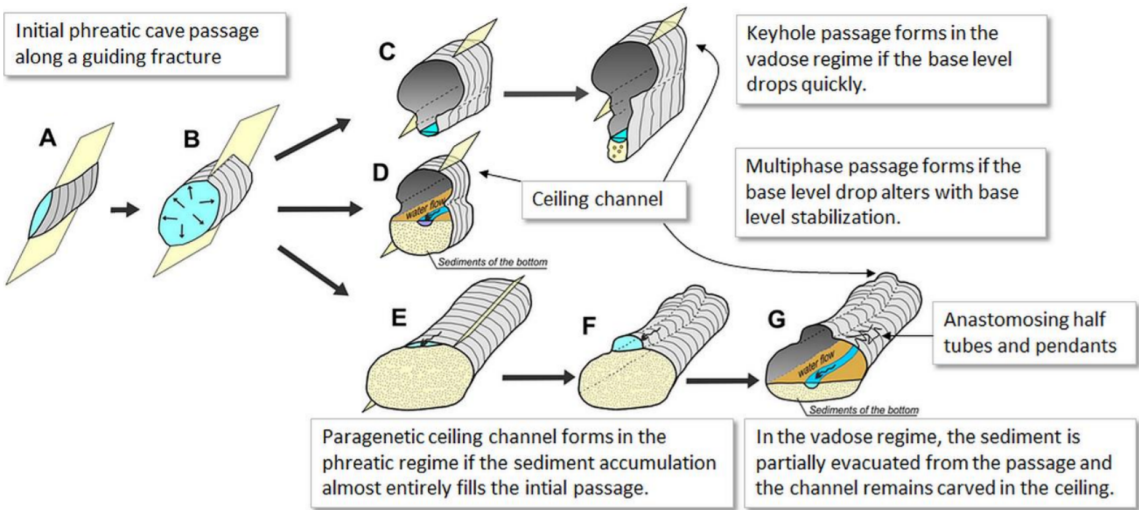

Figure 2.5-2: *Illustration of how the different cave passages may be formed due to changes in the water table position and amount of cave sediment deposits inside the cave passage (Gallay et al., 2016).*

The karst development does not only affect the subsurface, but will also influence the landscape at the surface. Common karst features in karst landscapes are dolines (sinkhole), karst towers, karren, disappearing streams (vertical shafts) and upcoming cave-springs (figure 1.1-1 in chapter 1 shows some of these features).

2.6 Paleokarst

Paleokarst is defined as karst that no longer is related to any active karst processes (Loucks, 1999). When inactive karst features are buried, the overburden pressure increases, which usually result in a collapsing of the cave. At what depth this collapse occurs, depends on the ceiling span of a cave passage, and the strength and thickness of the overlying strata (Ford and Williams, 2013; Loucks, 1999).

As the cave passage is subjected to the overburden pressure, a tension dome will form above the cave passage (figure 2.6-1) (Ford and Williams, 2013). The rocks in this area are subjected to maximum tension and sagging of the overlying strata occurs due to the overlying weight (Ford and Williams, 2013). When the tension reaches a certain level, the ceiling and some of the cave walls collapse causing a relief of stress. This will result in a breakout dome over the cave passage (see figure 2.7-2 and fig 1.1-1) (Loucks, 1999).

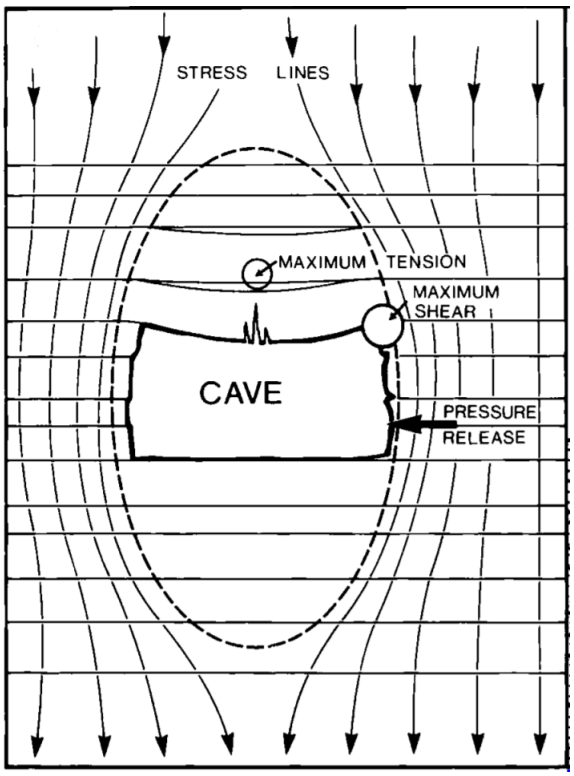

Figure 2.6-1: *The figure shows the distribution of stress around a buried paleocave and where the maximum tension and shear stress are located. It also shows how the overlying strata develops a sag-feature over the cave passage due to the overlying weight (Ford and Williams, 2013).*

As the ceiling starts to collapse, the breakdown collapse material will accumulate

at the bottom of the cave passage. The breakdown of the cave ceiling stops if the collapse material completely clogs the cave passage (figure 2.6-2a) (Ford and Williams, 2013).

The collapse material will fill up the entire cave passage because the volume of the breakdown material will be larger than the volume of the pre-collapse formation rock, unless there is a simultaneous removal mechanism of the breakdown material at the bottom of the cave such as a subsurface stream (Ford and Williams, 2013). If there is removal, the collapse process continues upwards, creating a breccia pipe. The process continues until the subsurface stream stops transporting breakdown material away from the cave-floor or if the breccia pipe reaches the surface creating a collapse doline (figure 2.6-2b) (James and Choquette, 1988).

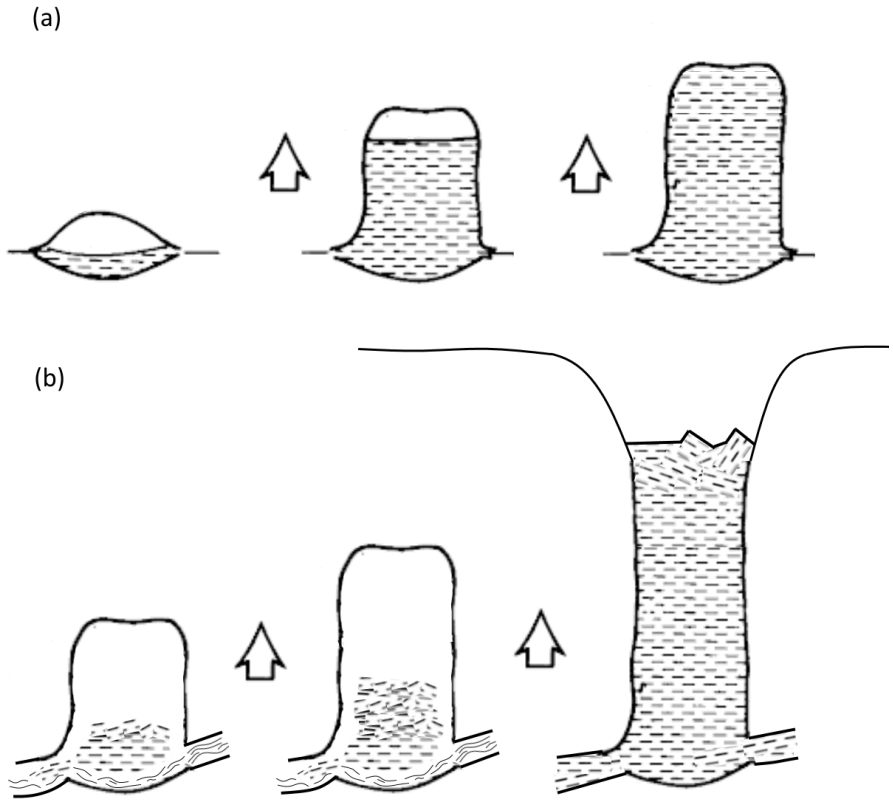

Figure 2.6-2: *Initial elliptical cave-passage developing to be either (a) filled with collapse material which stops the collapse process, or (b) there is a removal of the breakdown material which leads the collapse process to continue upwards until it reaches the surface. Modified from James and Choquette (1988).*

The collapse of a deeply buried paleocave will lead to an increased area with fractures

and crackle breccia surrounding the collapsed cave passage. A paleocave system containing several cave passages, which are closely spaced, can develop fractures caused by collapse and tectonic activities. These fractures may connect the different cave passages and cause high permeability between them (Loucks, 1999).

2.7 Cave-sediment and collapse material

As caves collapse, breakdown material will accumulate on the cave floor and may continue until the cave passage is completely filled with collapse material. The breakdown materials inside the cave consist of chaotic distributed and oriented breccias of different sizes, cave-ceiling and cave-wall crackle breccias and a combination of chaotic and crackle breccia called mosaic breccia (figure 2.7-1) (Loucks, 1999).

Sediments transported by flowing water from outside the cave conduits, can be a part of the facies inside a collapsed paleocave (White and White, 1969). Sediment fills may occur at any stage of cave facies, and can therefore be deposit at the bottom of the cave, in between breccias and on top of the chaotic breccias, but restricted to the pre-collapse cave area (Loucks, 1999). It is therefore difficult to describe one specific vertical sequence of collapse material and sediment fill in a collapsed cave.

As paleocave passages are buried deeper, the cave passages are subjected to extensive mechanical compaction which cause further collapse and the existing collapse material and cave sediments are re-brecciated and packed more closely together (figure 2.7-2) (Loucks, 1999). Coarse interbreccia pores and cavities decrease with burial-related mechanical compaction, while fine interbreccia pores, fractures and crackle breccia increase with deeper burial (Loucks, 1999). Intensive compaction may in some cases cause pressure-solution between contacts, which lead to a porosity reduction (Loucks, 1999).

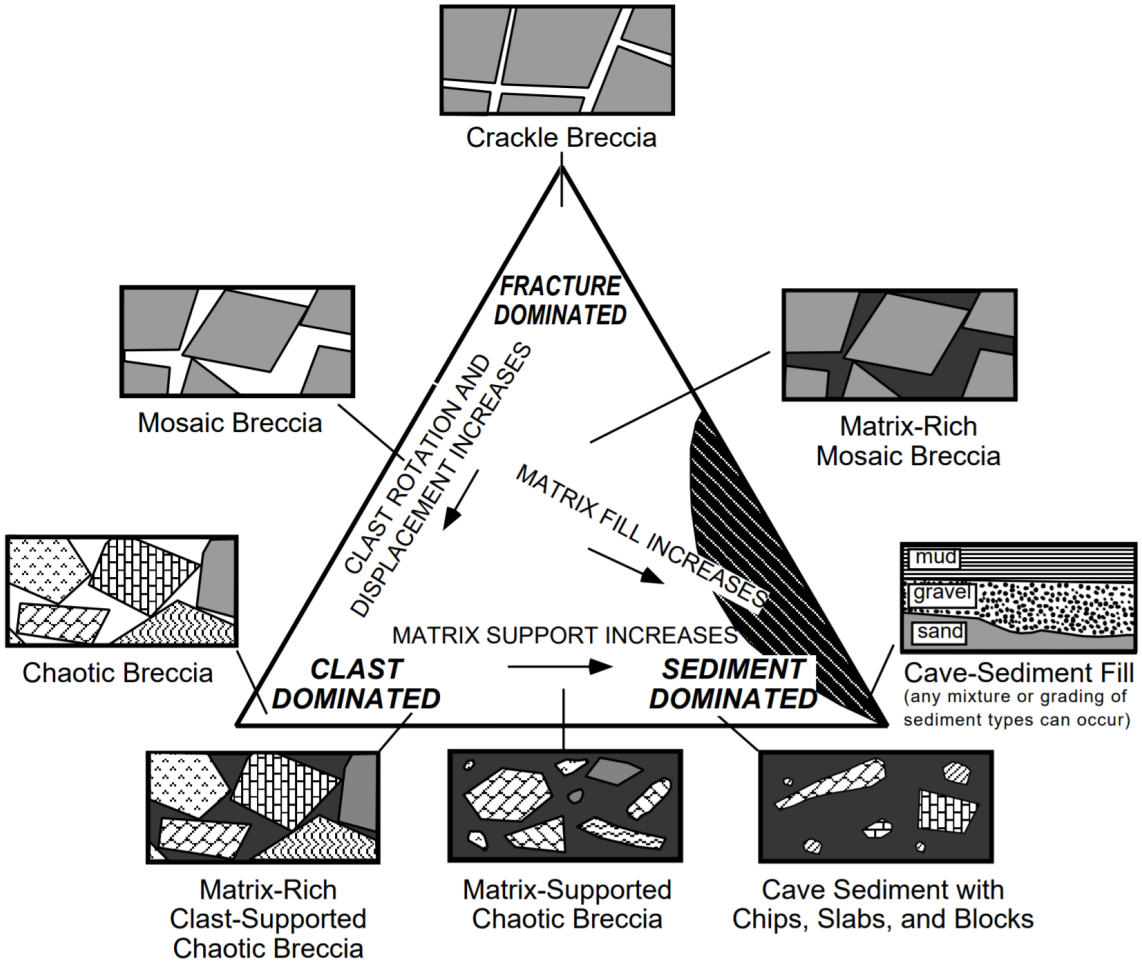

Figure 2.7-1: *Classification diagram of cave deposits and breccias and the relationship between three basic end members crackle breccia, chaotic breccia and cave sediment. Crackle breccias are highly fractured rocks in cave ceilings and cave walls and are a result of stress relief in surrounding strata. Chaotic breccias have been subjected to extensive rotation and displacement and may consist of clasts from more than one source. Cave sediments may vary in size and origin and can fill passages or interbreccia pores in the different breccia types and form a matrix-rich breccia (Loucks, 1999).*

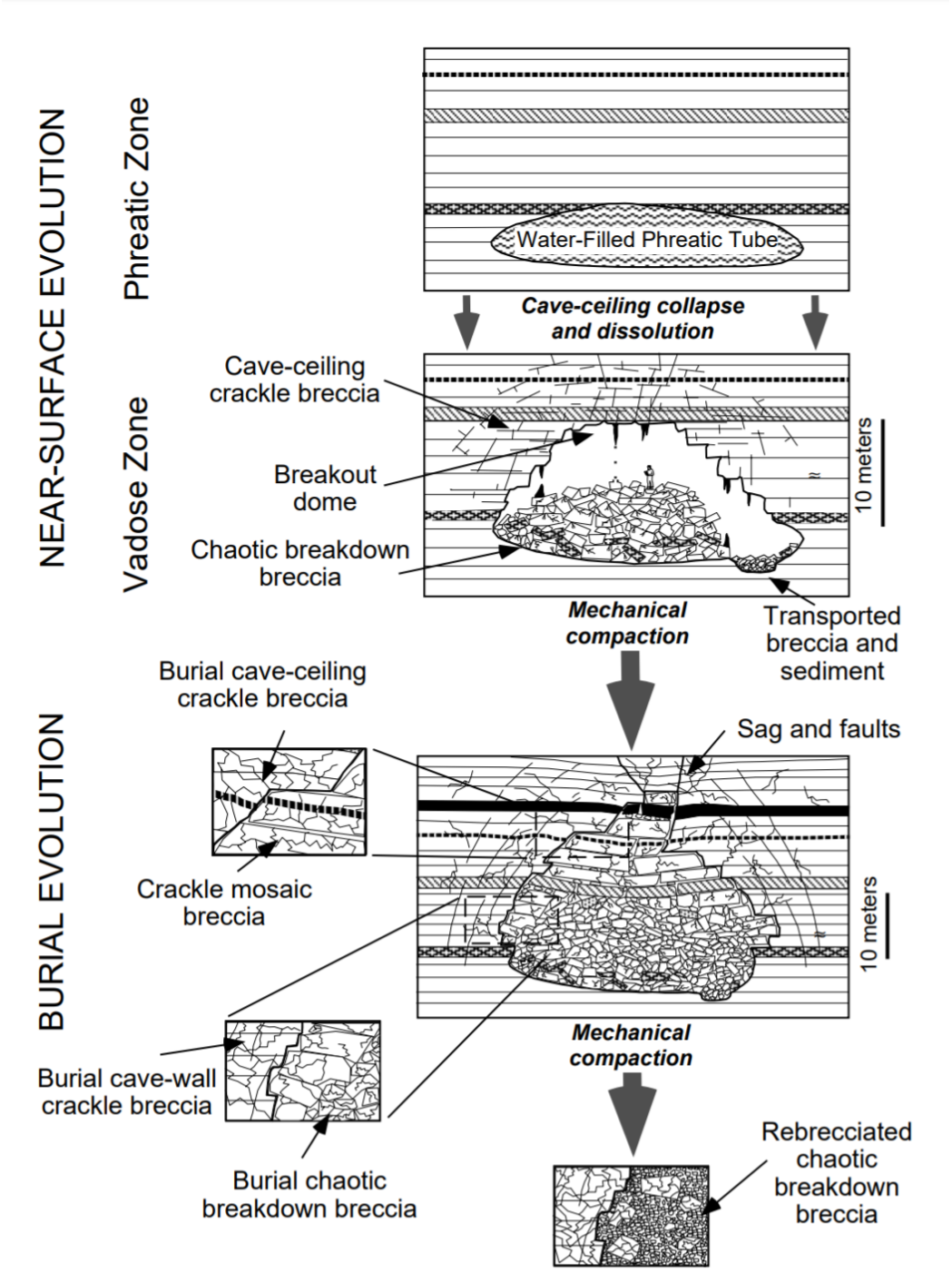

Figure 2.7-2: *An example of how an initial phreatic tube developed near-surface, may evolve as it is subjected to burial processes leading to collapse of the cave passage. Further burial leads to re-brecciation of the collapse material as it is subjected to mechanical compaction due to the overburden pressure (Loucks, 1999).*

2.8 Paleokarst reservoirs

Paleokarst systems as petroleum reservoirs, are an important class within carbonate related petroluem reservoirs and can contain a high amount of petroleum accumulations. Paleokarst reservoirs may virtually occur in every carbonate reservoirs to varying extents, and can be found all over the world, such as the giant (onshore) Thamama field in the Middle East (Melville et al., 2004), the Tarim basin in China (Zeng et al., 2011a), the Permian Yates field in west Texas (Loucks, 1999), and at Loppa high in the Barents Sea (Sayago et al., 2012) to name a few.

The condition of paleokarst reservoirs may vary in terms of whether they are completely filled with collapse material or exhibit large cavities. As paleocave passages are subjected to burial processes, they will at some point collapse due to the overburden pressure. At what depth this collapse occurs, may vary over a broad depth range and in some cases, cavities may occur at thousands of meters depths (Loucks, 1999).

One way of recognising such cavities at large depths, is by registered bit-drops during drilling. Bit-drops of 7,5 meters between 1100 and 1280 meters depths (Madison reservoirs of the Garland field in Wyoming), bit-drops of 5 meters at 2600 meters depth (Fusselman section in Dollarhide field in west Texas) and a drop of drill string at a depth of approximately 5800 meters (Silurian reservoir at Crittendon field in west Texas) have been registered in different paleokarst reservoirs (Loucks, 1999). Hydrocarbon reservoirs located in shallower paleokarst systems are dominated by cavernous, interbreccia and fracture porosity, while more deeply buried paleokarst reservoirs mainly consist of crackle breccia and fracture porosity (Loucks, 1999).

The buried paleokarst systems have a complex development-history where many stages from near-surface development, to stages of modification and later burial, collapse and compaction will produce complex reservoir conditions with a high degree of spatial heterogeneity (Sayago et al., 2012). This spatial complexity, both on a local (pore-type) level and regional level, make interpretation and quantification difficult in hydrocarbon exploration (Loucks, 1999). Therefore, an understanding of this type of reservoir is key to better predict reservoir potential and forecasting reservoir behaviour (Sayago et al., 2012). This may be dependent on factors, such as the degree of tight cemented zones and the connectivity (fracture-networks) between paleokarst features exhibiting hydrocarbon accumulations.

Chapter 3

Geophysical considerations and Rock Physics modelling

3.1 Geophysics in paleokarst

The complexity of paleokarst reservoirs makes seismic imaging and interpretation a challenging task. Therefore, a suitable rock physics model is crucial to get correct seismic velocities when performing a seismic forward modelling. Not all rock physics models are suitable for these types of heterogeneities, and the model should specifically take rock physics properties for karstified carbonate rocks into consideration. Porosity may vary from small cracks to large cavities on small lateral and vertical distances; the pores may have a large variation in shapes and there is usually no consistent relationship between porosity and permeability (Ringrose and Bentley, 2015). These types of challenges are typical for carbonate rocks.

The seismic velocities in carbonates are very high (e.g., 6100 m/s in limestone host rock (Zeng et al., 2011b)), but may vary due to properties such as pore shape, which appears to be the most dominant factor in carbonate rock physics, where the pore-type can cause a huge variation in P-wave velocity (Xu and Payne, 2009). The high seismic velocity and seismic attenuation cause a poor seismic resolution and for features in deep subsurface, where lower frequencies must be used because the high frequencies will attenuate in short distances, the resolution is really poor.

Seismic is essentially imaging rapid variations (contrasts) of acoustic/elastic impedance, which is described by the product of seismic velocity and density. The transition from a layer with low velocity and density, e.g. shale, to a carbonate layer with a considerably higher velocity and density, will be displayed as a high-amplitude event in the seismic data, due to a high reflection coefficient. However, transitions between

different carbonate strata are relatively weak in seismic (Decker et al., 2015).

Paleocave reservoir features are usually represented by high amplitude contrasts in the seismic data. These seismic contrasts representing the collapsed paleocave features will not be coherent, but more chaotic and associated with faults (Zeng et al., 2011b). Also, paleokarst features may enhance or destroy impedance contrasts within a stratigraphic architecture (Janson and Fomel, 2011).

The elements mentioned above are typical for collapsed paleocaves, where high-amplitude contrasts (bright spots) and faults represent the chaotic breccia and the higher porosities inside the paleocaves. Sag-features are also detectable in the seismic located above collapsed passages as explained in section 2.7 in chapter 2. As some of the different geophysical terms mentioned above may not be familiar to everyone, they will be further explained in the next few sections.

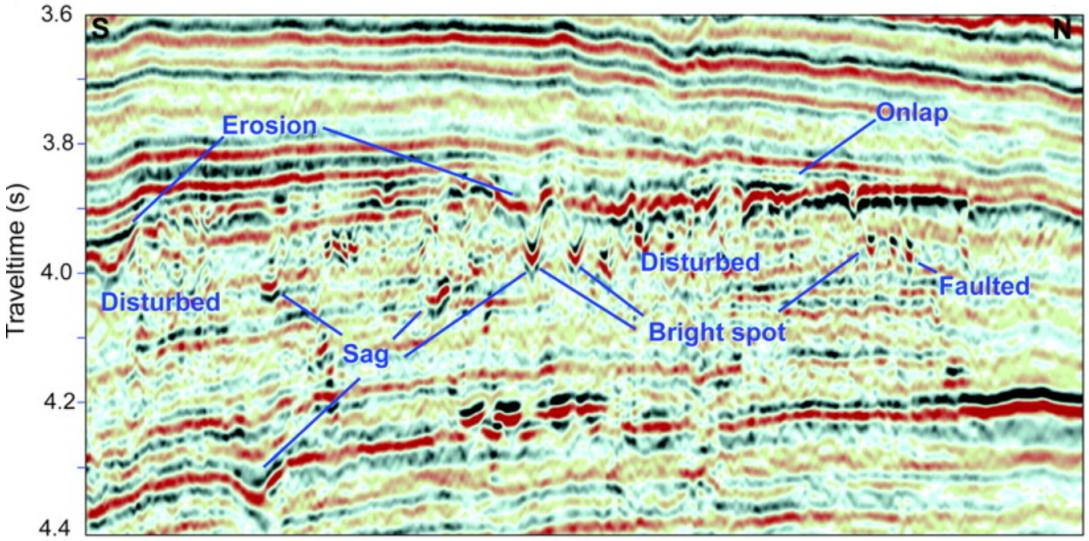

Figure 3.1-1: *A seismic section which includes paleokarst characteristics where some interpretation have been done based on some of the seismic anomalies (Zeng et al., 2011b).*

3.2 Seismic velocities

Seismic velocity represents the velocity of a seismic wave (elastic wave) moving through an elastic medium. In seismic, both compressional waves (P-waves) and shear waves (S-waves) are considered, for that reason the velocities used are called P-wave velocity and S-wave velocity. P-waves are waves that propagate through

the elastic medium by compressional and dilational strains in the direction of propagation (figure 3.2-1a) (Kearey et al., 2013). S-waves are waves that propagate through the elastic medium by pure shear strain perpendicular to the direction of propagation (figure 3.2-1b) (Kearey et al., 2013).

The compressional nature of a P-wave makes it capable of propagating through all material, whereas for a S-wave only shear takes place, meaning it can only propagate through solid material and therefore not through fluids. The velocity of a P-wave, v_p, is described by:

$$v_p = \sqrt{\frac{K + \frac{4}{3}\mu}{\rho}} \tag{3.1}$$

where K is the bulk modulus, μ is the shear modulus and ρ is the density. The S-wave velocity, v_s is described by:

$$v_s = \sqrt{\frac{\mu}{\rho}} \tag{3.2}$$

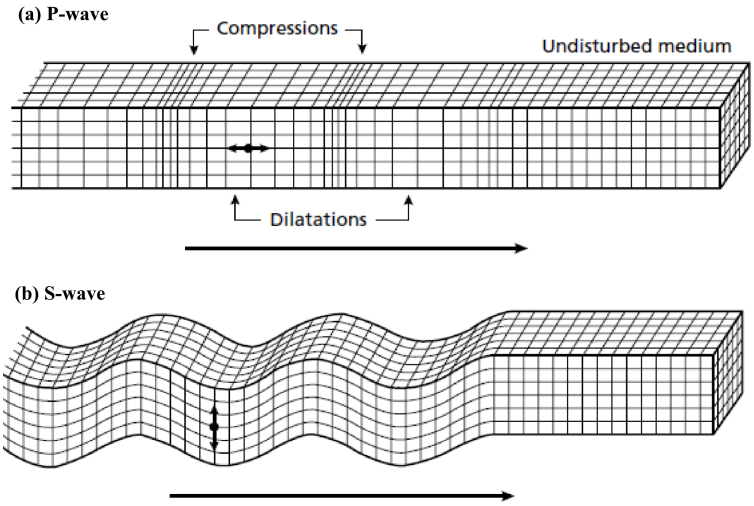

Figure 3.2-1: *Elastic deformations and particle motions of (a) a compressional body wave (P-wave) and (b) a shear body wave (S-wave) (Kearey et al., 2013).*

From the equations above, one can assume that P-waves will always be faster than S-waves when considering propagation through the same elastic medium. The density, ρ, in both equations is described by:

$$\rho = \frac{M}{V} \tag{3.3}$$

where M is the mass of the rock and V is the volume of the rock.

3.3 Seismic reflections

When a seismic wave hits an interface between two layers of different physical properties, the energy of the seismic wave is partitioned into reflected and transmitted waves (figure 3.3-1) (Kearey et al., 2013). The partition of seismic energy at an interface is described by an impedance contrast. Since only normal incidence cases will be considered in this study, the following description of the impedance contrast (reflectivity) will be constrained to only concern acoustic impedance (AI) contrasts, described by P-wave velocities for normal incidence cases, though it is important to have in mind the effect of non-zero incidence cases, where the S-wave velocity will have an effect on the reflectivity. The AI is defined as the product of density (ρ) and seismic velocity (v) of the rock:

$$AI = \rho v \tag{3.4}$$

The higher the contrast in AI at an interface, the higher portion of the energy is reflected, and therefore less is being transmitted (Kearey et al., 2013). The seismic reflection coefficient describes the amplitude of a reflected wave that has been partitioned at an interface. The reflection coefficient ($R0$) of a seismic wave, where normal incidence is considered, is defined as:

$$R0 = \frac{AI_2 - AI_1}{AI_2 + AI_1} \tag{3.5}$$

where AI_1 is the acoustic impedance in layer 1 and AI_2 is the acoustic impedance in layer 2 (figure 3.3-1). Since all the energy of an incident seismic wave is either reflected or transmitted at an interface, the sum of the amplitudes of a reflected and a transmitted wave equals the amplitude of the incident wave, and therefore the transmission coefficient (T) can be described as:

$$T = 1 - R0 = \frac{2AI_1}{AI_2 + AI_1} \tag{3.6}$$

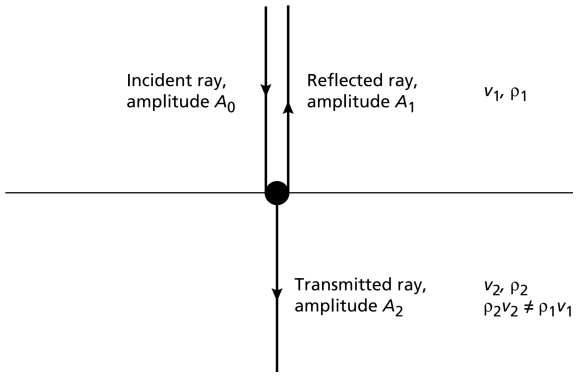

Figure 3.3-1: *Incident ray energy partitioned into a reflected and transmitted ray at an interface of acoustic impedance contrast (Kearey et al., 2013).*

3.4 Elastic moduli

Stress is a measure of the internal forces as an external force is applied on a material (Kearey et al., 2013). It can be divided into components of normal and shear stresses. The stress created by forces directed against each other, is called compressive stress, and tensile stress when forces are directed away from each other (Kearey et al., 2013). These are normal stresses and are called principal stresses which act along the three orthogonal axes (principle axes). If the magnitude of each principal stresses is equal, the stress is hydrostatic (Kearey et al., 2013). Shear stress occurs along all surfaces when the principal stresses are unequal. Shear stress does not occur in fluids, since fluids have no shear strength.

As the material is subjected to stress, a change of shape and/or size occurs (Kearey et al., 2013). This type of deformation is called strain. Stress and strain are proportional to each other up to a certain limit called the yielding point. The area up to the yielding point acts in accordance with Hooke's law of linear elasticity. Beyond the yielding point, the material acts in a plastic or ductile manner and the deformation caused by the applied force, is permanent (Gelius and Johansen, 2012). The area of linear elasticity represents very small deformations, such as deformation caused by seismic waves. These elastic deformations are reversible and do not cause any permanent damage to the material.

As seismic waves travel through a material, such infinitesimal small deformations occur along the path of the travelling wave. The bulk modulus or incompressibility (K) represents the stress-strain ratio of a simple case of hydrostatic pressure applied

on a material (figure 3.4-1a), and is defined as (Kearey et al., 2013):

$$K = \frac{volume\ stress\ P}{volume\ strain\ \frac{\Delta V}{V}} \tag{3.7}$$

where P is the hydrostatic pressure applied and $\frac{\Delta V}{V}$ represents the relative change in volume. The shear modulus or rigidity (μ) represents the ratio of the shear stress (τ) to the shear strain ($\tan\theta$) for a simple shear of a material (figure 3.4-1b) (Gelius and Johansen, 2012). The shear modulus acts for small deformation, and therefore the deformation occurring is reversible. The shear modulus is defined as:

$$\mu = \frac{shear\ stress\ \tau}{shear\ strain\ \tan\theta} \tag{3.8}$$

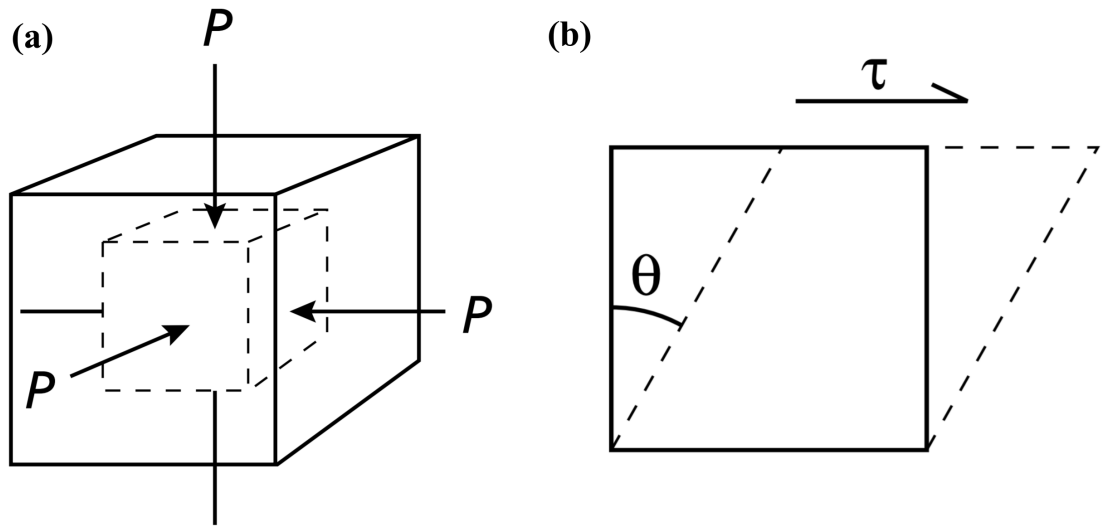

Figure 3.4-1: *(a) illustrates the incompressibility/bulk modulus, K, while (b) illustrates th rigidity/shear modulus, μ (Kearey et al., 2013).*

Effective elastic medium theory

Rocks usually consist of several types of minerals with different physical properties. Since most of the computation of rock properties are based on assumptions of a homogeneous isotropic medium, it is necessary to define a representative volume of a rock where the composition and structure are the same, and where this considered volume represents the whole rock (Gelius and Johansen, 2012; Smith et al., 2003).

For the approximation of effective elastic moduli, the geometrical distribution must be considered. Figure 3.4-2 shows how layers of different stiffness will be affected when they are vertically and horizontally layered (Gelius and Johansen, 2012).

Figure 3.4-2a shows an iso-stress case where the same stress is applied on all the layers, but there is a difference in strain between the hard and soft layers. Figure 3.4-2b shows an iso-strain case where the load applied causes the same amount of strain (Gelius and Johansen, 2012). The density is unaffected by the difference in geometrical distribution.

For effective elastic moduli approximation of an iso-stress case, the Reuss model computes the softest mixing model obtained from two materials (Gelius and Johansen, 2012), and is defined as:

$$M_{Reuss} = \left[\sum_{i=1}^{n} \frac{V_i}{M_i} \right]^{-1}, \tag{3.9}$$

where V_i is the volume fraction of each constituent and M_i is the elastic moduli of the different components. The Voigt model represents the stiffest mixing model and is used for an iso-strain case:

$$M_{Voigt} = \left[\sum_{i=1}^{n} V_i M_i \right]. \tag{3.10}$$

When the stress and strain conditions of a medium are not known, an average of the Voigt stiff upper bound and Reuss soft lower bound is estimated (Smith et al., 2003). This average is called the Hill average and is an estimation of the elastic moduli for more complex cases; it is defined as:

$$M_{Hill} = \left[\frac{M_{Voigt} + M_{Reuss}}{2} \right]. \tag{3.11}$$

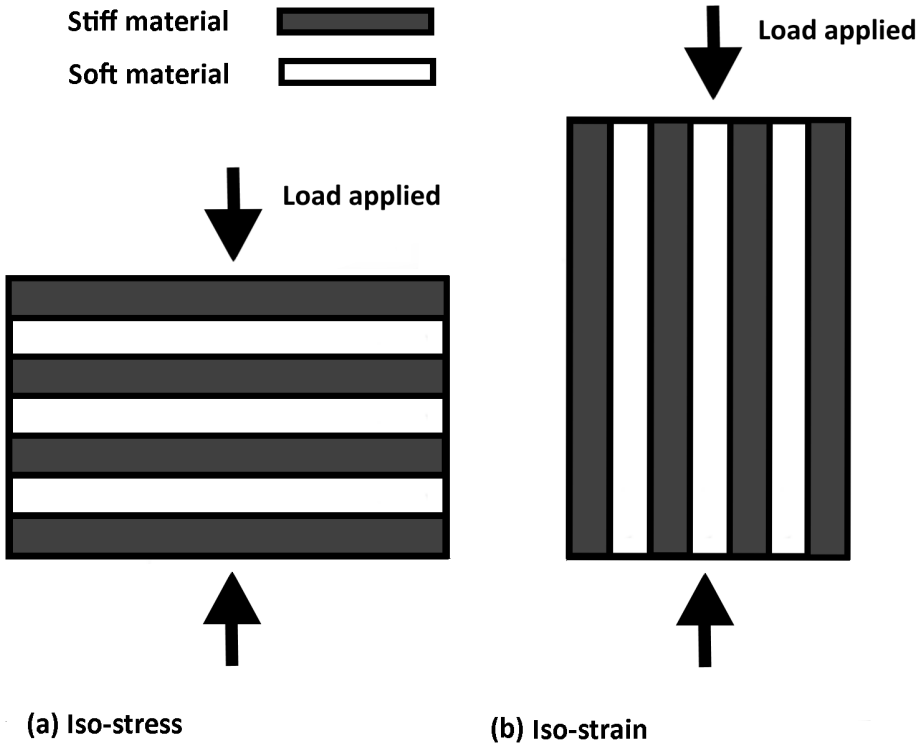

Figure 3.4-2: *(a) Horizontal layering of stiff and soft materials cause an iso-stress case (Reuss model). (b) Vertical layering cause an iso-strain case (Voigt). Inspired by Gelius and Johansen (2012).*

3.5 Rock physics models

A porous rock consists of various constituents with different physical properties (Gelius and Johansen, 2012). These constituents will therefore give different elastic responses due to an applied stress loading (Gelius and Johansen, 2012). By using theoretical models, effective elastic properties may be obtained from the effective physical properties of a porous rock. These models are called rock physics models and consider physical properties such as bulk and shear modulus, density, porosity, pore shape and fluid saturation. The bulk, shear and density of each mineral, the fractions of the different minerals and how these are mixed, must be considered when performing a rock physics modelling. These considerations also applies for the different fluids occupying the pore space in the model.

There exist many different types of rock physics models, each having benefits and

limitations (Avseth et al., 2010). Therefore, it is essential to choose the most appropriate model for a specific case, which then will give the best representative effective elastic properties of a reservoir. This is also important in terms of obtaining the most realistic seismic when performing a seismic forward modelling.

As mentioned earlier, pore shape plays a significant role in carbonate rock physics. Sayers (2008) elaborates that this applies for saturated carbonate rocks, while mineral composition is the dominant factor controlling elastic properties for dry rocks. The connectivity between the pores (especially flat compliant pores) will also influence the elastic properties of a rock due to pore fluid flow (Agersborg et al., 2008). A general principle is that the elastic properties, and therefore the seismic velocity of a rock, decrease with increasing porosity.

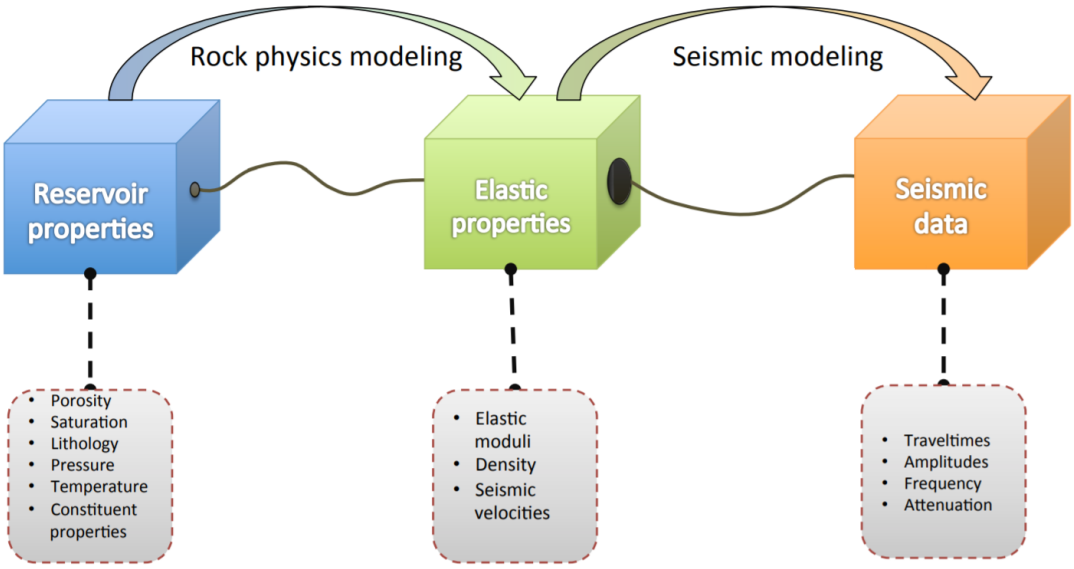

Figure 3.5-1: *The various parameter domains connected by rock physics modelling and seismic forward modelling. Adapted from Bredesen (2012).*

The Gassmann model for fluid substitution

The Gassmann-model is commonly used to calculate the effect of fluid substitution on seismic properties for a porous rock (Gelius and Johansen, 2012; Wang, 2001). The Gassmann equation calculates the elastic moduli for a porous rock using the frame properties, where the effective bulk modulus of a saturated rock, K_{sat} is given

by (Gassmann, 1951; Smith et al., 2003; Wang, 2001):

$$K_{sat} = K_{dry} + \frac{\left(1 - \frac{K_{dry}}{K_{matrix}}\right)^2}{\frac{\phi}{K_{fluid}} + \frac{1-\phi}{K_{matrix}} - \frac{K_{dry}}{K_{matrix}^2}}, \tag{3.12}$$

where K_{dry}, K_{matrix} and K_{fluid} are the effective bulk moduli of the dry rock, the matrix and the fluid respectively, whereas ϕ describes the porosity of the rock. Equation 3.12 can also be rearranged and used to calculate the effective bulk moduli of the dry rock:

$$K_{dry} = \frac{K_{sat}\left(\frac{\phi K_{matrix}}{K_{fluid}} + 1 - \phi\right) - K_{matrix}}{\frac{\phi K_{matrix}}{K_{fluid}} + \frac{K_{sat}}{K_{matrix}} - 1 - \phi}. \tag{3.13}$$

Since the shear modulus of a rock is not affected by fluid saturation, the effective shear moduli of the saturated and dry rock, are the same (Wang, 2001):

$$\mu_{sat} = \mu_{dry}, \tag{3.14}$$

where μ_{sat} is the effective shear modulus of a saturated rock, while μ_{dry} represents the effective shear modulus of a dry rock. If there are more than one fluid occupying the pore space, the effective bulk modulus representing the fluid content, K_{fluid}, is given by Wood's equation for N different fluids (Gelius and Johansen, 2012):

$$\frac{1}{K_{fluid}} = \sum_{i=1}^{N} \frac{S_i}{K_i}, \tag{3.15}$$

where S_i and K_i represent the saturation and bulk modulus respectively, for each constituent i. The effective shear modulus of a fluid equals zero. The last parameter needed to be able to calculate the seismic velocities of a saturated rock, is the density. The density of a saturated rock, ρ_{sat}, is defined by the simple equation (Wang, 2001):

$$\rho_{sat} = \rho_{dry} + \phi\rho_{fluid}, \tag{3.16}$$

where ρ_{dry} and ρ_{fluid} represent the dry rock density and fluid density respectively. Since $\rho_{dry} = (1 - \phi)\rho_{matrix}$, equation 3.16 may also be expressed as:

$$\rho_{sat} = (1 - \phi)\rho_{matrix} + \phi\rho_{fluid}, \tag{3.17}$$

where ρ_{matrix} represents the density of the matrix. By using the parameters calculated above, P-wave and S-wave velocities can be calculated for the saturated rock using equation 3.1 and 3.2 shown in section 3.2.

Gassmann assumptions

The Gassmann-model is based on a set of assumptions, which are (Adam et al., 2006; Chopra and Castagna, 2014):

1. The rock is homogeneous and isotropic.
2. The pore fluid is homogeneous.
3. The system is closed, which means that there is no fluid flow in or out of the system.
4. All pores, within the system, are connected and fully saturated, and the fluid can move freely.
5. There is no interaction between the solid rock and the pore fluid.
6. Enough time for the pore pressure to equilibrate throughout the interconnected pore space when the medium is being deformed.

Gassmann in carbonates

Due to the complex pore system of carbonate rocks, many authors question the validity of Gassmann fluid substitution for carbonate rocks, while others believe that experimental procedures must be carefully adapted to heterogeneities of carbonate rocks for the Gassmann theory to be applicable (Rasolofosaon et al., 2008; Xu and Payne, 2009).

The Gassmann assumptions do not account for or approve of many of the inherent factors of carbonates such as difference in pore shape, heterogeneities, and also the potential chemical reaction between the carbonate mineralogical constituents and the pore fluid, which is an essential consideration due to the soluble nature of carbonate rocks (Vanorio et al., 2008).

Since the seismic properties of carbonate rocks depend on the different pore shapes, they are an important consideration. Unconnected pores and cavities of different sizes are common in carbonate rocks, especially in karstified formations, and do not satisfy the Gassmann assumptions. These pores may cause higher seismic velocities contra if the pores were connected (Agersborg et al., 2008).

Further the Gassmann theory assumes that the shear modulus of a saturated rock equals the shear modulus of a dry rock. This assumption seems to be inaccurate for carbonates according to studies which report shear strengthening or weakening due to pore fluid interaction with the rock matrix (Adam et al., 2006; Agersborg et al., 2008).

Differential effective medium (DEM)

Since the Gassmann model does not take pore geometry into account, it could be more suitable to use an inclusion based model which considers a rock volume to contain pores as inclusions. The inclusions are uniformly distributed and randomly oriented, where each inclusion represents a pore in the rock (Gelius and Johansen, 2012). The inclusion based model considers each pore to be a scatterer of seismic wave energy (Gelius and Johansen, 2012). The scattered waves occur due to differences in strain between the inclusion and the surrounding material.

Differential effective medium (DEM) is an example of a such scattering-model. DEM is based on gradually implementing pore geometries of different sizes and shapes into a rock volume. After implementing the first set of pores, it uses Kuster-Toksöz model to calculate the effective elastic properties of the rock volume. Next step is to implement a second set of pores to the rock volume, which already includes the first set of pores. Again, the effective elastic properties are calculated for the rock volume with the new set of pores. This procedure continues until the desired porosity is achieved (Gelius and Johansen, 2012). The effective bulk and shear moduli for a rock volume where the inclusions contain fluids, the DEM-modelling are calculated by a set of differential equations (Berryman, 1992; Mavko et al., 2009):

$$(1-\phi)\frac{d}{d\phi}[K_{DEM}(\phi)] = (K_{fluid} - K_{DEM}(\phi))P^*, \tag{3.18}$$

$$(1-\phi)\frac{d}{d\phi}[\mu_{DEM}(\phi)] = -\mu_{DEM}(\phi)Q^*, \tag{3.19}$$

where ϕ represents the porosity, K_{DEM} and μ_{DEM} represent the effective bulk and shear moduli at a given porosity, respectively, K_{fluid} is the bulk modulus of the fluid, and P^* and Q^* represent components that take the geometrical factors of the inclusions into account (Mavko et al., 2009).

DEM-modelling takes pore geometry into account by adding inclusions with different aspect ratio. The aspect ratio, which is the ratio between the minor and major axis of an ellipsoid, decides if the inclusion is a spherical or flat ellipsoid (Gelius and Johansen, 2012). A high aspect ratio gives a spherical pore, while a low aspect

ratio gives a flat disc-like pore. All the different inclusions with various aspect ratios within the material are defined as the aspect ratio concentration (Gelius and Johansen, 2012).

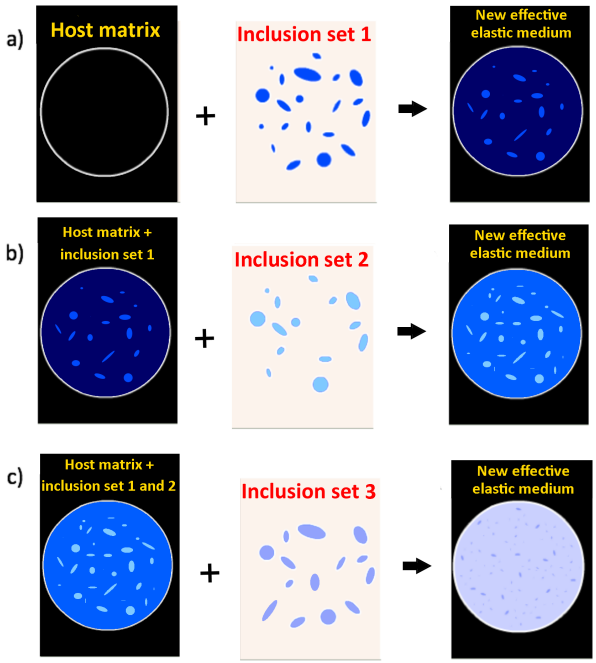

Figure 3.5-2: *The schematics of the Differential effective medium (DEM) theory, where (a) shows the first step of adding inclusions to the host matrix before calculating the effective elastic properties of the new matrix volume, including the initial host matrix and the newly added inclusions. (b) and (c) show further steps of the modelling method until the desired porosity is achieved. This figure shows three steps of the modelling method, though it could be a lot more depending on the amount of porosity requested. Modified from Gelius and Johansen (2012).*

An important consideration in rock physics modelling, is the pore-to-pore interaction in terms of the scattering interference between inclusion and the local fluid flow between pores. By using higher order scattering terms, the earlier embedded pores influence the later embedded pores (Gelius and Johansen, 2012). The DEM-modelling accounts for the local fluid flow by implementing larger and larger pore volumes for each stage (Gelius and Johansen, 2012).

The DEM-method is asymmetric meaning it considers a volume of solid matrix to be a solid until there is a 100% porosity, which means the volume only contains fluids (Mavko et al., 2009). This means the solid is connected until 100 percent porosity. This does not realistic for reservoir rocks. A way of dealing with this problem, is to introduce a critical porosity, ϕ_c, which is much lower than 100%. The critical

porosity then replaces the end member which is pure fluid, to be more applicable for reservoir rock scenarios (Mavko et al., 2009).

Contact cement theory (CCT)

Cementation of grains may occur before or after deposition and will influence the elastic properties of the rock. The cement may occur either inside pores as pore-filling material or as a part of the matrix, where cement occurs at contacts (Gelius and Johansen, 2012). The contact cement theory (CCT) is a method developed to take the cement into consideration by computing the affect of the elastic properties of the cement, its volume fraction and the critical porosity, and what influence these factors have on the effective elastic moduli of the total cemented granular volume (Gelius and Johansen, 2012).

Cementation between contacts cause a small porosity-decrease, while the stiffness of the granular composite will be subjected to a huge increase (Dvorkin and Nur, 1996). Even very small amounts of cement will significantly increase the elastic properties of the composite. This explains why sometimes high-porosity rocks may have a much higher seismic velocity than expected (Dvorkin and Nur, 1996).

Hashin-Shtrikman bounds

To be able to compute the effective elastic moduli of a material containing a solid matrix and pores, it is important to know the volume fractions, the elastic moduli and geometric details of the different phases and how they relate to each other (Mavko et al., 2009). If only the volume fractions and the elastic moduli of each constituents are known, an estimation of the value between an upper and a lower bound are the best way of computing the effective elastic moduli of the total medium (figure 3.5-3). The exact value can be acquired by including the geometrical details of the pores.

The upper and lower bounds for the range of possible solutions of the effective elastic moduli are decided by the stiffness of the pores, where stiff pores give a higher value while soft pores give a lower value. The stiffness is usually decided by the shape of the pores (Mavko et al., 2009). The narrowest possible range of solutions, where the geometrical details remain unknown, is called the Hashin-Shtrikman bounds. The Hashin-Shtrikman bounds depend on an isotropic linear elastic composite, and for two constituents the bounds are defined as (Mavko et al., 2009):

$$K^{HS\pm} = K_1 + \frac{f_2}{(K_2 - K_1)^{-1} + f_1(K_1 + \frac{4}{3}\mu_1)^{-1}}, \tag{3.20}$$

$$\mu^{HS\pm} = \mu_1 + \frac{f_2}{(\mu_2 - \mu_1)^{-1} + \frac{2f_1(K_1+2\mu_1)}{[5\mu_1(K_1+\frac{4}{3}\mu_1)]}}, \tag{3.21}$$

where K_1 and K_2 for the bulk moduli of different phases, μ_1 and μ_2 are the shear moduli of different phases, and f_1 and f_2 are the volume fractions of different phases. When the stiffest material is termed 1, the expression provides the upper bound, while it provides the lower bound when the softest material is termed 1 (Mavko et al., 2009). The equations assume that when the bulk modulus of a constituent is the largest, the shear modulus is also the largest for the same constituent (Mavko et al., 2009).

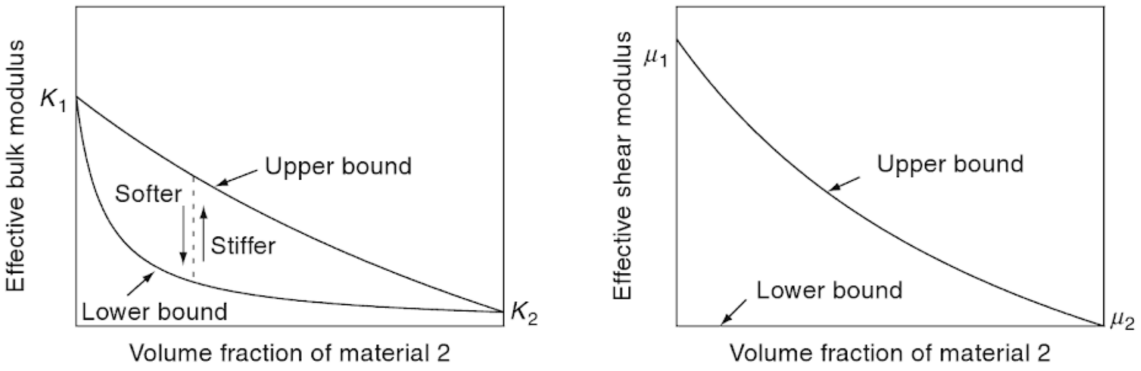

Figure 3.5-3: *A diagram illustrating the upper and lower bounds of the elastic bulk (left) and shear (right) moduli (Mavko et al., 2009).*

The Kite-model

Avseth et al. (2014) present a hybrid rock physics model which takes depositional and burial history into consideration. The model is called the Kite-model and consists of three main steps describing the elastic properties for different amount of porosity present in the material. For a low-porosity case, the inclusion-based DEM-model is used to account for different pore geometries. For a high-porosity case (larger than 20%), the CCT-model is preferred. To calculate the elastic properties between these two end-members, the Kite-model uses Hashin-Shtrikman upper bound (HSUB). The basic concept of this model is illustrated in figure 3.5-4.

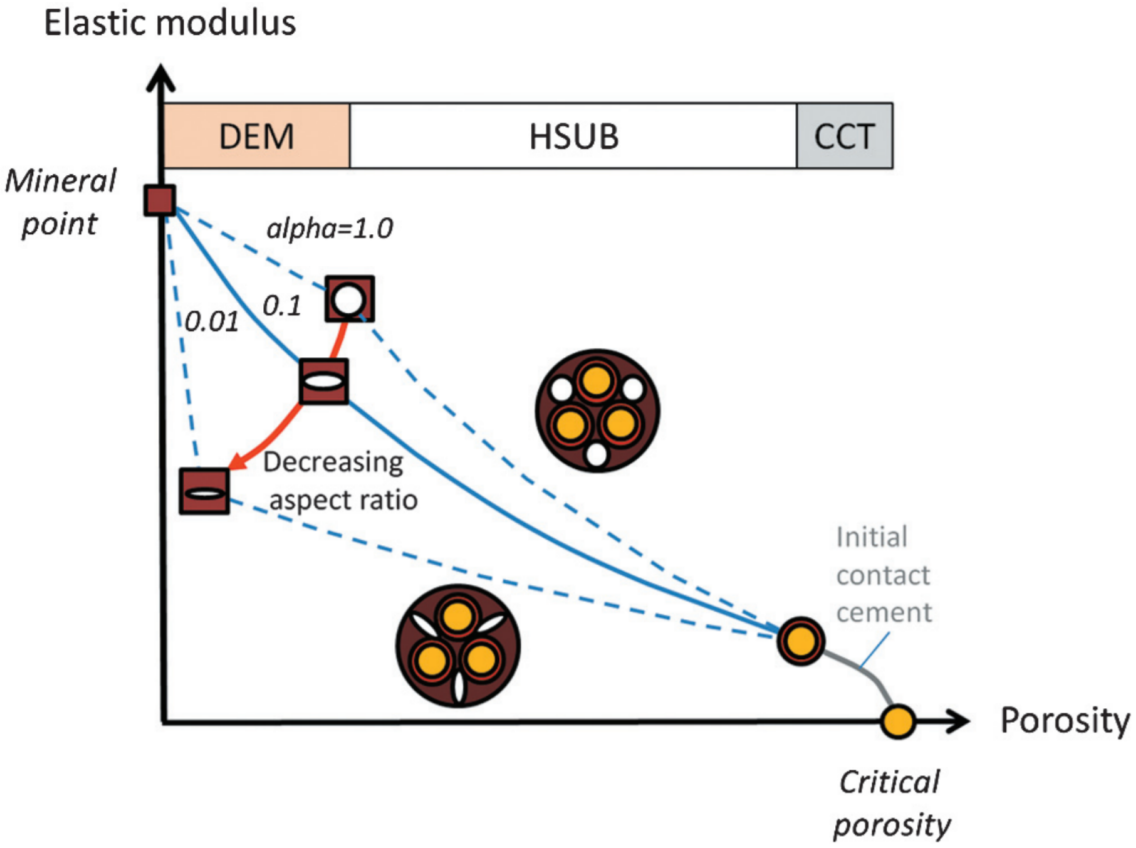

Figure 3.5-4: *Schematics illustrating the Kite-model, where a combination of differential effective medium-theory (DEM), contact cement theory (CCT) and Hashin Shtrikman upper bound (HSUB) are used to calculate the elastic properties of different amount of porosity (Avseth et al., 2014).*

The pore geometry is an important consideration especially for low-porosity cases, and that is why an inclusion based model such as DEM is chosen for the low-porosity part. From figure 3.5-4 it is possible to see how large effect the pore geometry has on

the elastic properties. Where the porosity is very low and most of the inclusion may be isolated, the DEM could be used to estimate the pore fluid effects. Otherwise for low-porosity but connected pores, the dry rock properties are calculated by DEM, and used as input for the Gassmann model (Avseth et al., 2014). Also, for higher porosity cases, the Kite-model uses Gassmann-model to study the pore fluid effects.

The cement contact theory (CCT), used to calculate the elastic properties in the high-porosity zone, is described as (Avseth et al., 2014):

$$K_{CCT} = \frac{n[1 - \phi_{CCT}/(1 - S_C)]}{6} M_C S_n, \tag{3.22}$$

$$\mu_{CCT} = \frac{1}{5} K_{CCT} + \frac{3n[1 - \phi_{CCT}/(1 - S_C)]}{20} \mu_C S_\tau, \tag{3.23}$$

where n is the coordination number, which is the number of contact points per grain, M_C and μ_C are the P-wave bulk and shear modulus of the cement, respectively, S_C is the fraction of the cemented porosity of the unconsolidated medium, and S_n and S_τ are normal and shear stiffness at the grain contacts, describing the relation between the grains and the cement (Avseth et al., 2014). In the equation, ϕ_{CCT} describes the porosity value at the maximum porosity point (Avseth et al., 2014). The shear modulus calculated by the CCT is usually to high due to slip and/or torsion, and therefore a shear relaxation factor, between zero and one, is multiplied to the shear stiffness (Avseth et al., 2014).

The HSUB is used to calculate the elastic properties between properties calculated by the DEM- and the CCT-modelling methods. The stiff components represent the cement properties in this case, and that is why the upper bound of the Hashin-Shtrikman equation is used (Eq. 3.20 and 3.21).

The Kite-model presents a modelling method that account for complex geology and the effects of different elements such as porosity, pore aspect ratio of a low-porosity case, cement between grains in a high-porosity case, and saturation. This approach may be useful for estimating elastic properties in carbonate reservoirs (Avseth et al., 2014).

Limitations of rock physics models

The rock physics models are based on assumptions and therefore have significant limitations (Wang, 1997). The more advanced and complicated models that tries to explain the rocks more accurately, are usually too difficult to understand and too complicated to use (Wang, 1997). Therefore, the models often use simplifications to

be applicable and easily understood, but simplifications cause inaccurate assumptions, which is important to have in mind. The main object with the rock physics modelling are to make an adequate model that describe the rock conditions as good as possible. It is useful to know the range of applicability for the different models, and therefore not expand beyond these theoretical boundaries, due to the possibility of generating erroneous results (Wang, 2001).

Chapter 4

Seismic Modelling

Seismic modelling is a tool to get a better understanding of the elastic wave propagation in the subsurface (Lecomte et al., 2016). Modelling may help interpreters to validate complex geological structures by comparing the seismic obtained from geological models, with real seismic data. To get the ideal simulation of seismic data concerning a specific geological feature, seismograms based on a conceptual representation of a survey should be generated, where a full-wavefield modelling approach, such as the finite-difference method, should be considered (Lecomte et al., 2015). Using a full-wavefield approach is important when considering a comprehensive complex structure and when the study demands an accurate result. For such studies, the available computer power must be adequately large.

Where more efficient methods are required, ray-based approaches are more suitable. There exit several alternatives of ray based modelling methods, but in this study a modelling approach based on convolution theory, will by considered. 1D convolution is a popular and efficient modelling method due to its simplicity (Lecomte et al., 2015). When the geology is more complex than horizontally flat layers and lateral variations are expected, in terms of structures and velocity, the validity of the 1D convolution method is however restricted and does not represent realistic seismic (Lecomte et al., 2015, 2016).

A way of keeping the efficiency that comes with a ray-based approach and still be able to take more complex geological structures with lateral variations into account, is to use a 2(3)D convolution approach, which simulates prestack depth migrated (PSDM)-images (Lecomte, 2008; Lecomte et al., 2016). Since the modelling in this thesis includes complex geological structures, and since the work consists of varying petrophysical parameters to look at different seismic responses, the modelling method requires efficiency with sufficient results. That is why the 2(3)D convolution approach will be suitable for this task. Further explanation about the 2(3)D

convolution method and methods used for similar tasks will be presented in a later section of this chapter, but first there will be a review of some of the theory behind the selected seismic modelling method.

4.1 Seismic rays and raypath

Seismic rays represent the direction of a propagating seismic wave. Rays are perpendicular to the wavefront of the seismic wave in a isotropic homogeneous medium (Kearey et al., 2013). A ray-based modelling method considers the ray path of the travelling wave instead of the whole wavefield. As rays are travelling through a layered medium, the direction and energy of these rays may change due to different physical properties of the layers.

Snell's law is used to describe the change of direction of the reflected and refracted seismic wave when dealing with a non-zero incident angle (θ_i) (figure 4.1-1). A refracted wave is a transmitted wave that has changed direction and strength due to a different physical environment. When considering non-zero incident angles, the waves may also be converted at the interface (P-wave converted to S-wave for instance). The complex Zoeppritz's equations describe how the seismic energy is distributed based on the incident angle (Kearey et al., 2013).

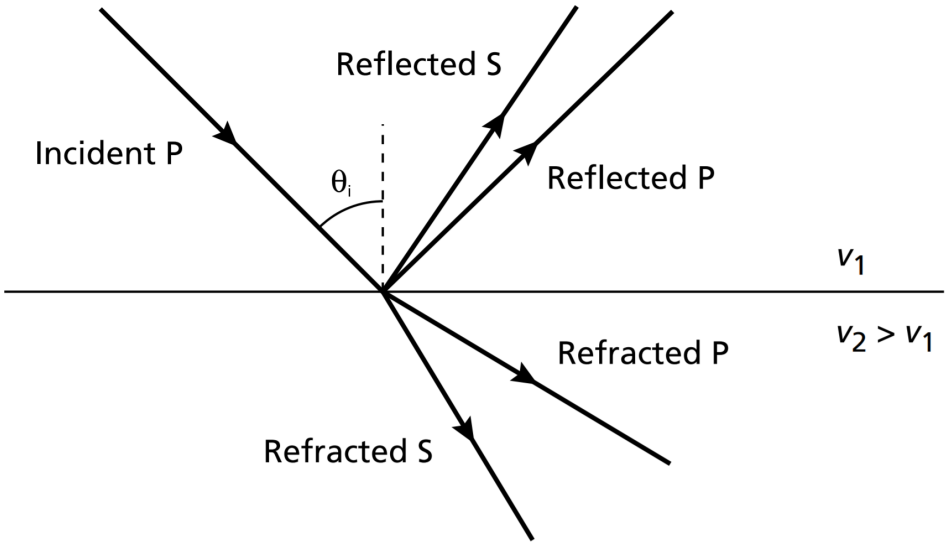

Figure 4.1-1: *An incident P-wave with a non-zero angle will be partitioned into a reflected P- and S-wave, and into a refracted P- and S-wave, at an interface where there exists a contrast in elastic properties (Kearey et al., 2013).*

The slowness vector is perpendicular to the wavefront, and in an isotropic case the ray path will be parallel to the slowness vector (Claerbout, 1985; Lecomte, 2008). The slowness vector has a magnitude inverse to the velocity, and is defined as the first spatial derivatives (dx, dz) of the traveltime, t (Claerbout, 1985):

$$slowness\ vector = \Big(\frac{dt}{dx}, \frac{dt}{dz}\Big). \tag{4.1}$$

The slowness vectors can be used to describe the illumination vector at a given point in the subsurface (Lecomte, 2008). The illumination vector may help describe which features that will be illuminated (visible) in synthetic seismic and which will be invisible. The illumination vector will be further described in a later section where a description of the modelling method will be given.

The lack of illumination is an important consideration for seismic modelling methods. By considering this, one can better plan a seismic survey for a complex target. Another important consideration is how much details are possible to determine with seismic acquisition and imaging. The geology represents a perfect resolution, but by imaging the geology with seismic, this perfect resolution will be distorted.

4.2 Seismic resolution

Seismic resolution decides the degree of details that will be included in a seismic image of the subsurface. Interpreters would want as high resolution as possible to be able to distinguish between finer geological details in the seismic data (Herron, 2011).

The seismic resolution is determined by the dominant wavelength of a seismic reflection, which is given by the seismic velocity of the sedimentary strata and the dominant frequency of the seismic signal. Since the seismic velocity usually increases with depth and because higher frequencies get attenuated with large depths, both the vertical and the lateral resolution get poorer with increasing depths (Kearey et al., 2013).

Lateral resolution is defined by the Fresnel zone (figure 4.2-1). For a ray with infinite frequencies, the reflected energy will originate from one point at the reflector. This is not realistic for seismic signals, which have band-limited frequency content. Considering frequencies with a band limit, the energy from a wavefront will not be reflected as one point, but as a zone around the point. This zone is called the Fresnel zone and determines the lateral seismic resolution (Gelius and Johansen, 2012). For a plane reflector and zero-offset case, the radius of the Fresnel zone, R_f, is given by (Gelius and Johansen, 2012):

$$R_f = \sqrt{\frac{z\lambda}{2}}, \tag{4.2}$$

where λ is the wavelength and z is the depth. This equation can also be represented by using the velocity (v) and the dominant frequency (f_{dom}) since $\lambda = \frac{v}{f}$:

$$R_f = \sqrt{\frac{zv}{2f_{dom}}}. \tag{4.3}$$

The Fresnel zone describes the lateral resolution of un-migrated seismic data (Herron, 2011). Migration collapses this Fresnel zone which leads to an improved lateral resolution (Simm and Bacon, 2014). The seismic modelling approach in this thesis, simulates the results of a PSDM (migrated seismic), which means that the lateral resolution mentioned later on, is referred to the collapsed Fresnel zone illustrated in figure 4.2-2.

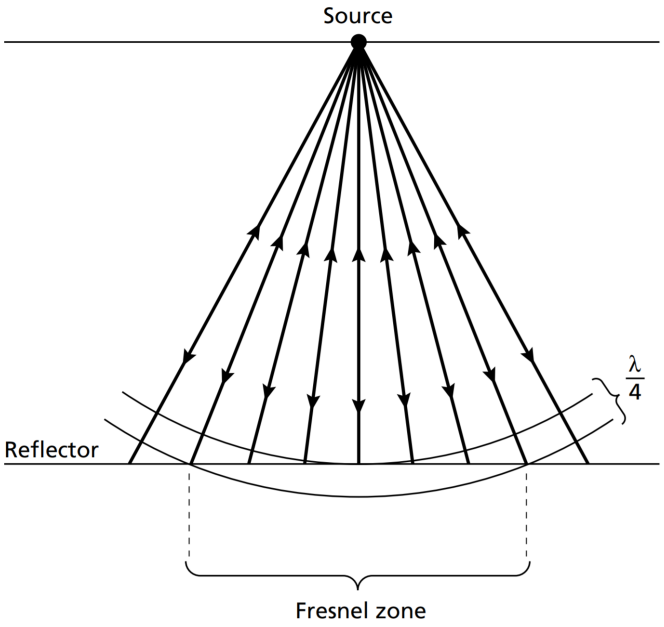

Figure 4.2-1: *Energy within the Fresnel zone is reflected back to the surface, representing the target reflector right beneath the source. Features smaller than this zone will not be detected in the seismic data (Kearey et al., 2013).*

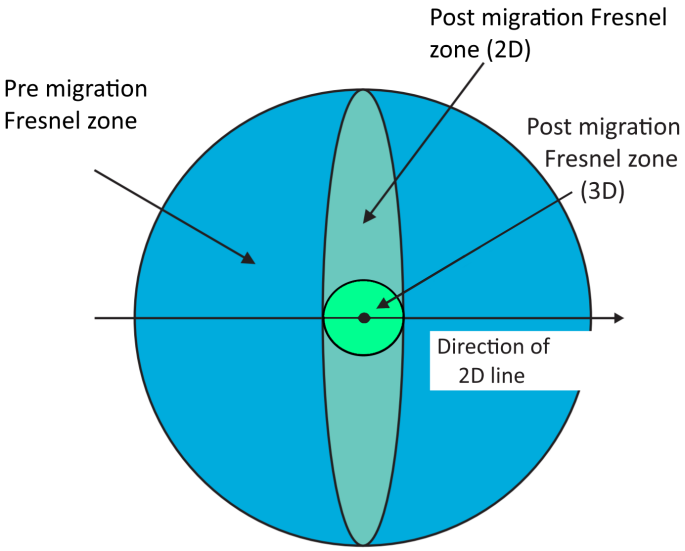

Figure 4.2-2: *The figure describes the lateral resolution in terms of a Fresnel zone before and after migration. Migration collapses the Fresnel zone to a circle (ideally) with radius $\frac{\lambda}{4}$ (for 3D migration, see green circle). This enhancement of lateral resolution will only occur in the direction of the 2D line, when a 2D migration case is considered. Modified from Simm and Bacon (2014).*

Vertical resolution decides if closely spaced reflectors will be detected in the seismic data (Kearey et al., 2013). The maximum resolution or the minimum thickness (tuning thickness) that may be detected is determined by the wavelength of the pulse, and is given as a rule of thumb as a quarter of a wavelength, $\frac{\lambda}{4}$ (Herron, 2011). This is not fixed, which means that the resolution may be smaller or larger than $\frac{\lambda}{4}$.

The essence of seismic modelling, is to reproduce the imaging effects that come with seismic. The seismic modelling method used in this thesis, is a 3D convolution approach where a point-spread function (PSF) is convolved with an input reflectivity model, which will result in a "blurred" representation of this input model (Lecomte et al., 2015). The PSF may be seen as a 2(3)D representation of a wavelet.

4.3 Convolution theory

Convolution describes an alteration of the shape of an input signal due to an applied filter. In seismic modelling, the convolution is between an input source wavelet and a reflection coefficient series (Kearey et al., 2013; Simm and Bacon, 2014). The reflection coefficients are determined by contrasts in elastic properties at boundaries in a geological section (section 3.3). The mathematical operation describing convolution is given by:

$$y(t) = g(t) \star f(t), \tag{4.4}$$

where $y(t)$ is the filtered output, $g(t)$ is input signal and $f(t)$ describes the filter. Figure 4.3-1 illustrates a simple convolution based on Eq.4.4, while figure 4.3-2 illustrates a 1D convolution between a reflectivity series and corresponding wavelets describing the different reflection coefficients.

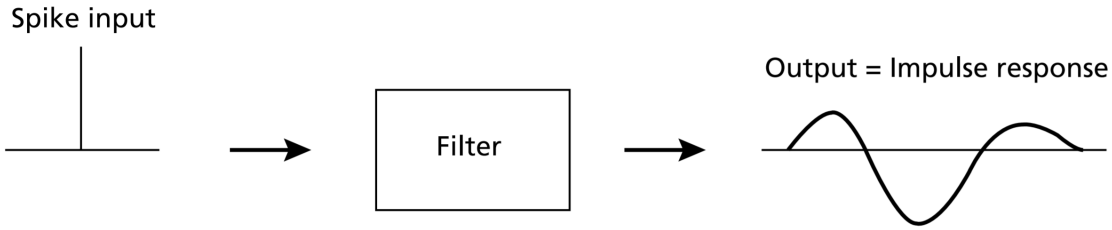

Figure 4.3-1: *Simple illustration of an input signal convolved with a filter which results in an output signal (Kearey et al., 2013).*

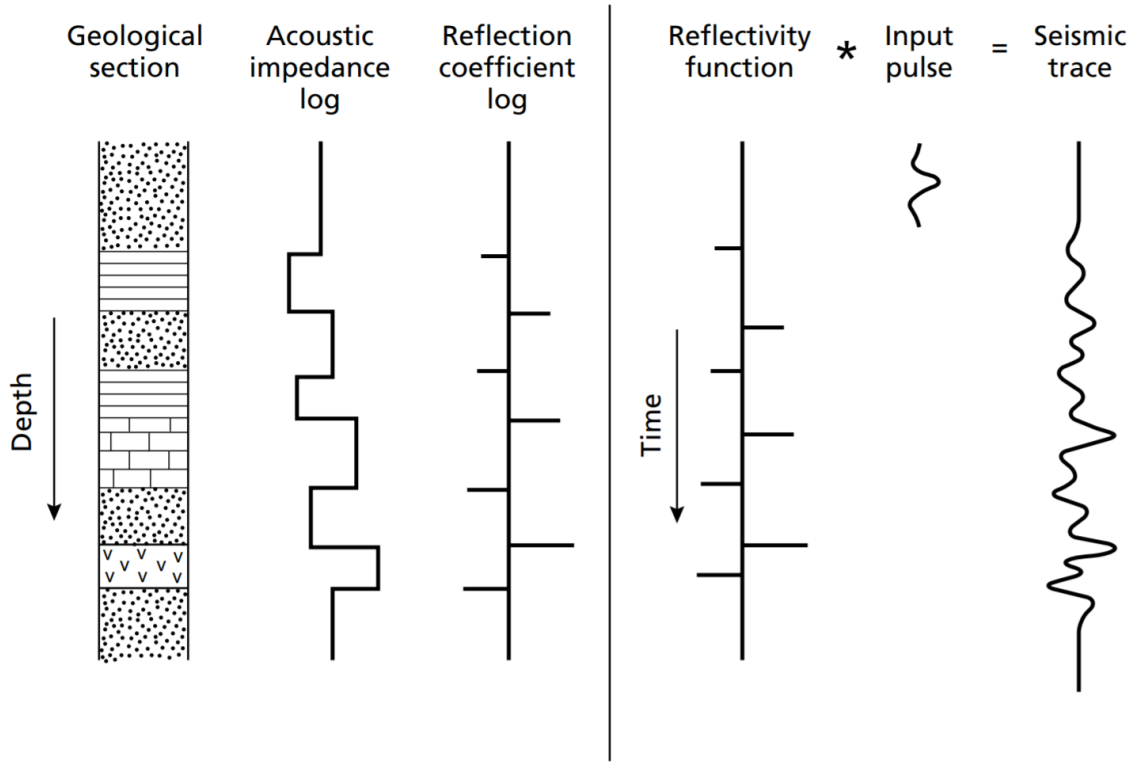

Figure 4.3-2: *The illustration describes a 1D convolution modelling. The reflection coefficients are retrieved from an acoustic impedance log representing geological boundaries, and by convolving an input pulse with a reflectivity function, a seismic trace is obtained (Kearey et al., 2013).*

The 1D convolution approach is also applied to more advanced reflectivity models with lateral variations, instead of just a vertical reflectivity series, though this would result in an unrealistic synthetic seismic, where the lateral resolution effects will not be accounted for.

4.4 The Fourier transform (FT)

The Fourier transform (FT) takes a signal defined in the time domain, and transforms it to the frequency domain. Convolution in the time domain is equivalent with multiplication in the frequency domain, which is an advantage considering that multiplication is a much simpler calculation.

A signal in the time domain represented as the sum of sine or cosine waves with various amplitudes, is decomposed into the frequency domain and represented as amplitude and phase spectra describing the signal (Kearey et al., 2013). The Fourier transform is described by:

$$g(t) = FT(G(f)), \tag{4.5}$$

where $g(t)$ represents the signal in time domain and $G(f)$ in frequency domain, making $g(t)$ and $G(f)$ a Fourier pair (Kearey et al., 2013). Example of such Fourier pairs are displayed in figure 4.4-1. The $G(f)$ is a complex function including the amplitude (A) and phase (ϕ) spectra:

$$G(f) = A(f)e^{i\phi(f)}. \tag{4.6}$$

For digitized signals, a Fourier transform may be conducted using an algorithm called a Fast Fourier transform (FFT) which is implemented into different computer programs (Kearey et al., 2013). This makes the Fourier transform fairly simple to use.

A signal in the time domain may be described by a time period, the time it takes the signal to reach its starting position again, while a signal in the space domain may be described by the wavelength, the distance of which the signal travels over over a given time period (figure 4.4-2) (Gelius and Johansen, 2012). The link between these domains, is the velocity. FT may be performed in both time and space domain. The FT of a time signal will give the amplitudes and phases plotted with different frequencies, while the FT of a signal in the space domain will give amplitudes and phases plotted with different wavenumbers, k, also called spatial frequencies (Kearey et al., 2013).

The wavenumber of an image point, scattering wavenumber, describes the illumination and the resolution of the image point (Gjøystdal et al., 2002; Lecomte, 2008). By performing an inverse FT back to the space domain, will give a representation of a plane wavefront perpendicular to the scattering wavenumber vector (Lecomte, 2008). A good coverage in the wavenumber domain, described by a long illumination vector and a long frequency band, will result in a sharp representation of the plane

wavefront in the space domain, which describes a good resolution. When several scattering wavenumbers for a set of source-receiver pairs (k_{SR}) in the wavenumber domain are included, and performing an inverse FT back to space domain, the PSF representation of the image point is obtained (Lecomte, 2008).

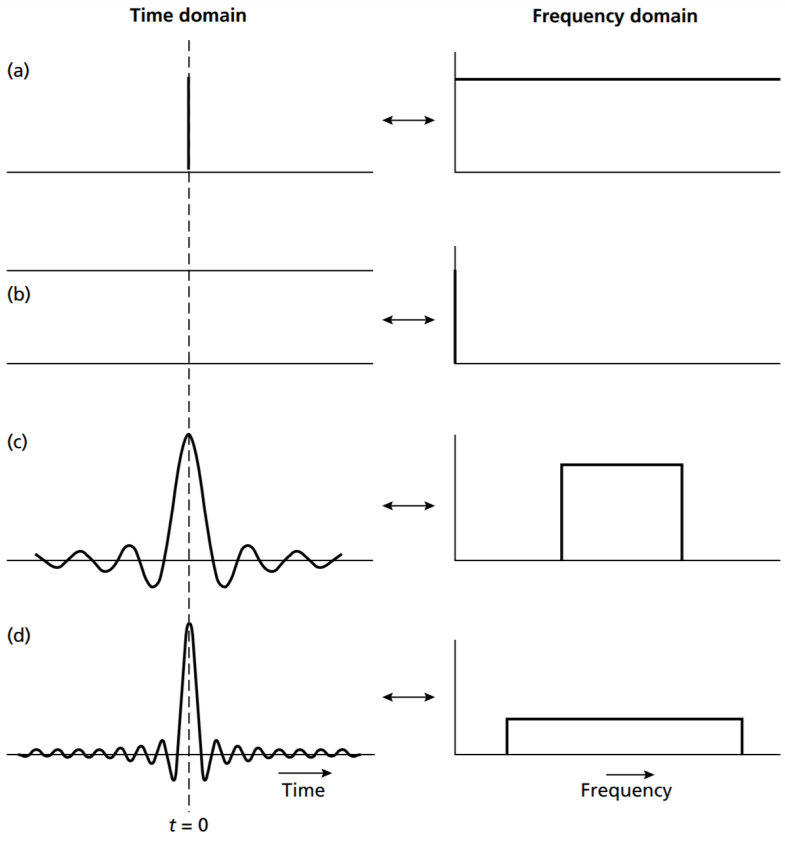

Figure 4.4-1: *Considering zero-phased waveforms, (a)-(d) illustrate the Fourier pair of various waveforms (Kearey et al., 2013).*

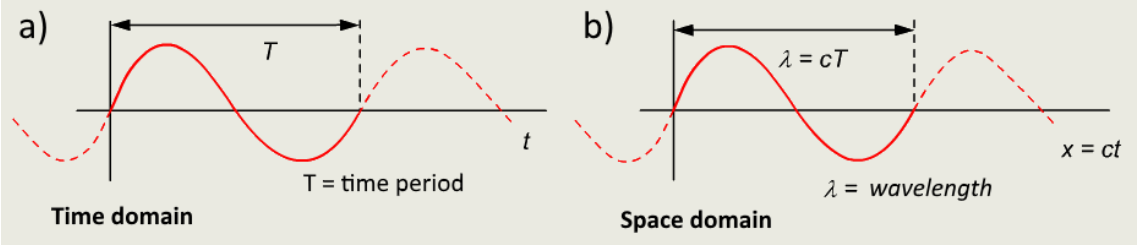

Figure 4.4-2: *A signal displayed in (a) the time domain, and (b) the space domain. The component linking the two domains, is the velocity (in this figure represented by c) (Gelius and Johansen, 2012).*

4.5 Prestack Depth Migration (PSDM)

What migration does is to move a seismic reflected event from a recorded point in the subsurface between a source and receiver (or right beneath for zero-offset cases), and move the reflection point to its true location in the subsurface (Herron, 2011). This process is illustrated by a simple example in figure 4.5-1, where a migration is performed for a dipping layer.

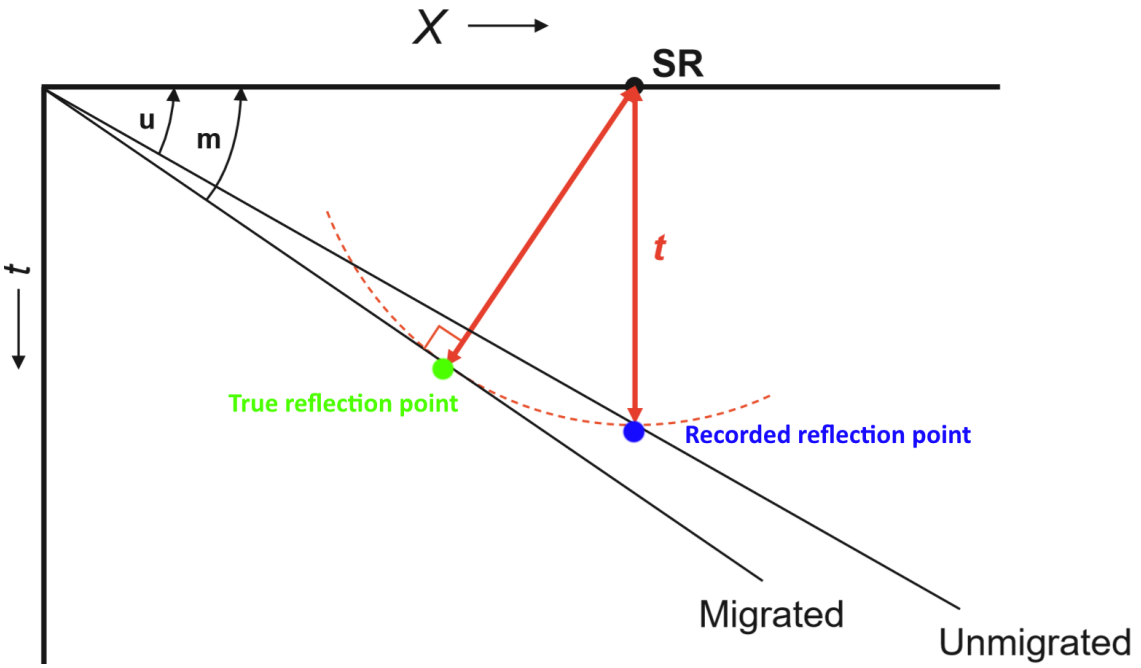

Figure 4.5-1: *Seismic reflection of a dipping layer for a zero-offset case, where the reflection is recorded in time (t) to and positioned beneath the source and receiver (SR). The reflection is then moved to the true position in the subsurface due to a migration process. u and m represent the angles of the dipping layer for an unmigrated case and a migrated case, respectively. Modified from Herron (2011).*

PSDM is migration performed before stacking the traces representing one reflection point, and it is performed directly in the depth domain. PSDM is usually necessary for areas with significant lateral variations in terms of velocity, because giving a more accurate description of geological structures (Herron, 2011).

PSDM representations of seismic images are obtained by using scattering isochrones, which are elliptical (or circular) representations of the wavefronts from a specific source-receiver pair in a homogeneous medium (figure 4.5-2). The isochrones will cross each other at the location of the image point (Lecomte, 2008). By considering the isochrones of several traces representing the same subsurface point, there will

occur a superposition by constructive interference at the location of the actual point, and destructive interference everywhere else (Lecomte, 2008). This is a PSDM representation of a point scatter (PSF), which is further used in a convolution process to generate synthetic PSDM images.

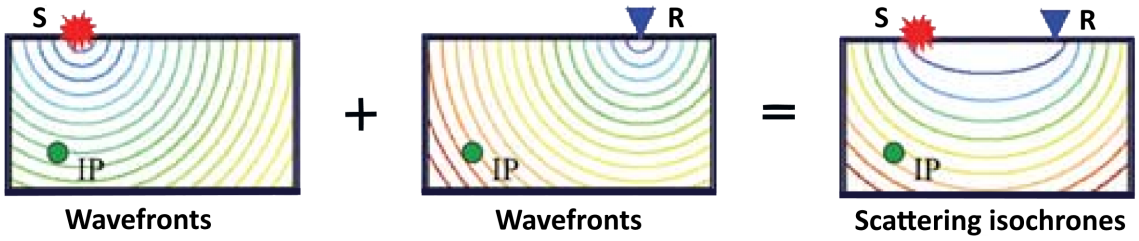

Figure 4.5-2: *Scattering isochrones for an isotropic case, where the scattering isochrones are combined by the wavefronts from source to the image point (IP), with the wavefronts from receiver to the image point, resulting in elliptical isochrones (Lecomte, 2008).*

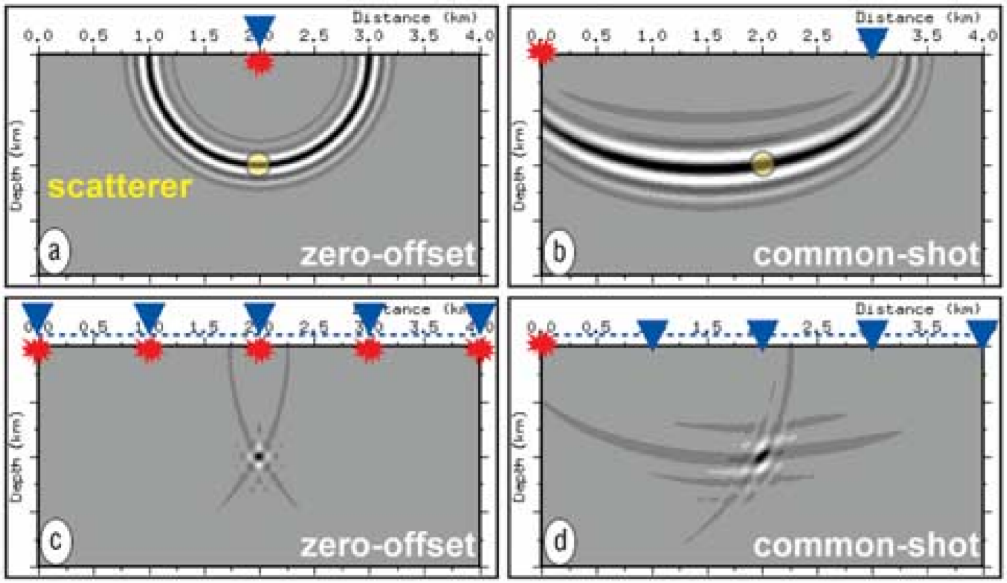

Figure 4.5-3: *For an isotropic homogeneous background velocity case, (a) illustrates a zero-offset case of a PSDM representation of a point scatterer (yellow) for one single source-receiver (red/blue) pair. (b) Presents the same case as (a) but includes an offset of 3 km. (c) And (d) represents a superposition of all the PSDM representations for several source-receiver pair for the same point scatterer, for a zero-offset case and one including offset, respectively. The zero-offset case leads to a better resolution of the point scatterer (Lecomte, 2008).*

4.6 2(3)D Convolution method

The following description of the 2(3) convolution method is based on Lecomte (2008), where further elaboration of the method is provided. The method described here will be the method used for seismic forward modelling later in this thesis.

The 2(3)D wavelet used as input for 2(3)D convolution with a reflectivity model, is the PSF which is defined based on the survey geometry, background velocity model, pulse and wave-types (in this thesis only P-waves will be considered). Considering a source-receiver (SR) pair and an image point in the subsurface, the incident wave (between the source and the image point), and the scattered wave (between the image point and receiver), are described by slowness vectors p_S and p_R, respectively. A illumination vector I_{SR} is defined as the difference between the slowness vectors (figure 4.6-1):

$$I_{SR} = p_R - p_S. \tag{4.7}$$

The I_{SR} represents the normal to a potentially illuminated reflector. A survey of several SR-pairs generate a family of illumination vectors. This family of I_{SR} form the restriction bounds of which reflector can be illuminated. If there exists a reflector with a normal not covered by the calculated I_{SR} family, the reflector will not be illuminated.

If survey geometry, background velocity model etc. are not specified for a target (as in this thesis), a general span of I_{SR} are generated by defining an average background velocity, an incident angle and the steepest reflector dip to be illuminated. Based on these parameters, a symmetric cone will be created to represent a generic illumination vector range, where the length of this cone will be controlled by the velocity and incident angle (where a high velocity and/or incident angle will result in a shorter cone and therefore a poorer resolution) (Lecomte et al., 2016).

Multiplication of the illumination vector with frequency, f, gives the scattering wavenumber, k_{SR}:

$$k_{SR} = f I_{SR}. \tag{4.8}$$

A so-called PSDM filter will be created in the wavenumber domain by mapping the calculated scattering wavenumbers (corresponding to different SR-pairs) of the point to be imaged and using the amplitude spectrum of a selected pulse as weight for each k_{SR} (Lecomte et al., 2016).

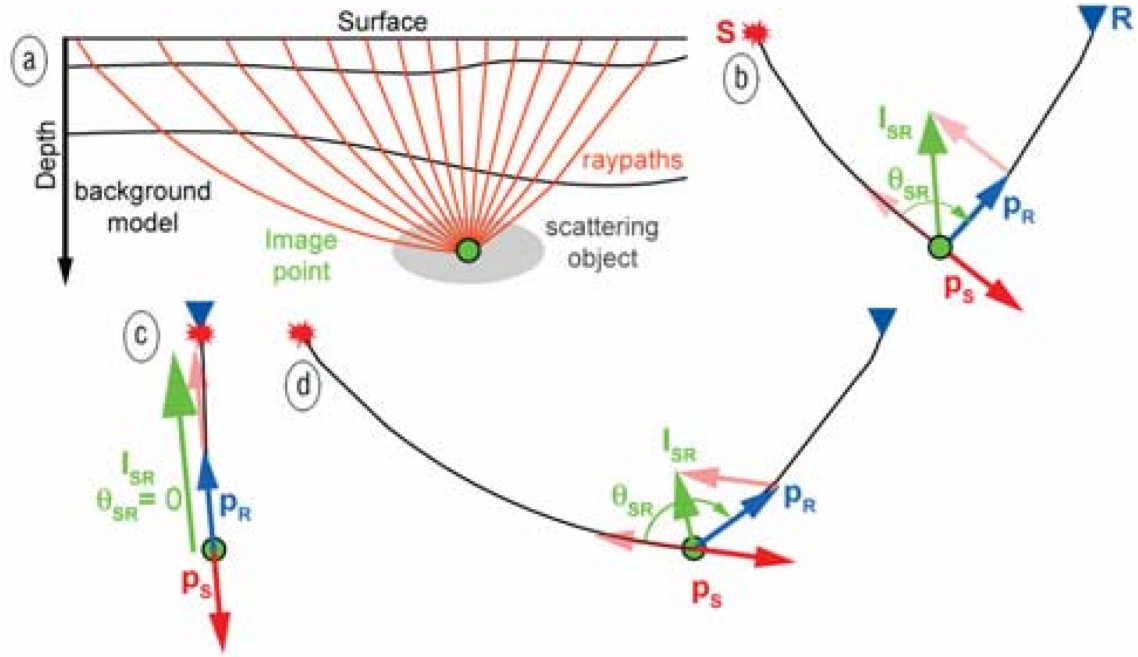

Figure 4.6-1: *Description of the illumination vector. a) Illustrate the different constituent affecting the calculation of the illumination vector, including a scattering object to be illuminated in the subsurface, a background velocity model with layering and different ray paths between the surface and the image point. b) Representation of the relationship between the illumination vector I_{SR} of a point in subsurface path between the source and receiver, with corresponding slowness vectors p_S and p_R and opening angle θ_{SR}. c) And d) illustrate a zero offset case and a large offset case, respectively, and how the length of the illumination vector is affected by offset. Zero offset causes a long illumination vector, while a large offset causes a short illumination vector. Longer I_{SR} cause a better resolution (Lecomte, 2008).*

These mapped and weighted k_{SR} represent the local illumination pattern and thickness of the corresponding scattering isochrone of a scattering point at the considered location in the spatial domain. The superposition of the different local shapes of the scattering isochrones in the spatial domain is obtained by applying a Fourier transform to the PSDM filter (figure 4.6-2). The result of that superposition is the PSF mentioned earlier. This provides a more efficient way of calculating PSF's instead of including time recordings for each point scatterer and performing a PSDM each time.

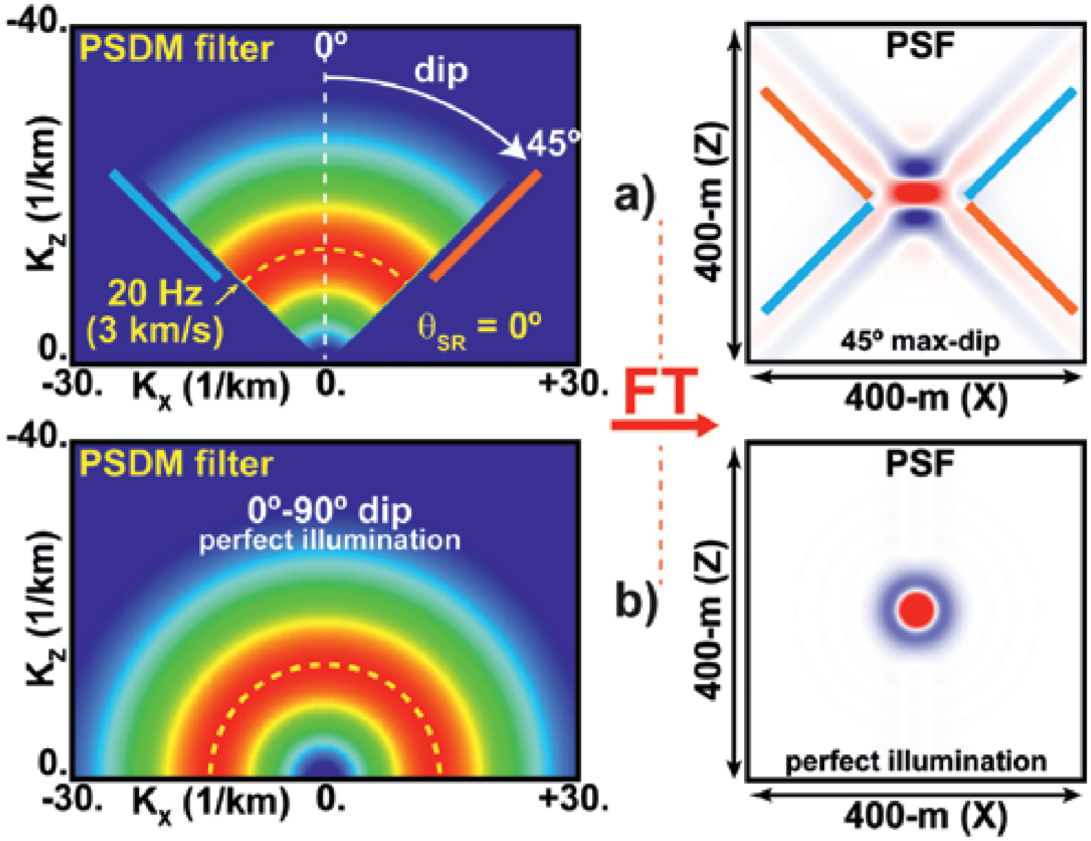

Figure 4.6-2: *a) Left: shows a PSDM filter in wavenumber domain with a frequency band where the dominant frequency is 20 Hz, the average velocity 3 km/s, the incident angel is 0° (zero-offset case), and maximum reflector dip to illuminated is 45°. Right: shows Fourier transform (FT) to spatial domain, which illustrates the PSF generated based on the PSDM-filter to the left. It is also possible to spot the relationship between the cross-pattern of the PSF in spatial domain with the maximum reflector dip in the PSDM-filter in the wavenumber domain (blue and red coloured lines are perpendicular to each other in space- and wavenumber domain). b) This illustrate the same mechanisms as in a), but using a perfect illumination case, where all possible illumination vector orientations are considered (0-90° dip) (Lecomte et al., 2016).*

The generated PSF is then either convolved with the reflectivity model in the spatial domain (figure 4.6-3), or the PSDM-filter is multiplied with the FT of a reflectivity model in the wavenumber domain.

The PSDM filter is multiplied with the reflectivity model in the wavenumber domain, which is an equivalent to the convolution between a PSF and reflectivity model in the space domain (figure 4.6-3). The PSF contains information about illumination and resolution based on the elements mentioned above, i.e., survey geometry, background velocity model, wavelet, etc. (Lecomte, 2008).

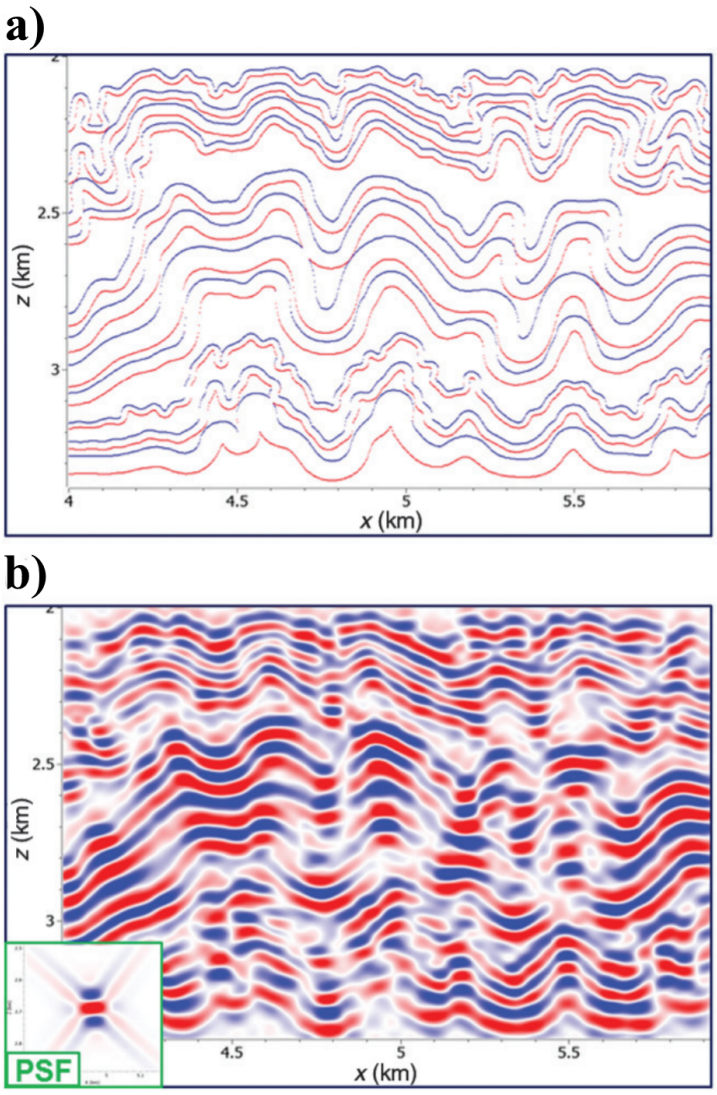

Figure 4.6-3: *Example from Lecomte et al. (2015), where the reflectivity (a) of a model containing folds, is convolved with a PSF (displayed in the bottom left corner in b), which results in a synthetic PSDM section (b).*

4.7 Previous work on seismic modelling of karst

There have previously been research on similar studies, where seismic modelling of karst features have been investigated.

Janson and Fomel (2011) presented a worklow for generating 3D synthetic seismograms for a 3D geocellular model, including a model of Lechuguilla cave. Unlike the ray-based modelling approach presented in section 4.6, Janson and Fomel (2011) used a more wavefield-based technique, where one simulates a propagating wavefield upward from each reflector in the impedance model, where the arrival time will be registered at the top of the model. Migration is then performed to obtain a 3D synthetic seismogram, where steep dips and rapid lateral velocity variations are realistically accounted for. The seismic modelling method is efficient, but since it includes synthetic trace modelling and then migration, it can not be as efficient as the 2(3)D convolution method described in section 4.6. Some of the results presented in Janson and Fomel (2011) from the seismic modelling of the cave, are displayed in figure 4.7-1.

Xu et al. (2016) went for a different approach by doing a physical (analog) modelling to study the seismic response of karst features, based on the karst reservoirs in the Tarim Basin in China. The materials that are used in the experiment to reproduce the correct elastic properties in a real karst feature, are a mix of epoxy resin and rubber to represent low-velocity cases, and a mix of epoxy resin with talcum powder to represent high-velocity cases. The amount of each constituent in the mix decides the elastic property. The scale factor of the model is set to 1:20 000 (1 mm in the model equals 20 m in a real scenario).

This approach leads to a more direct modelling approach. By including caves with different scales, velocities, shapes, fluids and spatial distribution, they investigated how the seismic response, represented as anomalous bright spots typical for carbonate karst reservoirs, changes with the different scenarios.

A brief comparison between the results presented in this study (which will be given in chapter 5) and the previous studies mentioned in this section (Janson and Fomel (2011) and Xu et al. (2016)), will be discussed later in this thesis.

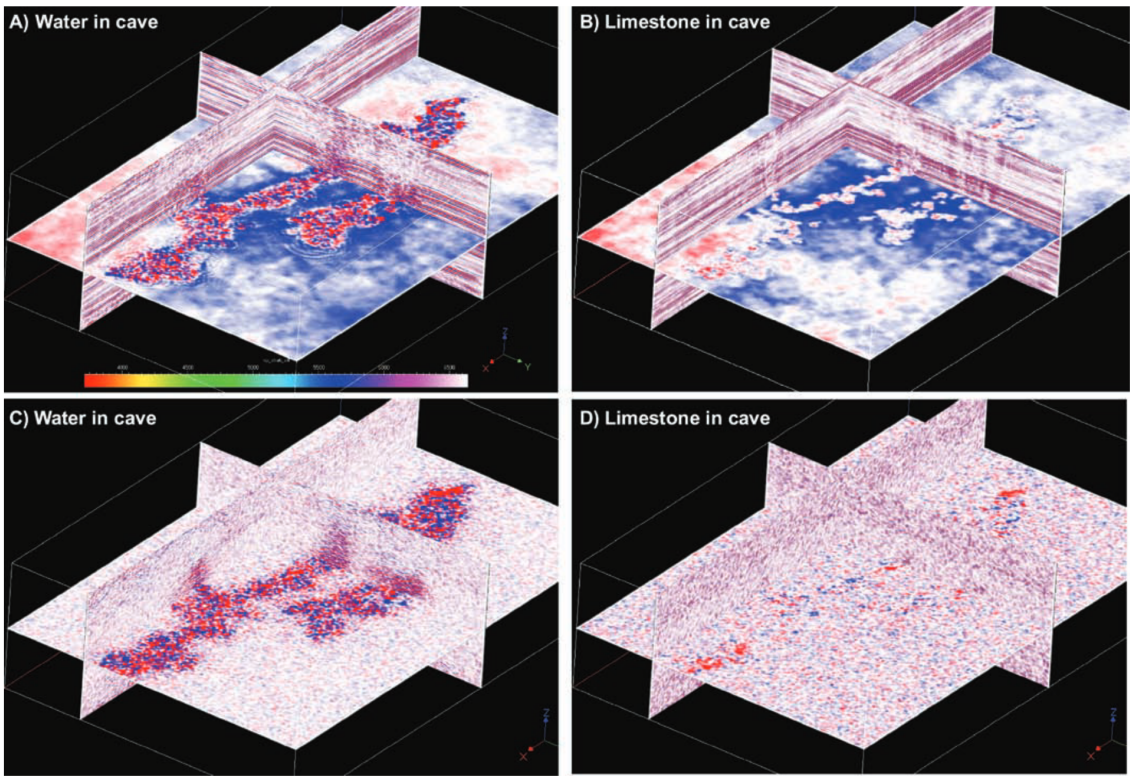

Figure 4.7-1: *Different results from the seismic forward modelling presented in Janson and Fomel (2011). (A) and (B) includes a layered background, while (C) and (D) have a stochastic background. (A) and (C) are cases where the cave is water-filled, while (B) and (D) are filled with limestone. The water-filled cases give a much higher impedance contrast, and the cave features are easier to distinguish, at least in the horizontal seismic section. In the case where the cave is filled with limestone material, it is more difficult to distinguish the cave from the surroundings, where the stochastic background case represent the most difficult (Janson and Fomel, 2011).*

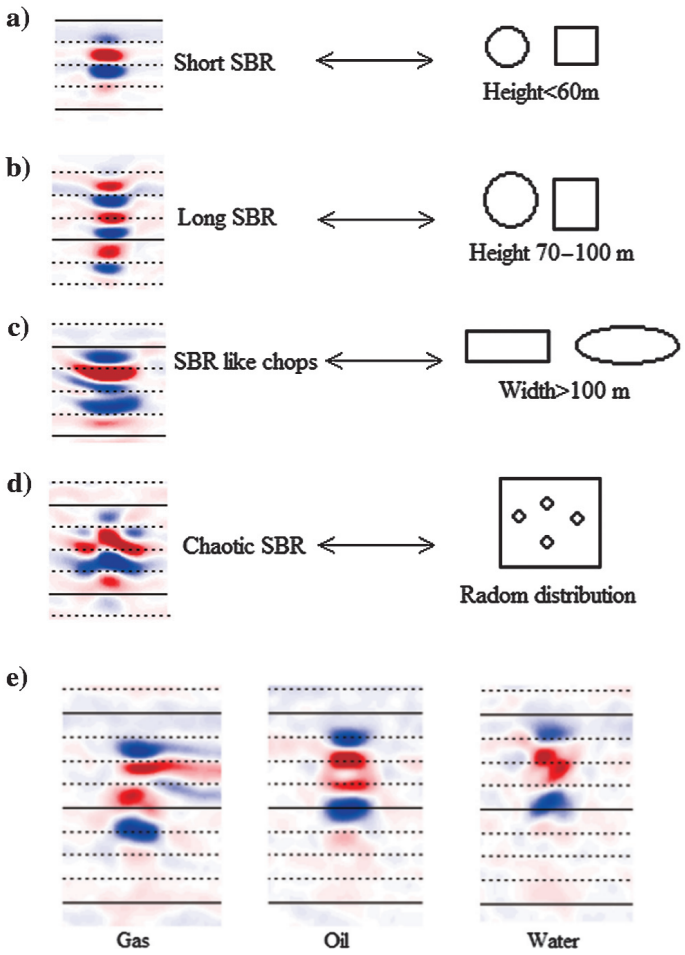

Figure 4.7-2: *Some of the results from Xu et al. (2016). The different cave structures, scales and shapes are displayed to the right of the arrow, while the corresponding seismic responses are displayed to the left. String of beads response (SBR) is a name for the anomalous bright spots typical for karst reservoirs. (a)-(c) displays the seismic responses of different shapes and sizes of the caves, while (d) shows a case of multiple caves where the distance between the caves is less than 100 m, which results in an interference. (e) displays a case of how the seismic response is affected by different fluid saturations (Xu et al., 2016).*

Chapter 5

Results

In this chapter, I will present my results from the rock physics modelling and seismic forward modelling. I have focused on two cave features, where one of them is an outcrop of a paleocave structure located in the Franklin Mountains in Texas, USA, and the second cave is a modern cave system called Setergrotta located in Mo i Rana, Norway. The geological model representing the Franklin Mountains paleocaves is based on the interpretations and some of the values presented in Målbakken (2009). Since the focus of this study is to present a workflow for modelling paleokarst reservoir features, the petrophysical properties used are simple estimates and not 100% exact.

The geological model with corresponding petrophysical properties representing the Franklin Mountains case was generated by adding the appropriate values to an image of the model using a MATLAB script developed by Dani Schmid (February 2016) and later modified by Isabelle Lecomte (March 2016). The script was later adapted (by the author of this thesis), to be able to account for the desired petrophysical properties.

The 3D model of the Setergrotta cave system has previously been developed and studied by Furnée (2015) and Ledsaak (2016), and is provided to this study through the research project called FOPAK (Forecasting of architecture, seismic characteristics and flow behaviour in paleokarst reservoirs). Further details about the model will be given in section 5.2.

The rock physics modelling script (ENTER) used in this thesis is provided by Åsmund Drottning (Rock Physics Technology), and is based on the Kite-model presented by Avseth et al. (2014), which is further described in section 3.5. A seismic modelling software called SeisRoX, developed by NORSAR, is used for the seismic forward modelling. SeisRoX is based on the 2(3)D convolution approach described in section 4.6.

5.1 2D model of the Franklin Mountains paleocaves

Introduction

The Great McKelligon Sag (GMS) is a large paleocave breccia structure located in the southern Franklin Mountains area, in West Texas (Loucks, 2007; Målbakken, 2009). The site contains outcrops of paleocave features including cave breccias, fractures and cave sediments, and is accessible to geologists for interpretation and mapping of the different cave facies. The Ordovician sequences in the Franklin Mountains is considered to be an equivalent to the Ellenburger Formation of the Permian Basin, which is a large hydrocarbon reservoir in West Texas (McDonnell et al., 2007; Målbakken, 2009).

For that reason, the paleocaves in the Franklin Mountains are of great interest in terms of simulating synthetic seismic of paleokarst to be able to understand seismic responses related to analogous reservoir types. Since information about porosity, geological constituents and paleocave structures can be derived from interpreting these outcrops, a more realistic model of the paleocaves can be achieved.

However, considering that the aim of this study is to develop a workflow for seismic modelling of paleokarst reservoir, and not a detailed investigation of the paleocaves in the Franklin Mountains, the properties added in the models are just simple assumptions and approximations mainly based on the information and interpretations provided by Målbakken (2009).

As a starting point for the modelling, I have used an illustration (figure 5.1-1) from Målbakken (2009), where the main composites of the paleocave are described. The illustration has been modified before imported into the MATLAB software (figure 5.1-2), where various petrophysical properties have been added to the background layers, and to the contents inside the paleocaves. The different constituents of the background stratigraphy are described in figure 5.1-3. The background lithologies including the paleocave fillings are also illustrated in figure 5.1-4a-c.

The chosen porosities are displayed in figure 5.1-5, where the properties are, as mentioned earlier, mainly assumptions and approximations based on the work of Målbakken (2009), and some additional information provided by Holtz and Kerans (1992), where data from the Ellenburger Group equivalent to the Franklin Mountains sequence are provided.

As seen in figure 5.1-6a and b, I have chosen to fill the paleocave features (including the crackle breccia) with oil, while the surrounding layers are brine saturated. This is for simplicity and the sake of illustration, although it is possible to distribute the fluids differently.

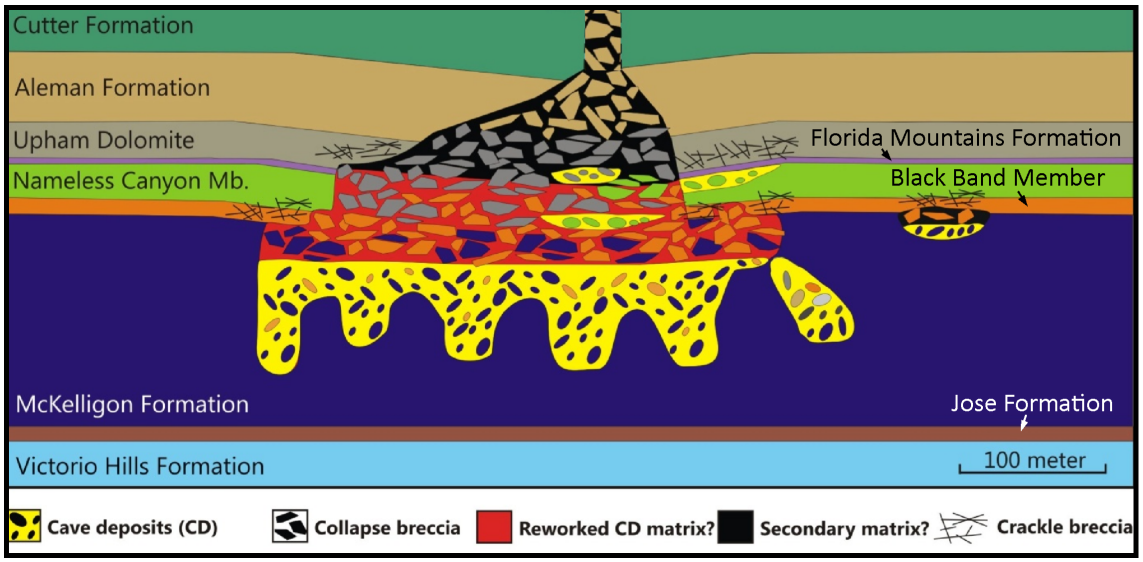

Figure 5.1-1: *Illustration of the paleocave showing the distribution of the various cave material, and the background stratigraphy with corresponding names. There is also a phreatic tube located to the right of the Great McKelligon Sag, which is included in the modelling (Målbakken, 2009).*

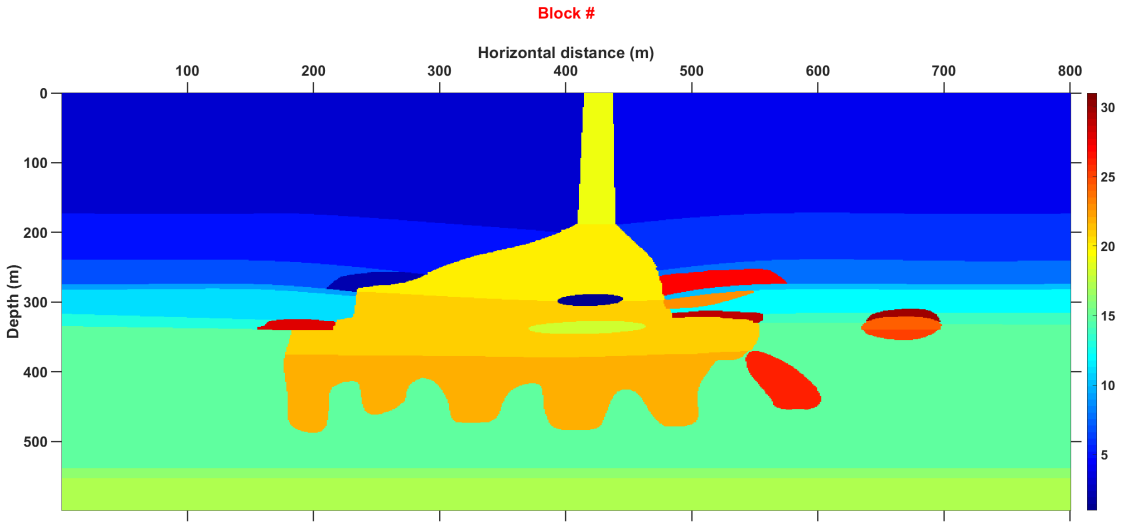

Figure 5.1-2: *An equivalent representation of figure 5.1-1, which has been imported and plotted in MATLAB. The different colours in this plot corresponds to specific block numbers (colour scale to the right). The model also includes the crackle breccia features displayed in figure 5.1-1.*

Period	Group	Units	Lithology
Silurian		Fusselman Dolomite	Dominantly Dolomite
Upper-Ordovician	Montoya Gp.	Cutter Fm.	Dominantly Dolomite
		Aleman Fm.	Carbonate & Chert
		Upham Dolomite	Dolomite
Lower-Ordovician	El Paso Gp.	Florida Mts. Fm.	Limestone & silisiclastics
		Nameless Canyon Mb.	Limestone & silisiclastics
		Black Band Mb.	Dolomite
		McKelligon Fm.	Limestone
		Jose Fm.	Dolomite
		Victorio Hills Fm.	Limestone
		Cooks Fm.	Dolomite
		Sierrite Fm.	Dolomite & silisiclastics

Figure 5.1-3: *Some of the different units and corresponding lithologies found in Franklin Mountains are listed under "Units" and "Lithology", where the red frame indicates the units that are included in the model described in this study. The second column from the left describes which group the different units belong to, and the first column describes which time period the different units were developed in (Målbakken, 2009).*

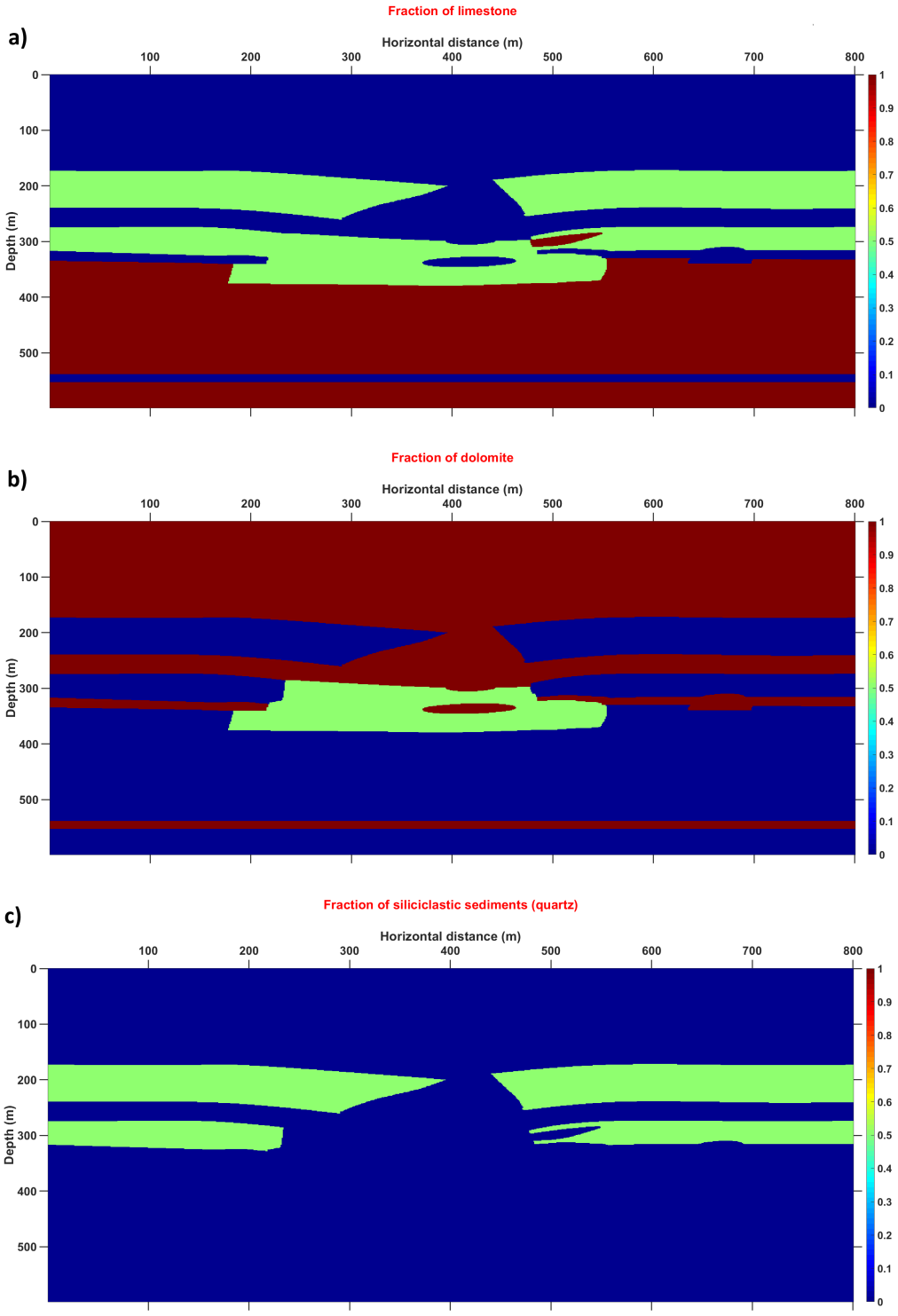

Figure 5.1-4: *(a)-(c) illustrate the distribution of the different lithologies in the paleocave model. These lithology descriptions are based on the information given in figure 5.1-3. (a) displays the fraction of limestone, (b) displays the fraction of dolomite, and (c) displays the fraction of siliciclastic sediments (quartz) in the model.*

Table 5.1-1: *The porosities of the background stratigraphic units used in the paleocave model.*

Background stratigraphy	**Porosity (%)**
Cutter Fm.	2
Aleman Fm.	4
Upham Dolomite Fm.	6
Florida Mts. Fm.	12
Nameless Canyon Mb.	8
Black Band Mb.	6
McKelligon Fm.	10
Jose Fm.	6
Victorio Hills Fm.	2

Table 5.1-2: *The various porosities inside the paleocave units. To locate the different porosity units mentioned below, refer to figures 5.1-1 and 5.1-5 for guidance.*

Paleocave units	**Porosity (%)**
Crackle breccias	15
Phreatic tube (upper part)	12
Phreatic tube (lower part)	3
GMS (upper part)	15
GMS (middle part)	17
GMS (lower part)	5
Various pockets inside GMS	5
Pocket outside GMS	4
Cave passage close to the lower part of GMS	7

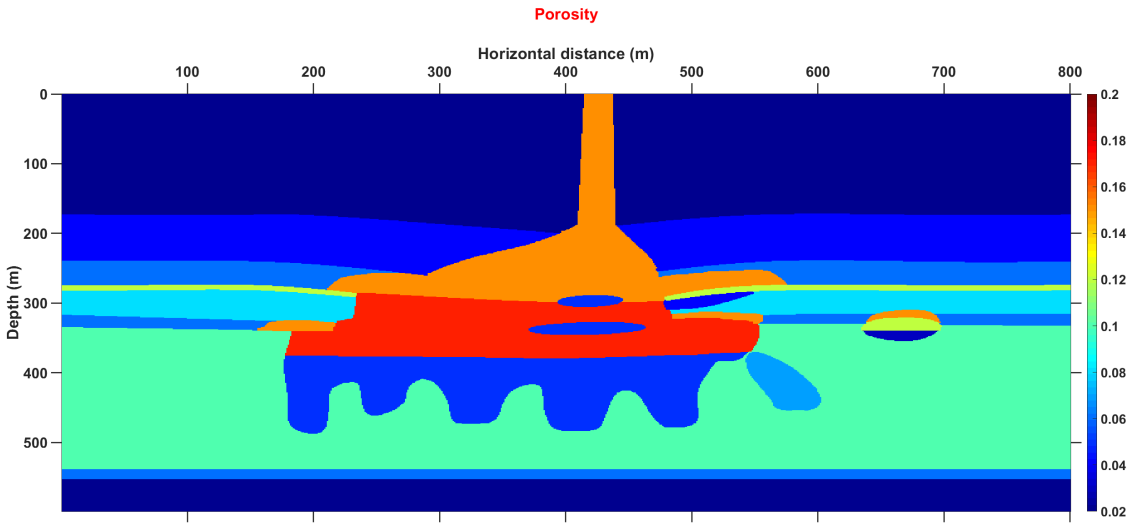

Figure 5.1-5: *The porosity distribution in the paleocave model. The porosities of the different units are further described in table 5.1-1 and 5.1-2.*

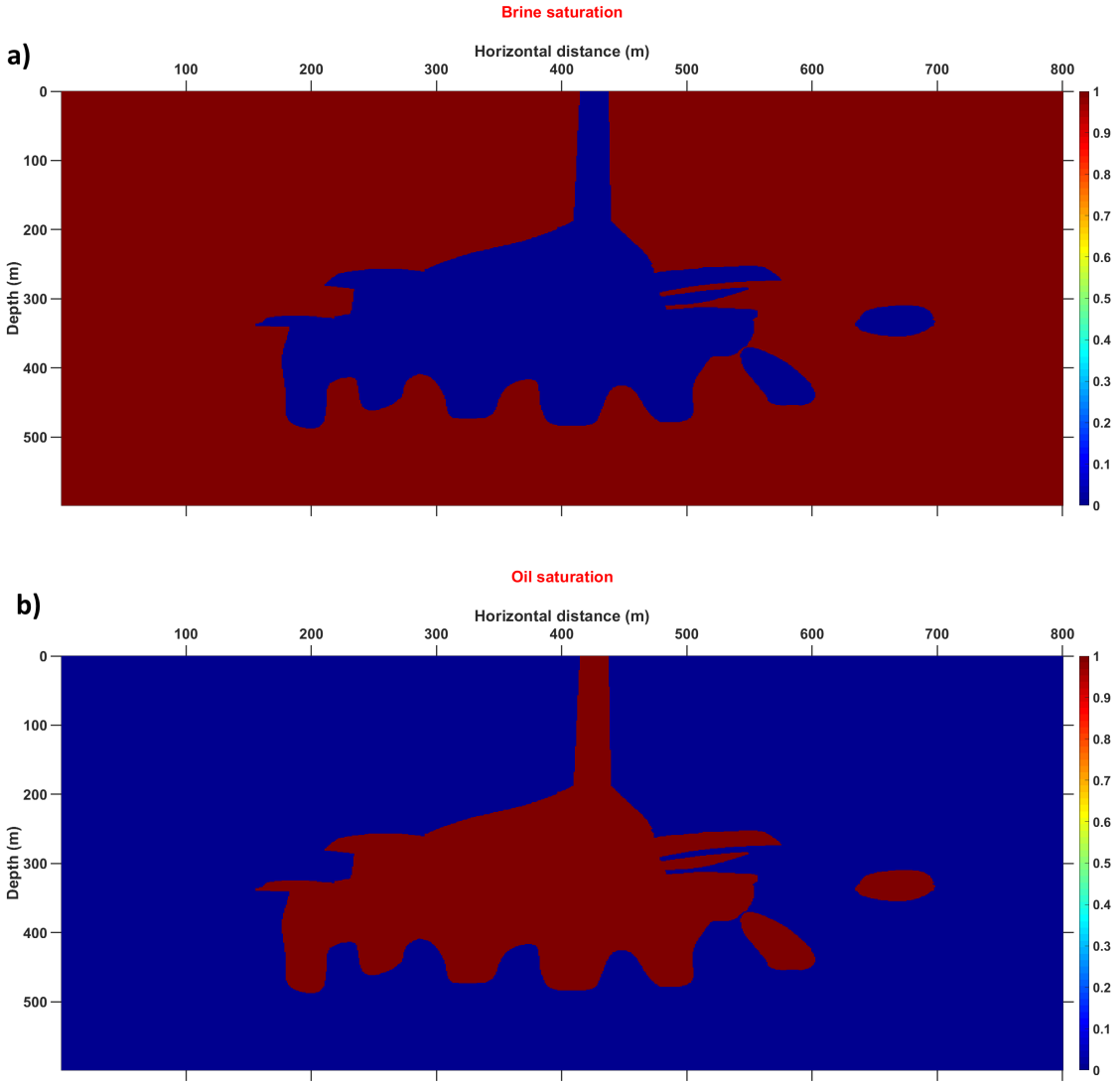

Figure 5.1-6: *The two figures above show the distribution of fluid saturations in the model. (a) displays the brine saturation, while (b) displays the oil saturation. Notice that the crackle breccias (showed in figure 5.1-1) and the phreatic tube (elliptical feature to the right) are also saturated with oil.*

Rock physics modelling

For the rock physics (RP) modelling of the 2D-model, I have considered seven different RP-models each describing a specific condition of the various model units. Each RP-model has a general set of parameters based on properties given in Avseth et al. (2014), where the critical porosity is considered to be 40% and cement volume fraction is 5%. The temperature, the pore pressure and effective pressure of the reservoir are set to 60°C, 20 GPa and 20 GPa, respectively. The critical porosity could be higher than 40% for carbonates, where a typical critical porosity for a limestone is considered to be 60% (Mavko et al., 2009). I have however chosen to stick with the properties presented in Avseth et al. (2014) for simplicity.

Table 5.1-3 provides information of the elastic moduli and densities of the solid grains for each composite. In this case, limestones consist of calcite minerals, dolomites of dolomite minerals and siliciclastics and chert consist of quartz minerals. The salinity of the brine is 5% and the oil reference density is equal to 0.8762 g/cm^3. Two different pore geometries (represented by the aspect ratio) can be considered within one RP-model, but to better visualize what effect each pore geometry has on the elastic properties, only one pore type is considered in each RP-model. Beyond these general settings, the characteristics of each model are described in table 5.1-4, and figure 5.1-7 shows which layers the different rock physics models are added to. Figures 5.1-8, 5.1-9 and 5.1-10 display the calculated bulk, shear and density plots, respectively, of the different RP-models described in table 5.1-4.

Table 5.1-3: *Elastic moduli and densities of the different minerals used in the rock physics modelling. The properties representing the calcite and dolomite minerals are from Sayers (2008), while the properties representing the quartz mineral are from Avseth et al. (2014).*

	Bulk modulus [GPa]	**Shear modulus [GPa]**	**Density [$\frac{g}{cm^3}$]**
Calcite	76.8	32.0	2.71
Dolomite	76.4	49.7	2.87
Quartz	36.0	44.0	2.65

The aspect ratio describes the pore geometry, where the low aspect ratio represents crack-like pores and high aspect ratio represents more spherical pores (intraparticle, vuggy and moldic pores). The aspect ratio ranges between three values (1.0, 0.1 and 0.01), which are based on the aspect ratios given in figure 3.5-4. The low aspect ratio (0.01) represents the crackle breccias (figure 5.1-1), the high aspect ratio (1.0) represents the paleocave interbreccia pores, while the moderate aspect ratio (0.1) represents the pores that occur in the background stratigraphy.

The low-porosity interval in the Kite-model is described by DEM theory. A maxi-

mum porosity of this low-porosity zone, called $\phi_{DEM,max}$, will vary in terms of which aspect ratio is considered in the model. This is because the inclusions (pores) more easily interact with each other in the case of low aspect ratio, which is a violation of the Kuster-Toksöz model assumptions used in the DEM modelling. Therefore, an aspect ratio of 1.0 corresponds to $\phi_{DEM,max}$=0.1, aspect ratio of 0.1 corresponds to $\phi_{DEM,max}$=0.05, and aspect ratio of 0.01 corresponds to $\phi_{DEM,max}$=0.02.

Table 5.1-4: *Short description of the main differences between the rock physics models used to compute the elastic properties of the 2D model of the paleocaves in the Franklin Mountains. Where there are two different lithologies within the same rock physics model, the amount of each lithology is divided equally (50%/50%).*

	Lithology	**Fluid saturation**	**Aspect ratio**
Model 1	Dolomite	100% oil	1.0
Model 2	Dolomite/Limestone	100% oil	1.0
Model 3	Limestone	100% oil	1.0
Model 4	Dolomite	100% brine	0.1
Model 5	Dolomite	100% oil	0.01
Model 6	Limestone/Siliciclastic (quartz)	100% brine	0.1
Model 7	Limestone	100 % brine	0.1

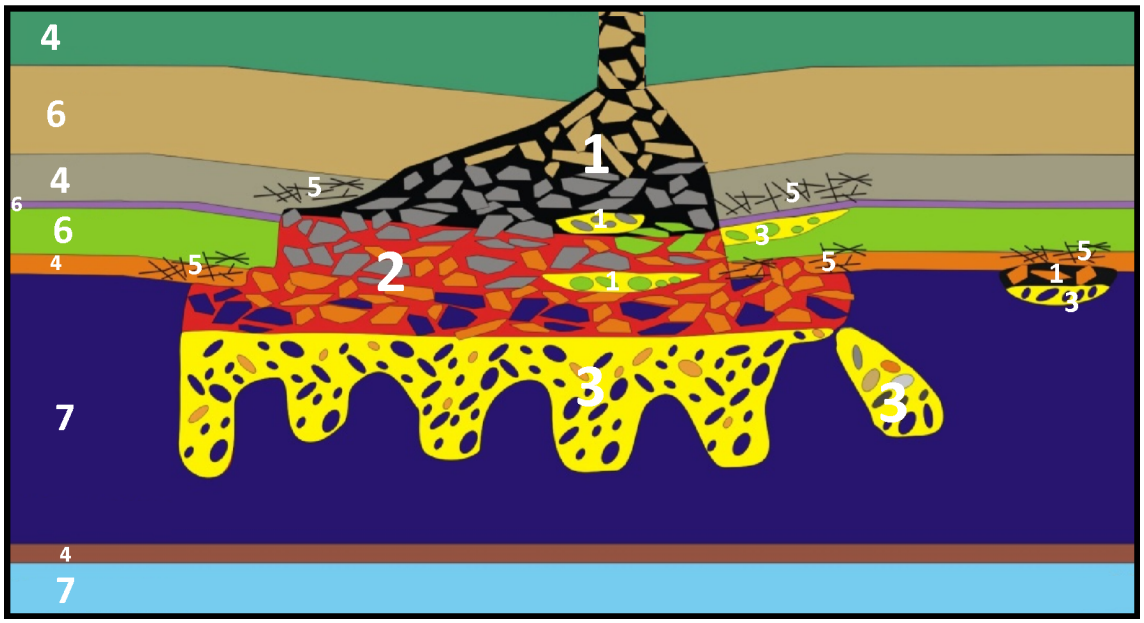

Figure 5.1-7: *The image shows which units the different rock physics models are added to. The white numbers correspond to the various model numbers given in table 5.1-4. Modified from (Målbakken, 2009).*

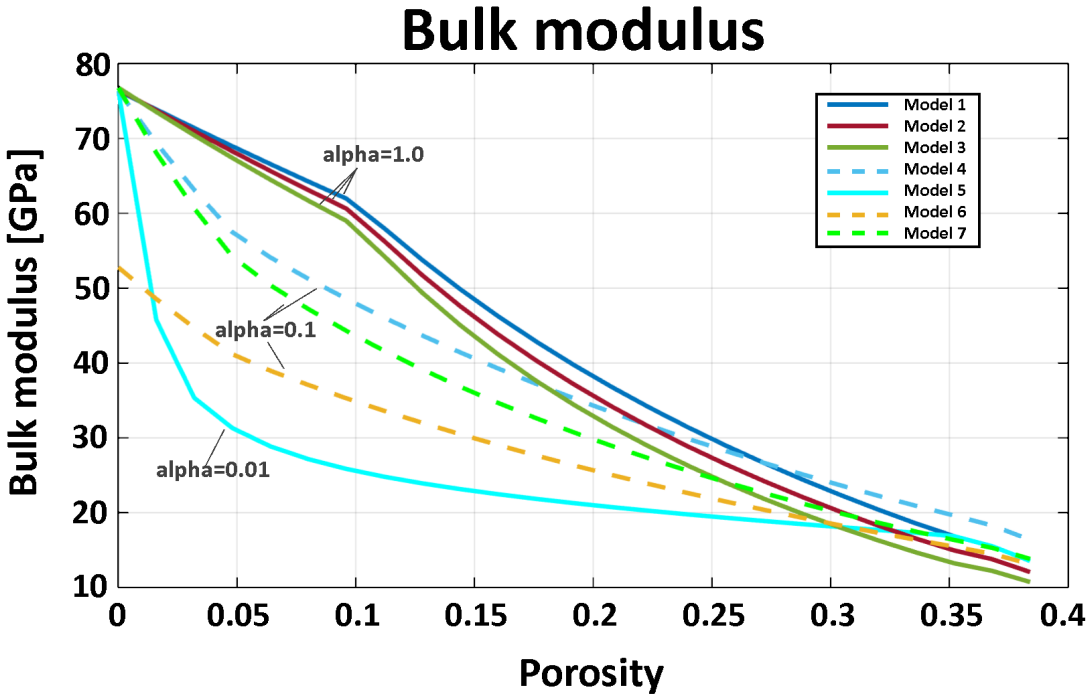

Figure 5.1-8: *The figure describes the bulk modulus versus porosity for the different rock physics models presented in table 5.1-4. The solid lines represent oil saturation, while the dashed lines represent brine saturation. The different aspect ratios are represented in the figure as alpha = 1.0, 0.1 and 0.01. Note the huge impact the pore geometry has on the bulk modulus when comparing Model 1 with Model 5, where both represent a oil saturated dolomite, but where Model 1 has an aspect ratio of 1.0, while Model 5 has an aspect ratio of 0.01.*

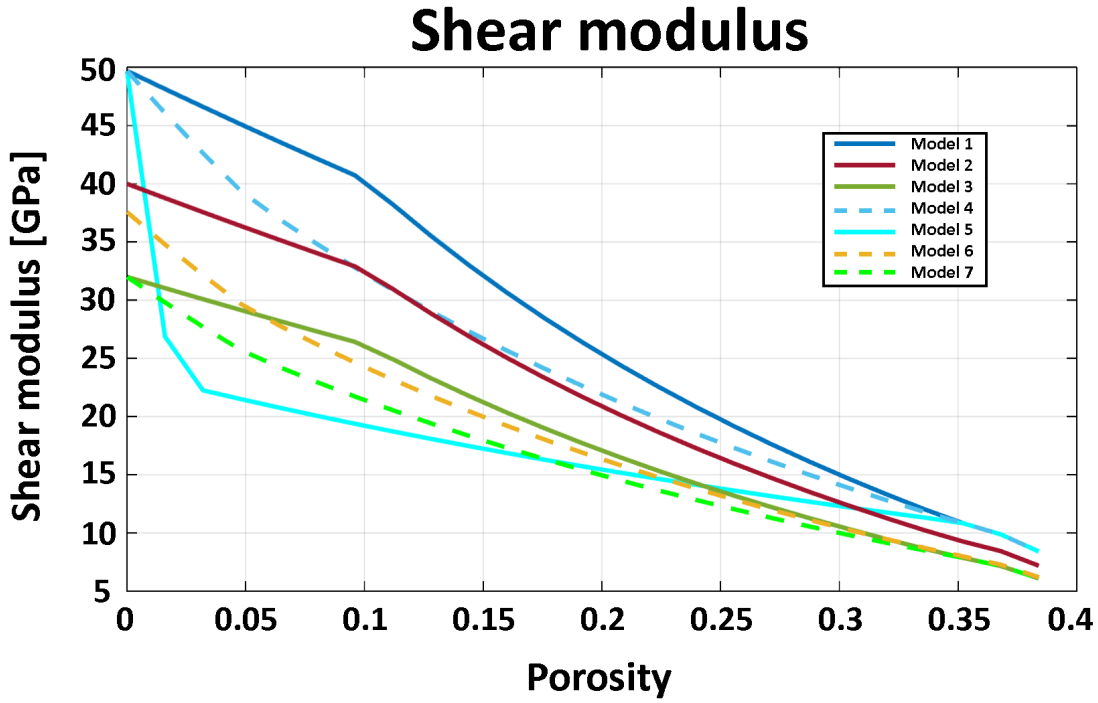

Figure 5.1-9: *The plot describes how the shear modulus changes in terms of porosity. Like in figure 5.1-8, the pore geometry has the largest impact on the shear modulus. Table 5.1-4 provides further details of the different rock physics models described in the figure.*

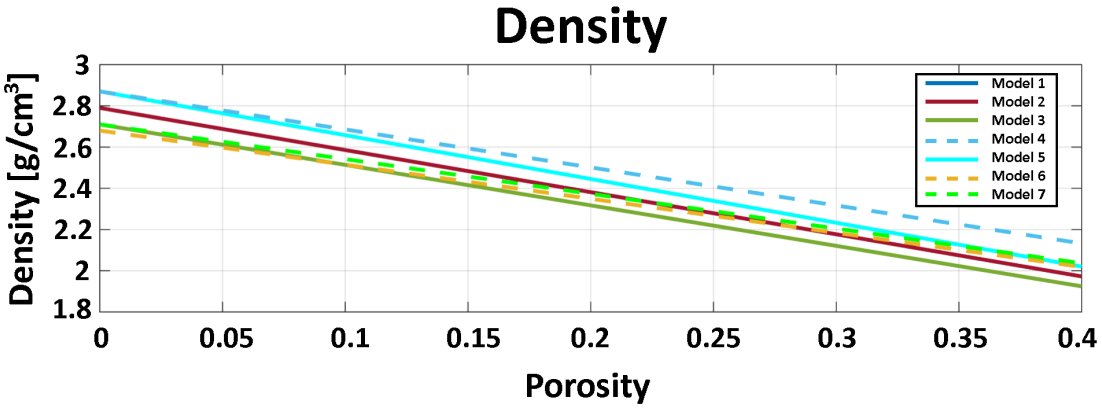

Figure 5.1-10: *The figure shows the density versus porosity. Unlike the bulk and shear modulus, the density is not affected by different pore geometries.*

Seismic forward modelling

The computed elastic properties, obtained from the rock physics modelling represent the input values to the seismic forward modelling. Table 5.1-5 provides the properties used in the calculation of the PSF (figure 5.1-14) that the 2D paleocave-model is convolved with, which includes restriction of illumination due to a conceptual survey scenario.

The chosen peak frequencies of 30 Hz and 60 Hz are based on the seismic modelling of paleokarst done by Janson and Fomel (2011). In the seismic survey described in Zeng et al. (2011b), the dominant frequency was characterized as 25 Hz at depths between 5650 to 6400 m, which are quite deep. Xu et al. (2016) also used a dominant frequency of 25 Hz in a physical modelling of seismic features representing the same paleokarst reservoir as Zeng et al. (2011b) (depths between 5500-6400 m). Based on these studies, the chosen peak frequency of 30 Hz, used in the present work, seems reasonable. The 60 Hz scenario is considered to give a comparison to the more low resolution case of 30 Hz.

Table 5.1-5: *Properties used in the seismic forward modelling. Maximum reflector dip describes the steepest feature that will be illuminated in the synthetic seismic. The average velocity in target model is an approximate estimation of the average velocity in the background velocity model. Only zero offset cases are considered in this study. The Ricker wavelets with peak frequencies of 30 and 60 Hz are chosen for this study. Only P-wave reflections are considered.*

Maximum reflector dip	45°
Average velocity in target model	5.5 km/s
Incident angle	0°
Wavelet	Ricker: 30 Hz and 60 Hz
Reflection mode	P-P

The results of the seismic forward modelling for the 2D Franklin Mountains model will be presented as two main cases. In the first one, the focus will be on the palocaves in the model, while all the background layers will consist of the same petrophysical properties, and therefore also the same elastic properties (figure 5.1-11a). In the second case, the background layers will be included and represent different petrophysical and elastic properties (figure 5.1-11b). Both cases will also be displayed with noise, where a signal-to-noise (S/N) ratio equal to 2 will be considered.

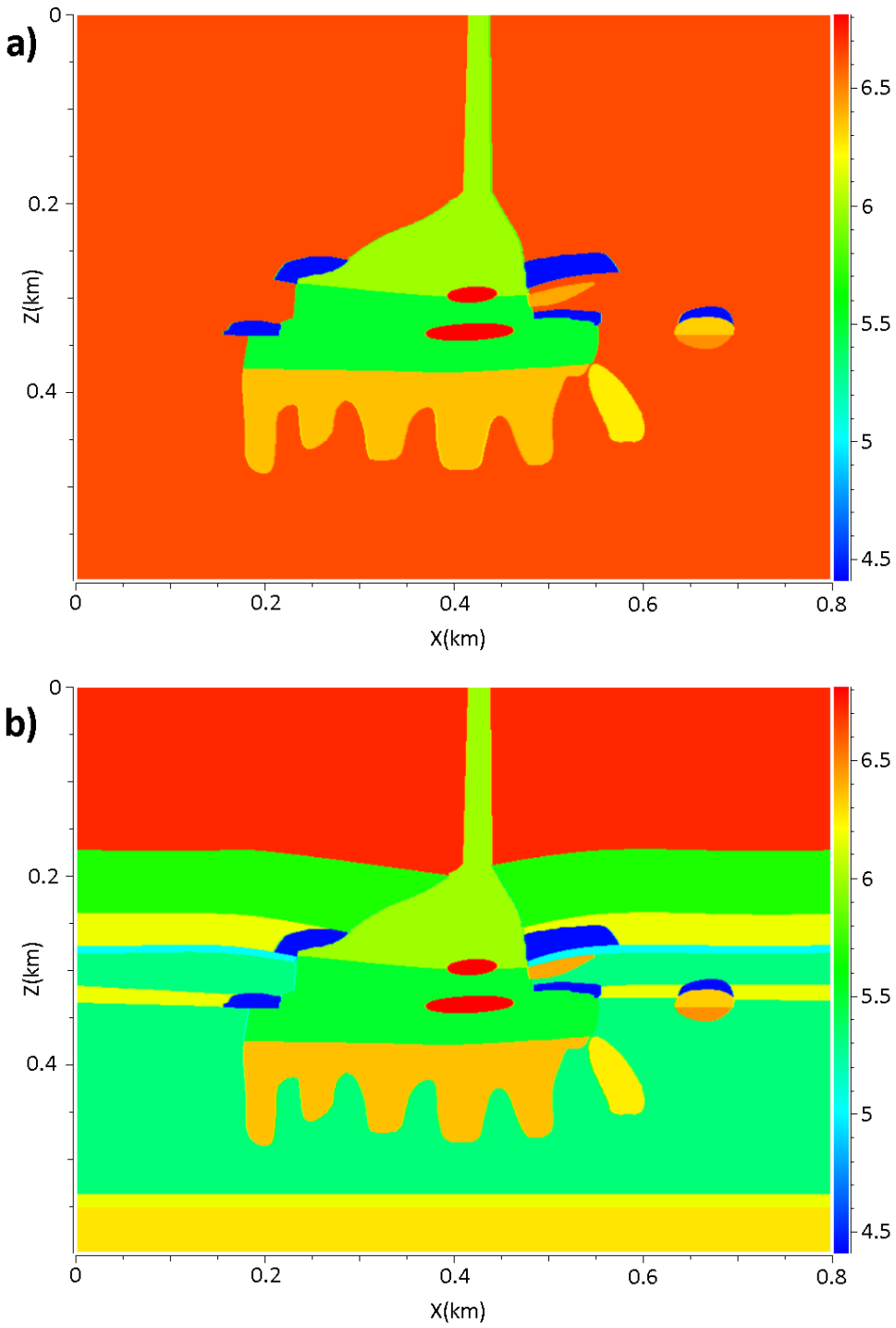

Figure 5.1-11: *P-wave velocity derived from the rock physics modelling of the Franklin Mountains paleocaves, where (a) represents the model without the background layers, and (b) represents the model where the background layers are included. The crackle breccia features represent the lowest p-wave velocity, while the low porosity pockets inside the paleocave (cave sediments) represent the highest p-wave velocity (applies both for a and b).*

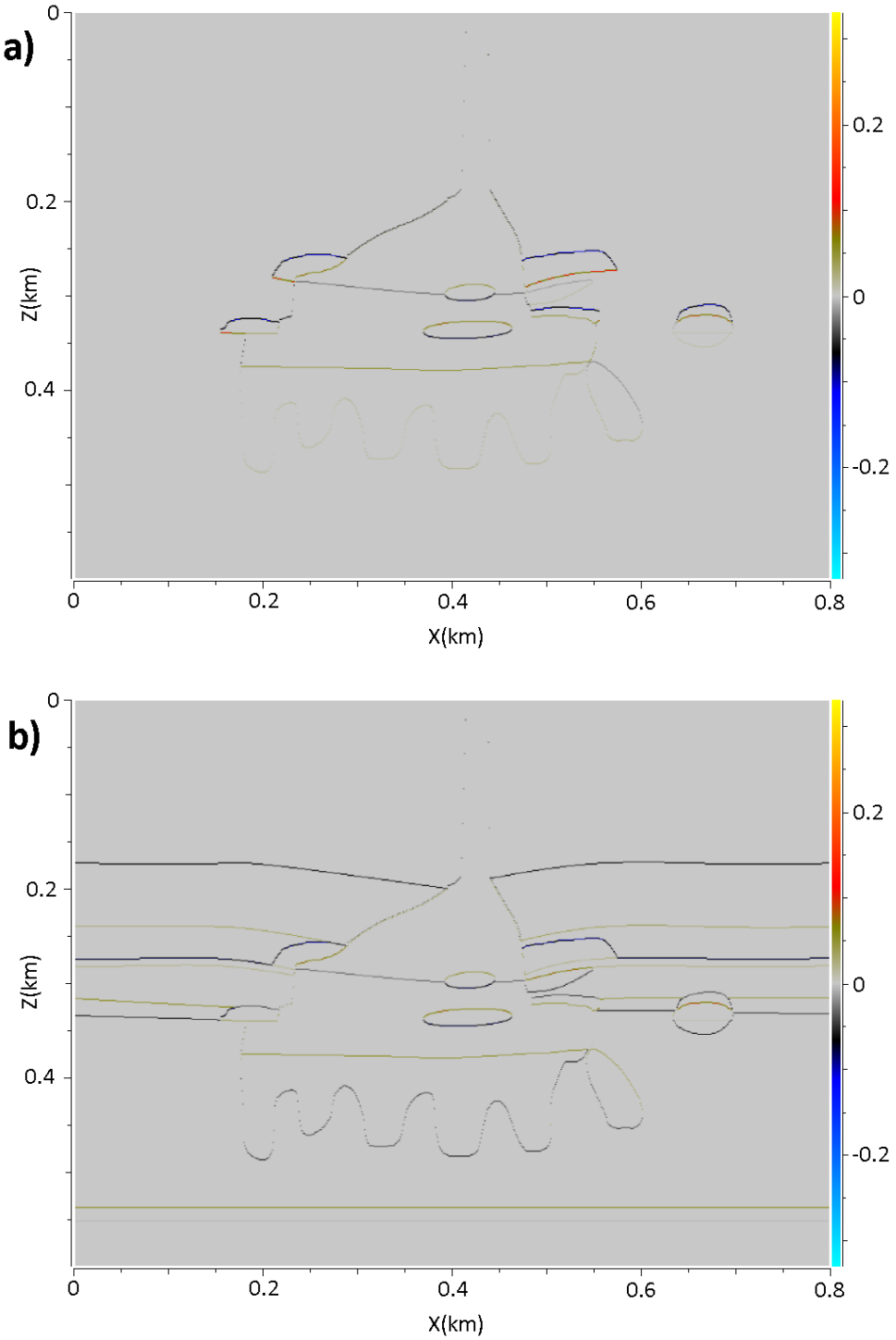

Figure 5.1-12: *Figure (a) and (b) display the reflectivity of the the Franklin Mountains paleocave model, where (a) shows the case where there are no background layers, while (b) represent the case including the background layers. By introducing the background layers, the reflectivity changes due to different impedance contrast since layers above the previously higher contrast now consist of different physical properties.*

The reflectivity model in figure 5.1-12a, reveals a high negative reflectivity between the surroundings and the top of the crackle breccia features. This is due to the lower elastic properties of the crackle breccias, where there is a higher porosity, and a low aspect ratio representing the pore geometry.

The high negative reflectivities presented in figure 5.1-12a, are not that dominating in figure 5.1-12b, where background layers of various porosities and mineral constituents are introduced. The change in reflectivity strength is displayed in figure 5.1-13a and b for the phreatic tube (small cave). There are also some features that change reflectivity from positive to negative and vice versa when background layers are added to the model, such as the down-cutting vadose features (horizontal wiggly feature) located at the bottom of the paleocave in figure 5.1-12a and b, and the bottom part of the phreatic tube displayed by the black arrows in figure 5.1-13a and b.

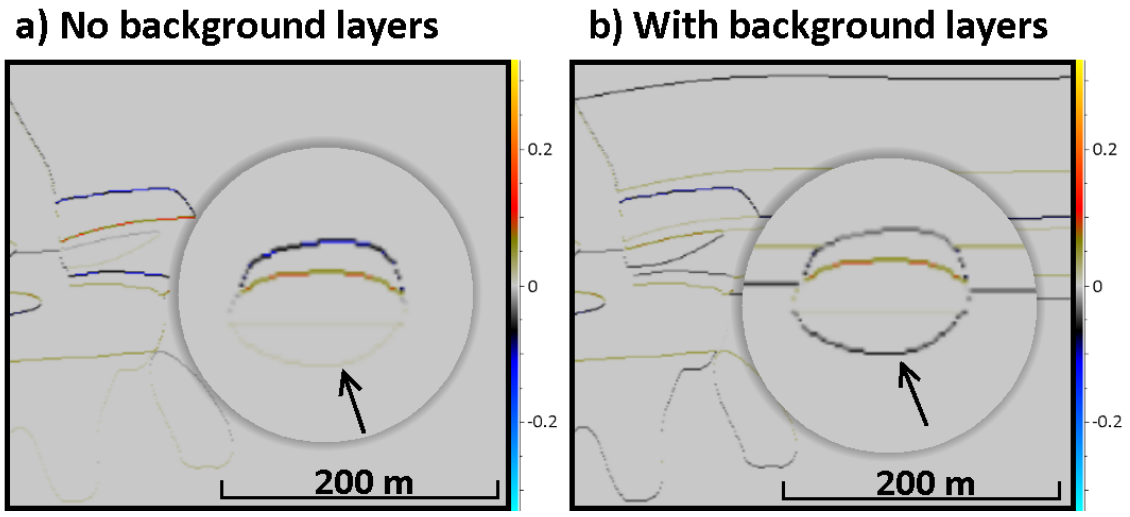

Figure 5.1-13: *An enlarged version of figure 5.1-12, where (a) and (b) in this figure correspond to (a) and (b) in figure 5.1-12, respectively. The figure illustrates how the reflectivity of the phreatic tube changes due to the modification of the elastic properties representing the background. The reflectivity changes both on top and bottom of the phreatic tube when background layers are added to the 2D model. The arrows indicate a polarity change.*

To obtain synthetic seismic, a 2D convolution between the reflectivity model and the designed PSF (figure 5.1-14a and b) has to be carried out. The output synthetic seismic are displayed in figures 5.1-15, 5.1-16 and 5.1-17, where both cases of not including and including the background layers are presented.

These figures all represent cases where the seismic has been calibrated with the corresponding reflectivity model, to be able to interpret the results with a fixed scale range, which makes it easier to compare the amplitude of the synthetic seismic with the reflectivity, and therefore make reasonable quantitative observations between them. The PSF's displayed in the following figures are not calibrated, but only there to illustrate the shape and size.

The calibration was done by generating a reference horizontal surface with the same input modelling parameters as for the considered seismic model. The reflectivity of this reference surface was equal to one. The corresponding maximum amplitude of the synthetic seismic of this reference surface was further used for calibration computation, where the seismic amplitudes of the considered and more advanced model, were divided by the reference seismic amplitude. This resulted in a calibrated synthetic seismic.

The comparison between the reflectivity and the seismic output shows that the seismic is stronger than the reflectivity in some areas, which is due to a constructive interference phenomena.

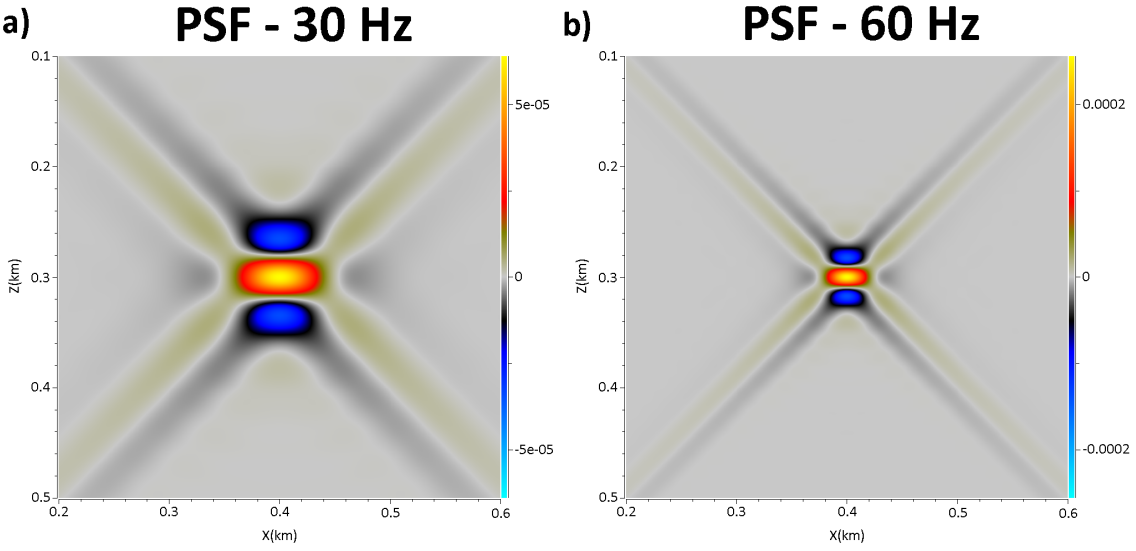

Figure 5.1-14: *Figure (a) and (b) illustrates the PSF calculated based on the values presented in table 5.1-5, where (a) represents the 30 Hz case and (b) represents the 60 Hz case.*

Figure 5.1-15 and 5.1-16 represent synthetic seismic of the 30 Hz PSF case, while figure 5.1-17 shows the synthetic seismic where the 60 Hz PSF is considered. A background noise is included in figure 5.1-16 and 5.1-17 to make it more realistic and to see if it has an effect on the output syntetic seismic. This is done by generating white random noise (Gaussian distribution) over the same target area as the considered model, then that noise is "PSDM-coloured" by filtering it with the same PSDM filter, i.e. having the same frequency range that the modelled seismic and the same illumination/resolution pattern (Lecomte, pers.comm).

The 30 Hz synthetic seismic in figure 5.1-15 and 5.1-16 represent a low resolution case of the 2D paleocave model, and small details are hard to distinguish, especially for the case including background layers. However, it is possible to observe certain characteristics and a weak rendering representing the structure of the GMS-paleocave, including the in case with background layers.

The pink box in figure 5.1-15, which represents the phreatic tube from the 2D paleocave-model, illustrates that it is possible to recognize an event in the synthetic seismic causing a small sag in the case where the background layers are included. The strong event in figure 5.1-15a (green box), which represents a crackle breccia feature, becomes much weaker in figure 5.1-15b, though it is possible to notice that an event breaks with the layering trend, observed as a small uplift.

The added noise in figure 5.1-16 does not seem to have any crucial effect on the interpretation of the synthetic seismic, other than possibly making the seismic look more "realistic". The only features that seems to be affected are the down-cutting vadose features at the bottom of the GMS-paleocave in figure 5.1-15a, which more or less disappear when the noise is added to the seismic, though these events were quite weak without the noise as well.

Considerably more details can be distinguished in the synthetic seismic for a 60 Hz PSF case, presented in figure 5.1-17, compared to the 30 Hz cases. The seismic events in the case without background layers are interpretable even when the background layers are included and despite of the noise. The phreatic tube can almost be distinguished as an elliptical feature when there are background layers. As mentioned earlier in this thesis, paleokarst and paleocave features are often characterized by separated bright spots on actual seismic, nearly appearing as scattered PSF-like seismic features more or less chaotically distributed. Similar features are observed in the 60 Hz synthetic seismic, especially when the background layers are not included. This can also seen in the 30 Hz synthetic case, where the background lithologies are not included.

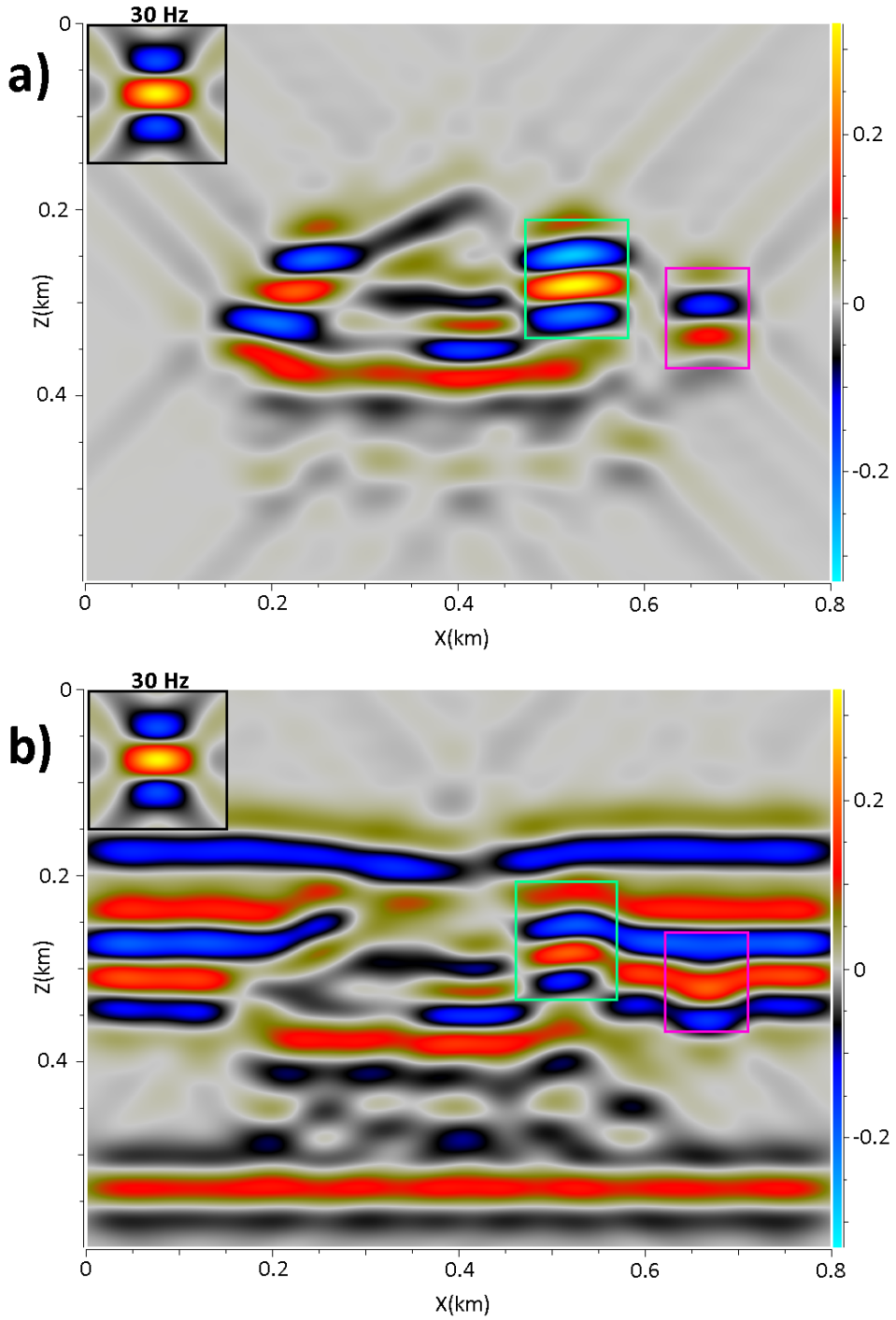

Figure 5.1-15: *The figures display synthetic seismic of the case where the reflectivity is convolved with the 30 Hz PSF (displayed in the top left corner of the figure). (a) represents the case where no background layers are included, while (b) displays synthetic seismic where different background lithologies are included in the model. The green and pink boxes indicate areas where the seismic clearly has been affected by the addition of different background lithologies.*

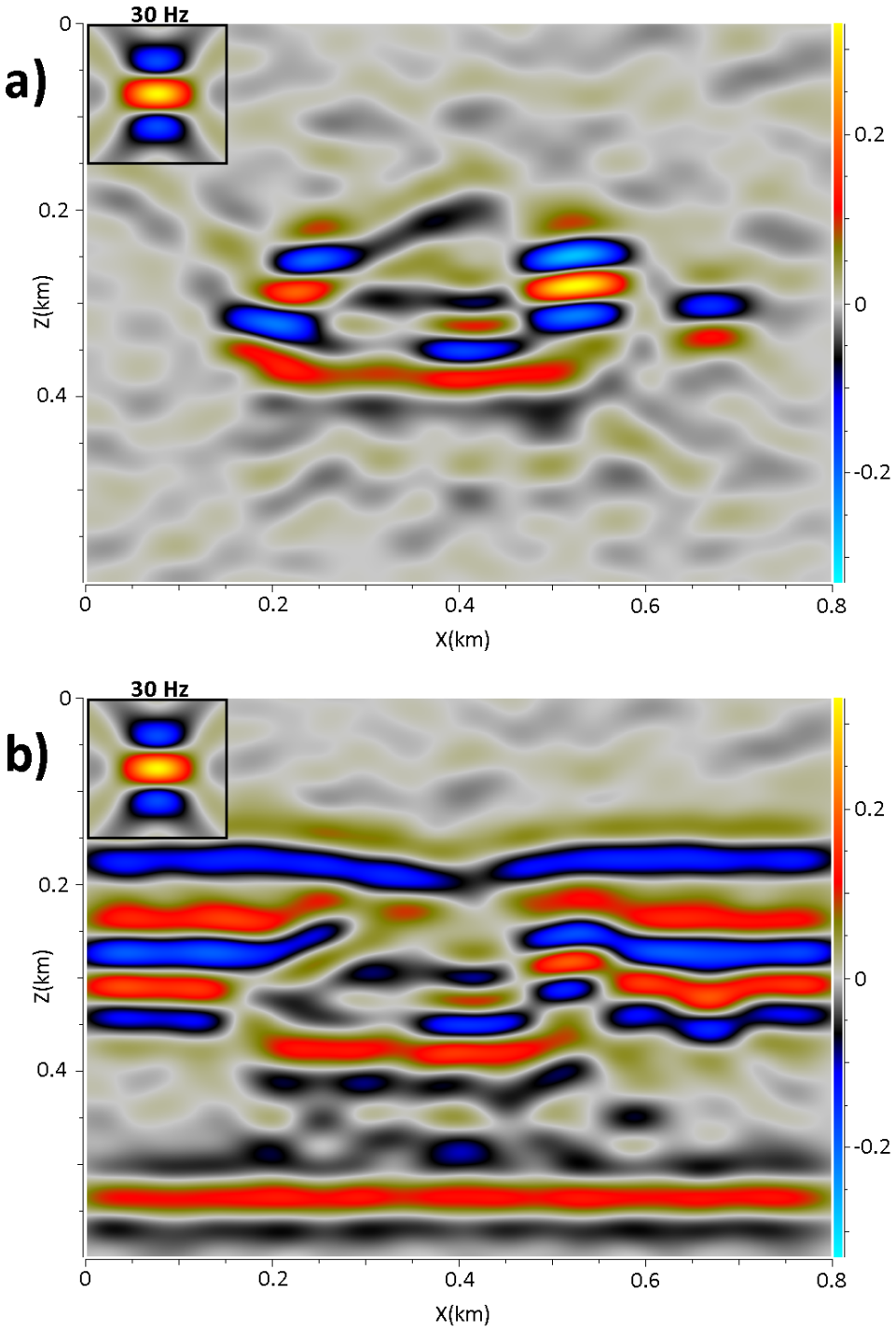

Figure 5.1-16: *The figure illustrates the same synthetic seismic as in figure 5.1-15, but in this case, random noise has been added to the model. The strength of the added noise has a S/N ratio equal to 2.*

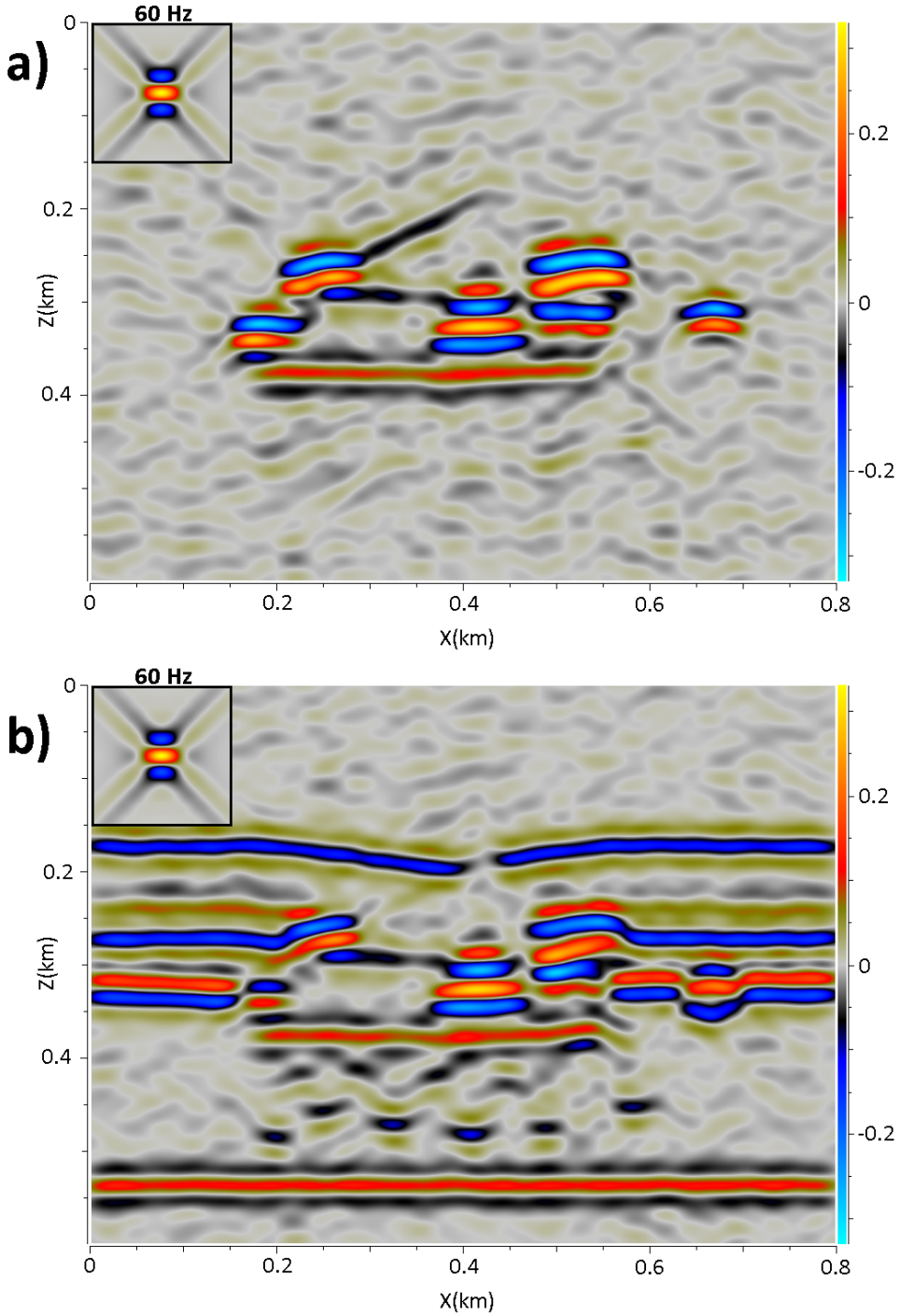

Figure 5.1-17: *The synthetic seismic in the figure is the output of a 2D convolution between the reflectivity model and the PSF of 60 Hz, which is displayed in the top left corner of the figure (with the correct scale). (a) represent the case without background layers, while (b) represent the case with background layers. Backround noise is added to the model, where a S/N ratio of 2 is considered.*

Figure 5.1-18 shows a case where the reflectivity model and the corresponding synthetic seismic are displayed with a superposition plot. This is included to illustrated how the seismic is related to the corresponding reflectivity model. The reason for not displaying calibrated plots is because the superposition option in SeisRoX only work for the direct results of modelling, and not for the calibrated versions, which are obtained via another option.

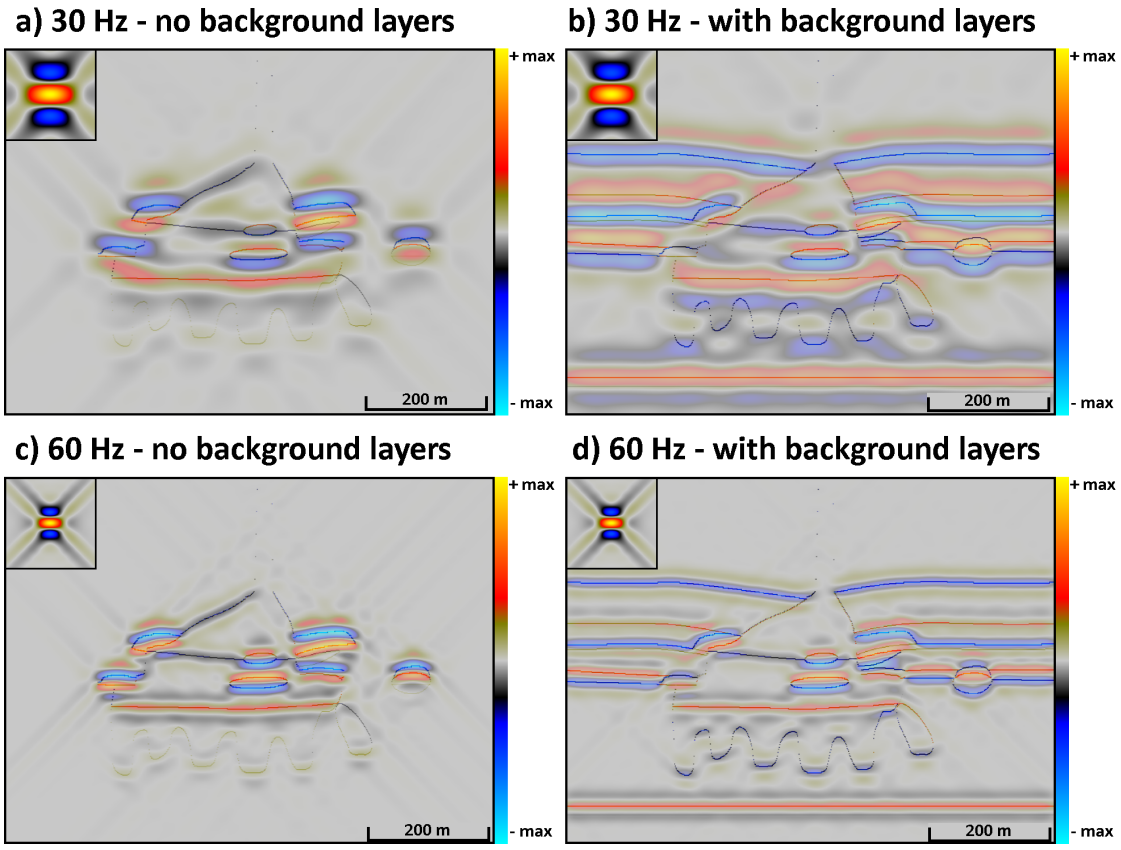

Figure 5.1-18: *The figure illustrates dual plots (superposition plots) of various scenarios, where (a) and (b) represent 30 Hz seismic plotted with the corresponding reflectivity model, while (c) and (d) represent 60 Hz seismic plotted with the reflectivity models. (a) and (c) display the cases where the background layers are not included, while (b) and (d) show the cases where the background layers are included. The scale ranges between the positive maximum absolute value to the negative maximum absolute value (from +max//value// to -max//value//).*

The 2D synthetic seismic images presented in this section have been derived from an image of a paleocave-outcrop. In the following section, a 3D reservoir model of a modern cave system will be presented.

5.2 3D model of the Setergrotta cave

Introduction

The Setergrotta cave is a large cave system located in Mo i Rana, Norway. The cave consists of marble (metamorphosed limestone) and is approximately 3 430 m long (Lauritzen et al., 2005). By using this modern cave system as a basis for seismic modelling of a paleokarst reservoir, a realistic cave geometry can be considered in the modelling procedure in a first attempt, though actual (paleo)karst systems are in practice more complex networks than just one cave system.

The input 3D model of the Setergrotta cave used in this study is a geocellular model developed in the reservoir modelling software RMS (Furnée, 2015; Ledsaak, 2016).The model of the cave has been subjected to a collapse simulation, yielding an expanded paleocave zone filled with collapse material. A fracture model has been added to the 3D model to account for the distribution of fractures which are common in carbonates, especially related to karst systems (Furnée, 2015; Ledsaak, 2016).

The model was implemented by (Furnée, 2015) and further studied by (Ledsaak, 2016). The input 3D model was provided to this study as a SEG-Y file through the FOPAK-project. The input model of the cave system contains information about porosity and pore pressure. The geometry of the cave system is described in 36 different horizons each representing a slice of the total 3D cave volume.

For the rock physics modelling part, two scenarios will be first considered and a brief comparison between these scenarios will be given, before one of these cases will be investigated further under the seismic forward modelling segment. For the seismic modelling part, a closer investigation of one seismic scenario will be considered. Afterwards, a last comparison will be provided, where the main case will be compared with a high resolution case, and with another modelling approach (1D convolution), to illustrate the benefits with a 2(3)D convolution modelling approach.

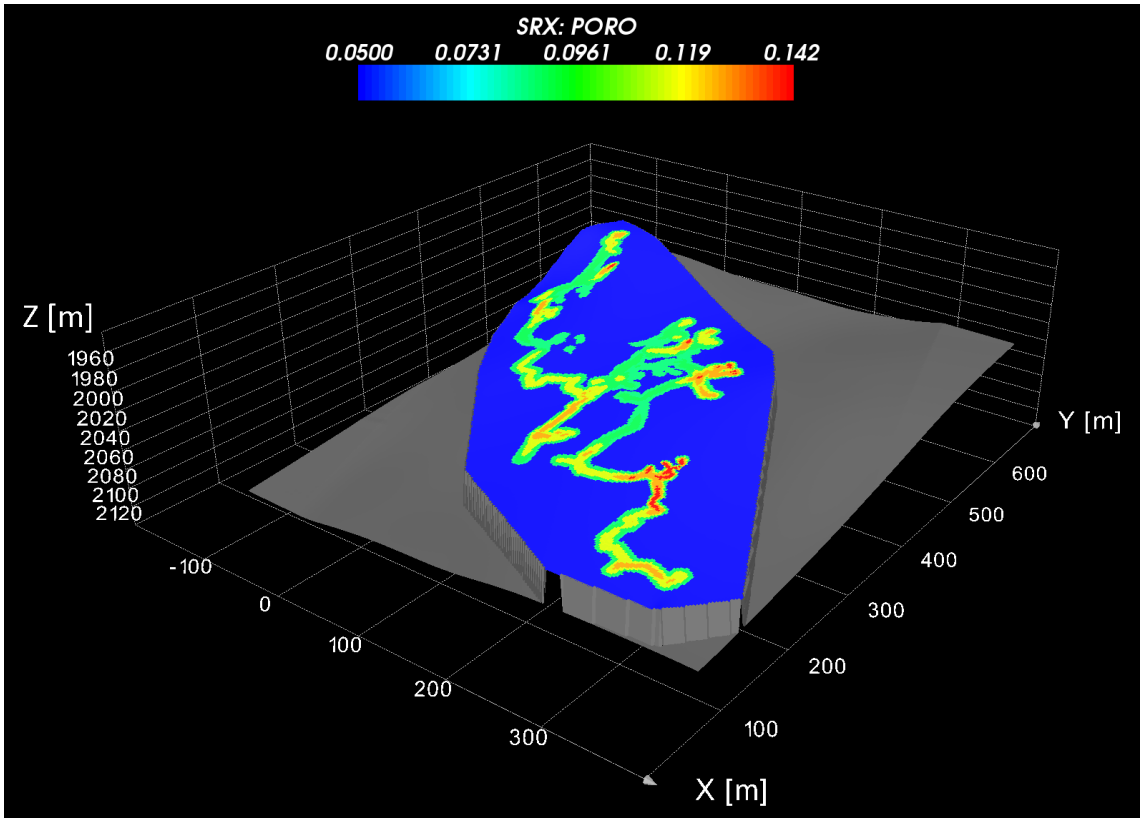

Figure 5.2-1: *The figure illustrates the porosity distribution in the Setergrotta cave model. The porosity is clearly higher (up to 14.2%) where the collapsed cave passages are located, and much lower outside the collapsed passages, where the porosity is approximately 5%. The figure displays horizon number 22 of the total 36 horizons representing the 3D cave model.*

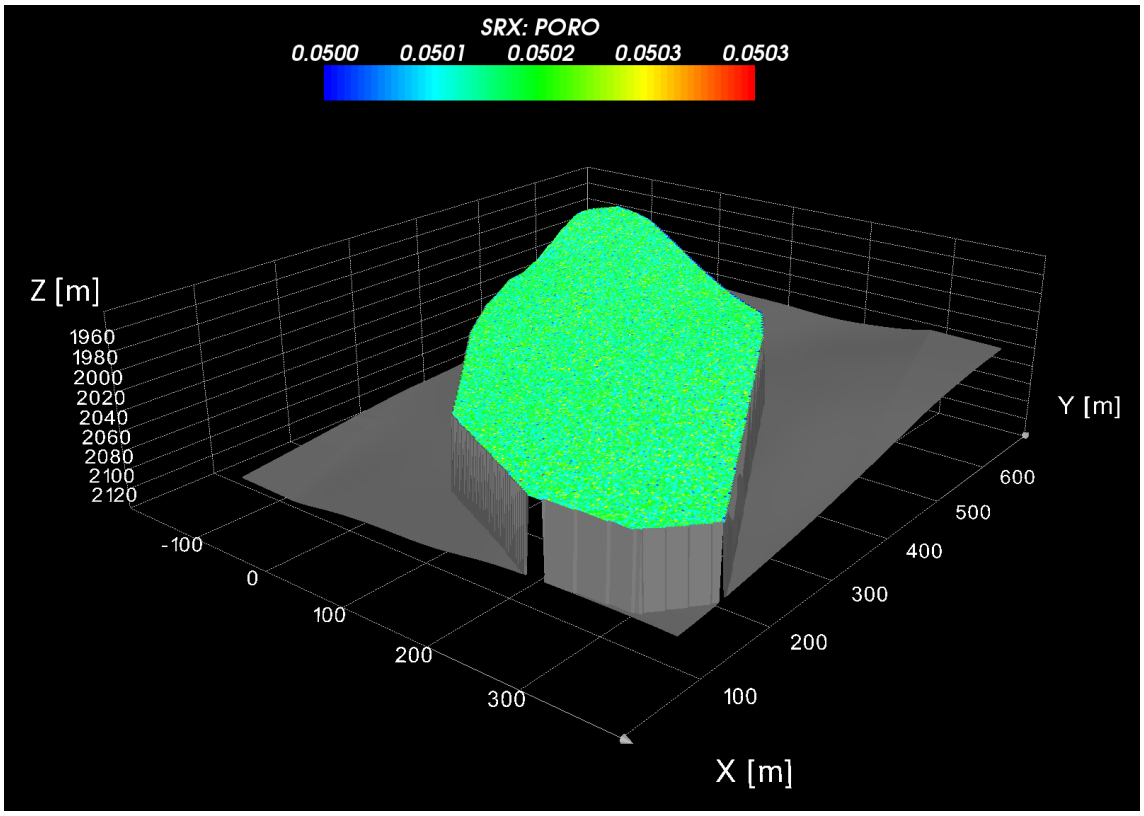

Figure 5.2-2: *Horizon number 2, where no collapsed cave features are present, displays the range of porosity of the fracture network populated in the 3D cave model. These porosities are low (around 5%) and are distributed throughout the entire 3D model.*

Rock physics modelling

The physical properties of the calcite mineral used in the rock physics calculations for the Setergrotta cave are 76.8 GPa, 32.0 GPa and 2.71 g/cm^3 representing the bulk and shear moduli, and the density, respectively. Two rock physics scenarios will be considered, where the only difference between these scenarios will be the aspect ratio outside the cave passages.

The first case consists of two different aspect ratios, where the aspect ratio inside the cave passages will be 0.1, and the aspect ratio outside the cave passages will be 0.01, which describes a more fracture dominated setting. For the second case, an aspect ratio of 0.1 will be considered for the whole 3D model, both inside and outside the cave passages. The two rock physics cases are displayed in table 5.2-6 and 5.2-7, while the resulting plot of the bulk and shear moduli, and the densities, are displayed in figure 5.2-3, 5.2-4 and 5.2-5. Other parameters included in the rock physics modelling of the Setergrotta cave, are equal to the parameters presented in Avseth et al. (2014) (and also mentioned at the beginning of the rock physics section for the Franklin Mountains model 5.1).

Table 5.2-6: *Rock physics models of the scenario with two different aspect ratios. The 3D model is considered to only consist of limestone and brine is considered to fill the pore space throughout the whole model.*

	Lithology	**Fluid saturation**	**Aspect ratio**
Inside cave passage	Limestone	100% Brine	0.1
Outside cave passage	Limestone	100% Brine	0.01

Table 5.2-7: *The second case only considers one pore type, both outside and within the cave passages in the 3D model. The 3D model is considered to only consist of limestone and brine is considered to fill the pore space throughout the whole model.*

	Lithology	**Fluid saturation**	**Aspect ratio**
Inside cave passage	Limestone	100% Brine	0.1
Outside cave passage	Limestone	100% Brine	0.1

Figure 5.2-6 displays the result of the rock physics modelling, and how the bulk and shear moduli are distributed within the 3D model for the two scenarios. The derived P-wave velocities representing these two cases are illustrated in figure 5.2-7a and b, including the computed reflectivity in figure 5.2-7c and d. The case where the medium outside the cave passages consists of low aspect ratio pores (figure 5.2-6a and c, and 5.2-7 a and c), will be further investigated under the seismic modelling

segment. The reason for choosing that specific scenario is because a medium dominated by fractures, are (as mentioned earlier in this thesis) quite common nearby a collapsed and deeply buried paleocave system.

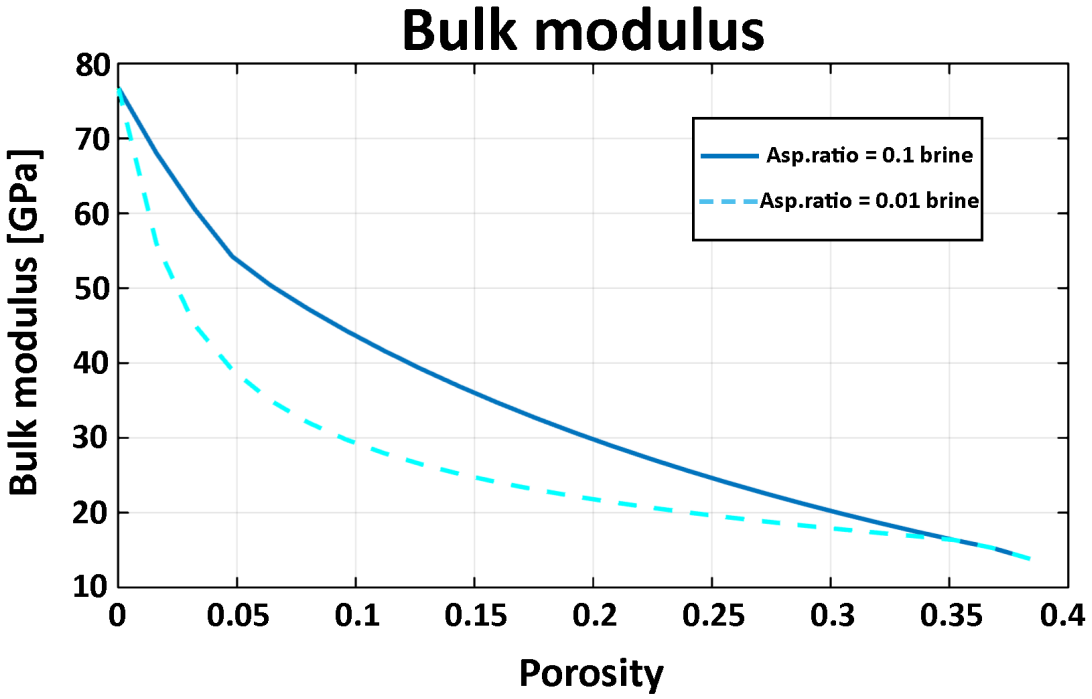

Figure 5.2-3: *The figure shows a plot of the bulk modulus versus porosity for two different pore geometries. Both lines in the plot represent the same mineral composition (calcite). The solid line represents an aspect ratio of 0.1, while the dashed line represents an aspect ratio of 0.01.*

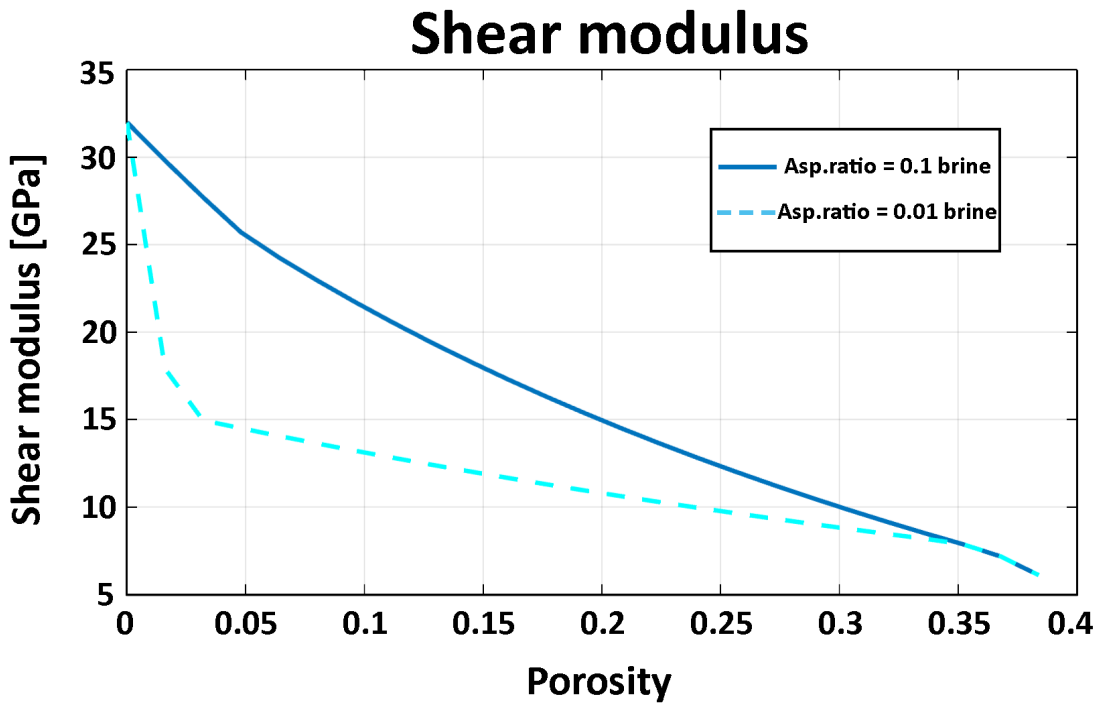

Figure 5.2-4: *The shear modulus is plotted against the porosity. The different lines represent similar trends as the bulk versus porosity plot, except for the 0.01 aspect ratio case, where the shear modulus decreases much faster with increasing porosity than the bulk modulus case.*

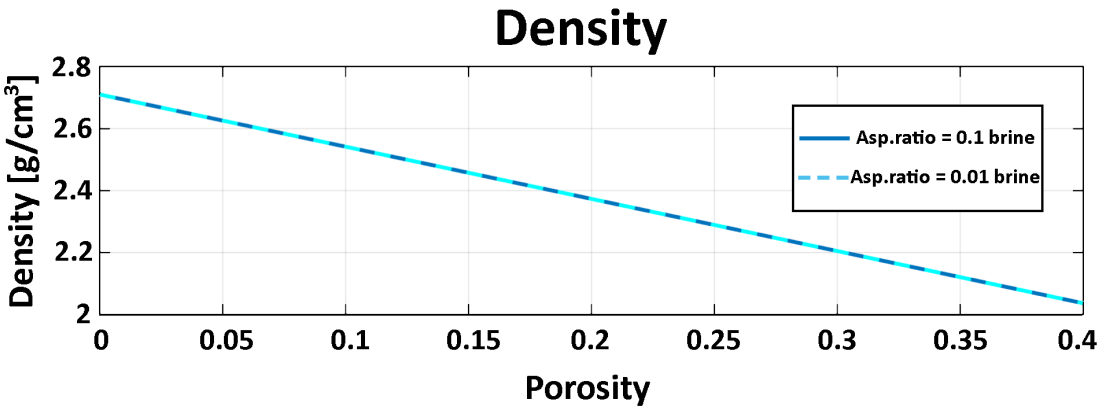

Figure 5.2-5: *The figure illustrates how the density is affected by the porosity. Since the density does not take pore geometry into account, the densities of the two different cases of aspect ratio are the same.*

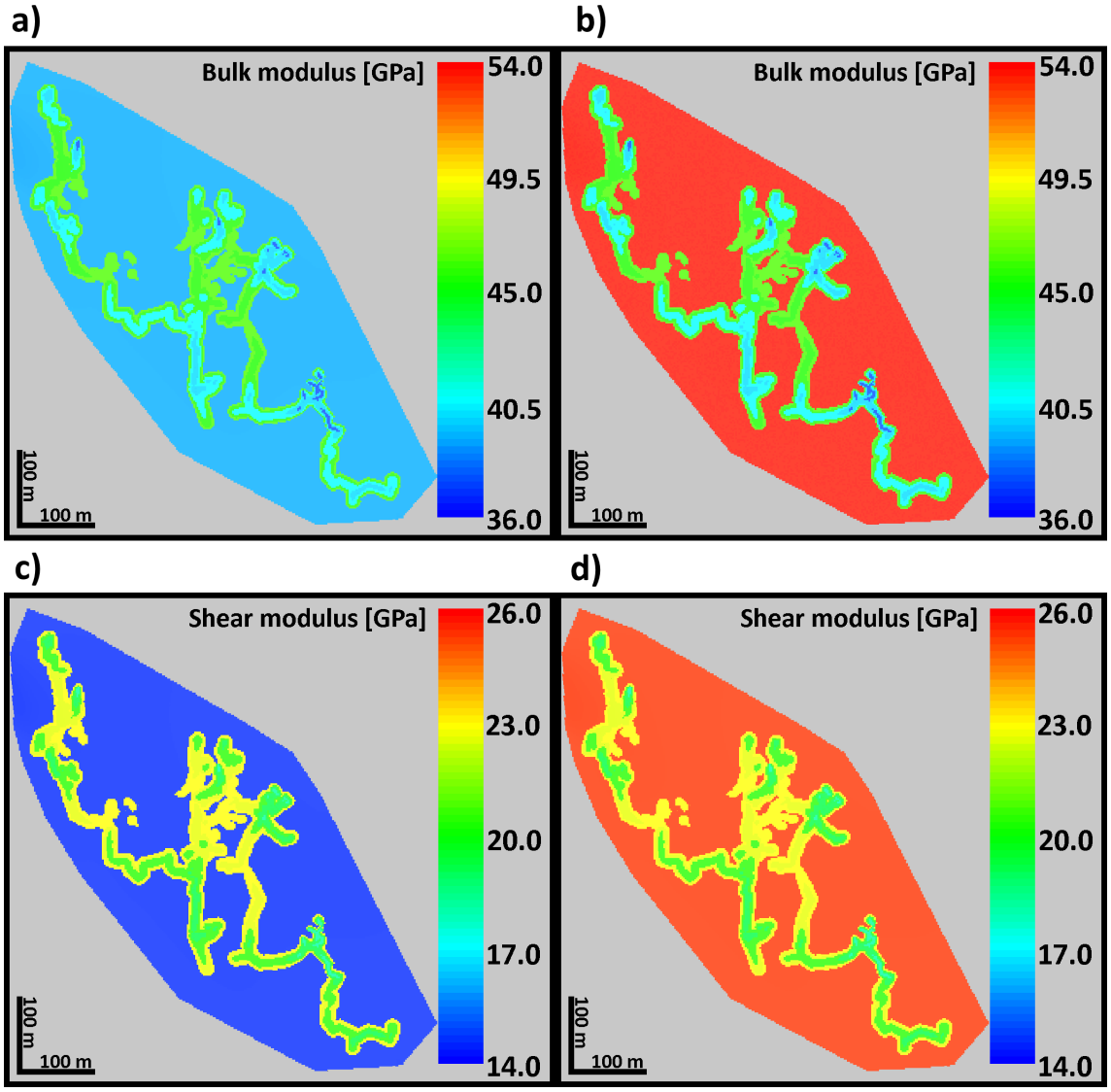

Figure 5.2-6: *The figures display the bulk (a and b) and shear (c and d) moduli of the two different scenarios mentioned earlier. (a) and (c) represent the scenario where there are one type of pore geometry inside the cave (aspect ratio: 0.1) and a different pore geometry outside the cave (aspect ratio: 0.01). Figures (b) and (d) consider the case where the pore geometry is the same both inside and outside the cave (aspect ratio: 0.1).*

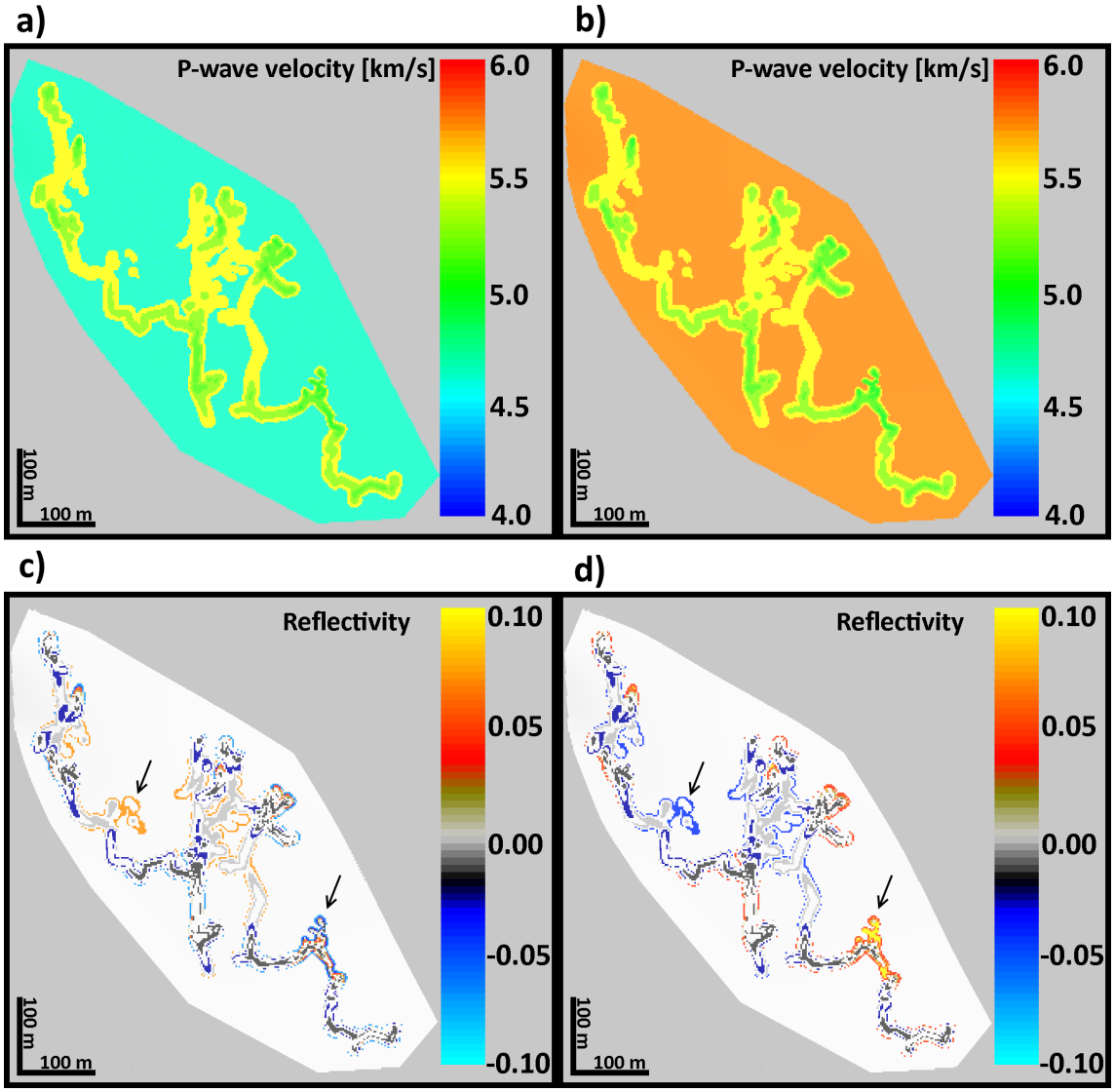

Figure 5.2-7: *The P-wave velocities seen in (a) and (b) are derived from the bulk and shear moduli (and the density) from figure 5.2-6. Figures (c) and (d) represent the reflectivity based on the P-wave velocities in (a) and (b). (a) and (c) represent two different pore geometries (one inside the cave and one outside), while (b) and (d) display only one type of pore geometry. In the reflectivity plots (c and d), the black arrows indicate areas where the most noticeable changes in the reflectivity (between the two different scenarios) are located.*

Seismic forward modelling

The elastic properties derived from the rock physics modelling of the Setergrotta cave model, where the cave interior and the surrounding medium consisted of two different pore geometries, are considered in the seismic forward modelling performed in this section. Figure 5.2-8 illustrates the P-wave velocity of this model, where the aspect ratio inside the cave is equal to 0.1, while the aspect ratio outside the cave is equal to 0.01.

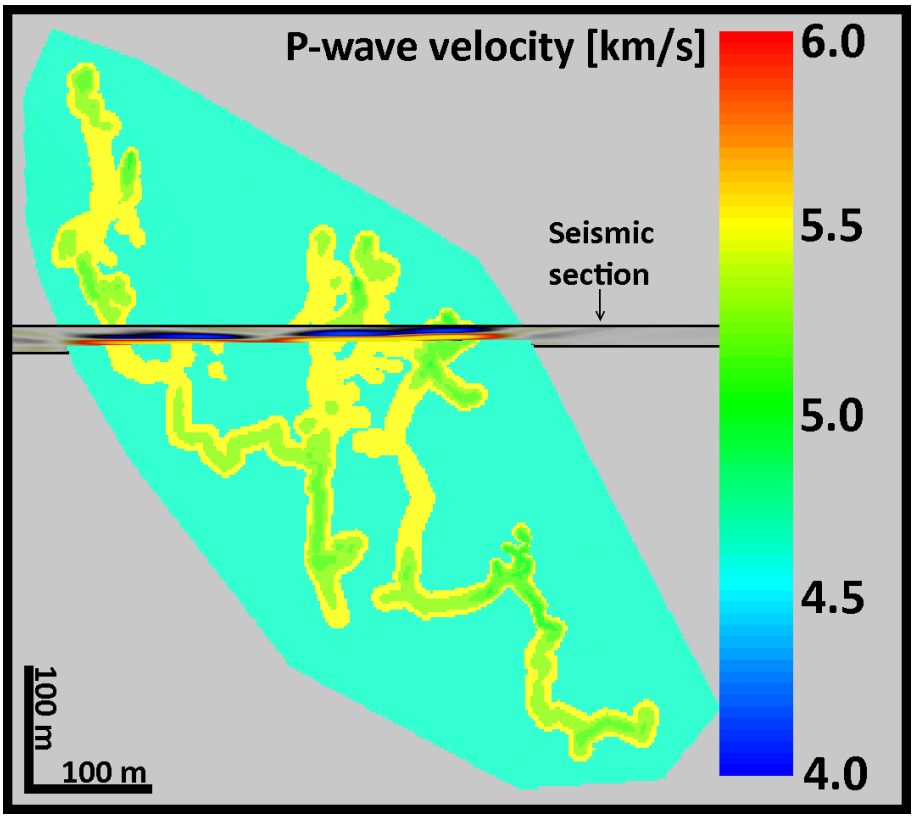

Figure 5.2-8: *The figure displays the P-wave velocity as seen from above (horizon 22) and the location of a vertical section crossing the horizontal view just above the center of the image.*

The input parameters and the corresponding values used in the seismic forward modelling are displayed in table 5.2-8. Since the Setergrotta cave model is a 3D model with several horizons describing it, I chose one horizontal section and one vertical section which will be further investigated. The horizontal section is located at a depth of 2048 m, in the vicinity of the horizon displayed in figure 5.2-8, while the position of the vertical section is illustrated in figure 5.2-8 as a slice window cutting through the 3D model.

Table 5.2-8: *The input parameters used in the seismic forward modelling of the Setergrotta cave model.*

Maximum reflector dip	45°
Average velocity in target model	5 km/s
Incident angle	0°
Wavelet	Ricker: 30 Hz
Reflection mode	P-P

Figure 5.2-9 and 5.2-10 show the reflectivity and corresponding synthetic seismic in the horizontal section and vertical section, respectively. The synthetic seismic does not capture any distinguishable features representing the cave geometry. The most noticeable from the synthetic seismic in the horizontal section is the correlation between three high negative amplitudes in the seismic with the high negative reflectivity. In the vertical section, the seismic could be interpreted as representing two different units lying next to each other, based on the two separately seismic events, though the reflectivity model reveals that there exist more than two cave units.

The figures displaying the vertical sections have been vertically exaggerated, and the PSF attached in these figures are therefore vertically stretched. These PSF's do not correlate with the same distance scale as the seismic image, because that would have caused the PSF-display to cover some of the seismic events. The reason for the vertical exaggeration is to better display the seismic, which makes it easier for interpretation. The exaggeration does not apply for the figures representing the horizontal section, where the PSF's attached (unlike in the vertical sections) correlate with the scale of the seismic image. Figures 5.2-11 and 5.2-11 show a superposition plot between the reflectivity and the synthetic seismic image in different locations in the 3D model. All of the figures represent calibrated seismic, except the superposition plots in figure 5.2-11 and 5.2-11.

As a result from the 3D convolution with a relatively large PSF (due to high velocity and low frequency, in addition to the selected illumination pattern), interferences with the surrounding structures will occur, both laterally and vertically. The lateral and vertical seismic smearing-effect is displayed in figure 5.2-11, where seismic signals are registered in areas without reflectivity. This is due to underlying or overlying strong seismic events, where these may interfere either constructively or destructively with the surrounding medium. Figure 5.2-11 displays three different horizontal sections, where (a) represents a section at 2048 m, (b) at 2038 m and (c) at 2028 m. Moving upwards from (a) to (c) in figure 5.2-11, one can see that some of the seismic amplitudes originating from the reflectivity in (a) are displayed 20 m above in (c). This is also illustrated in 5.2-12, where the section is shifted horizontally.

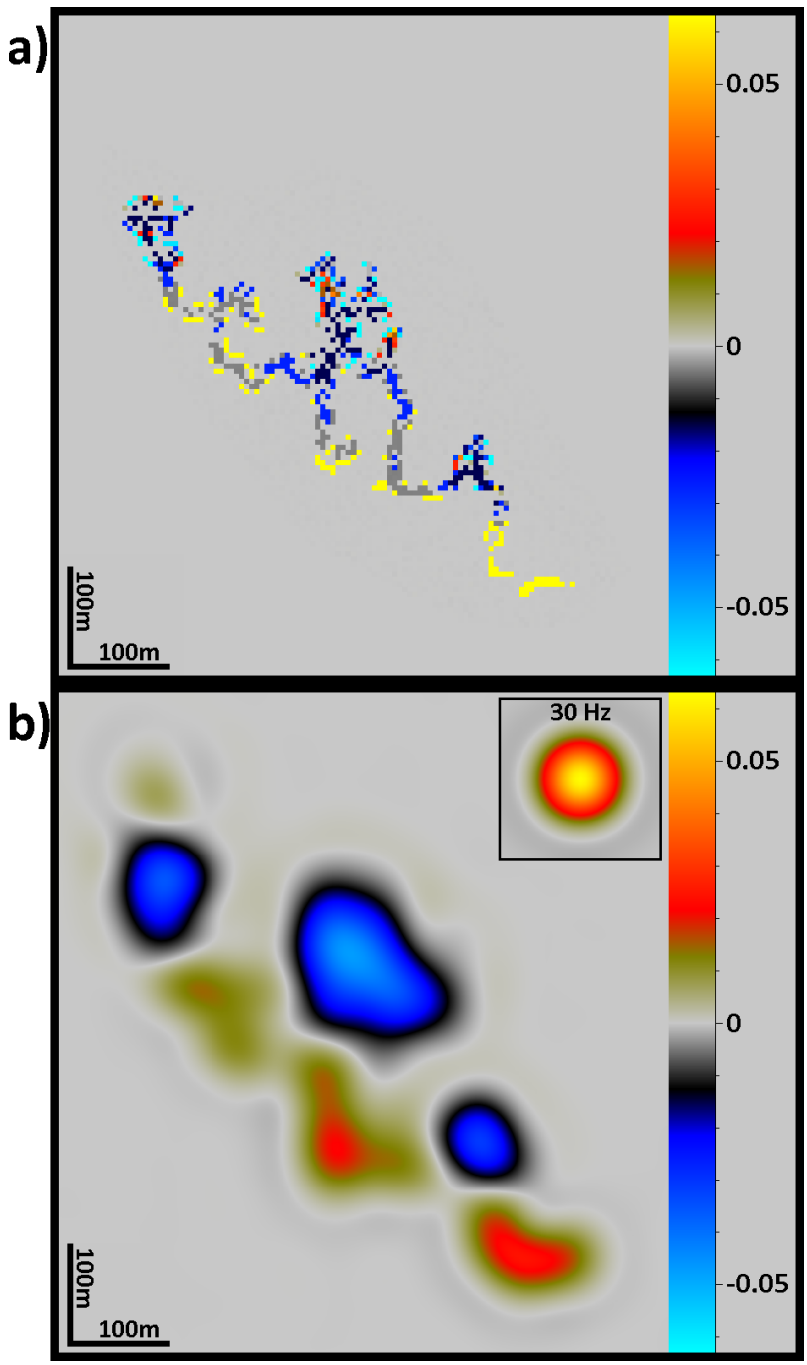

Figure 5.2-9: *The figure displays the reflectivity in a) and the corresponding synthetic seismic in b), where both are located in the same horizontal plane at depth 2048 m (seen from above). The 30 Hz PSF that is used in the 3D convolution with the reflectivity is displayed at the top right of b).*

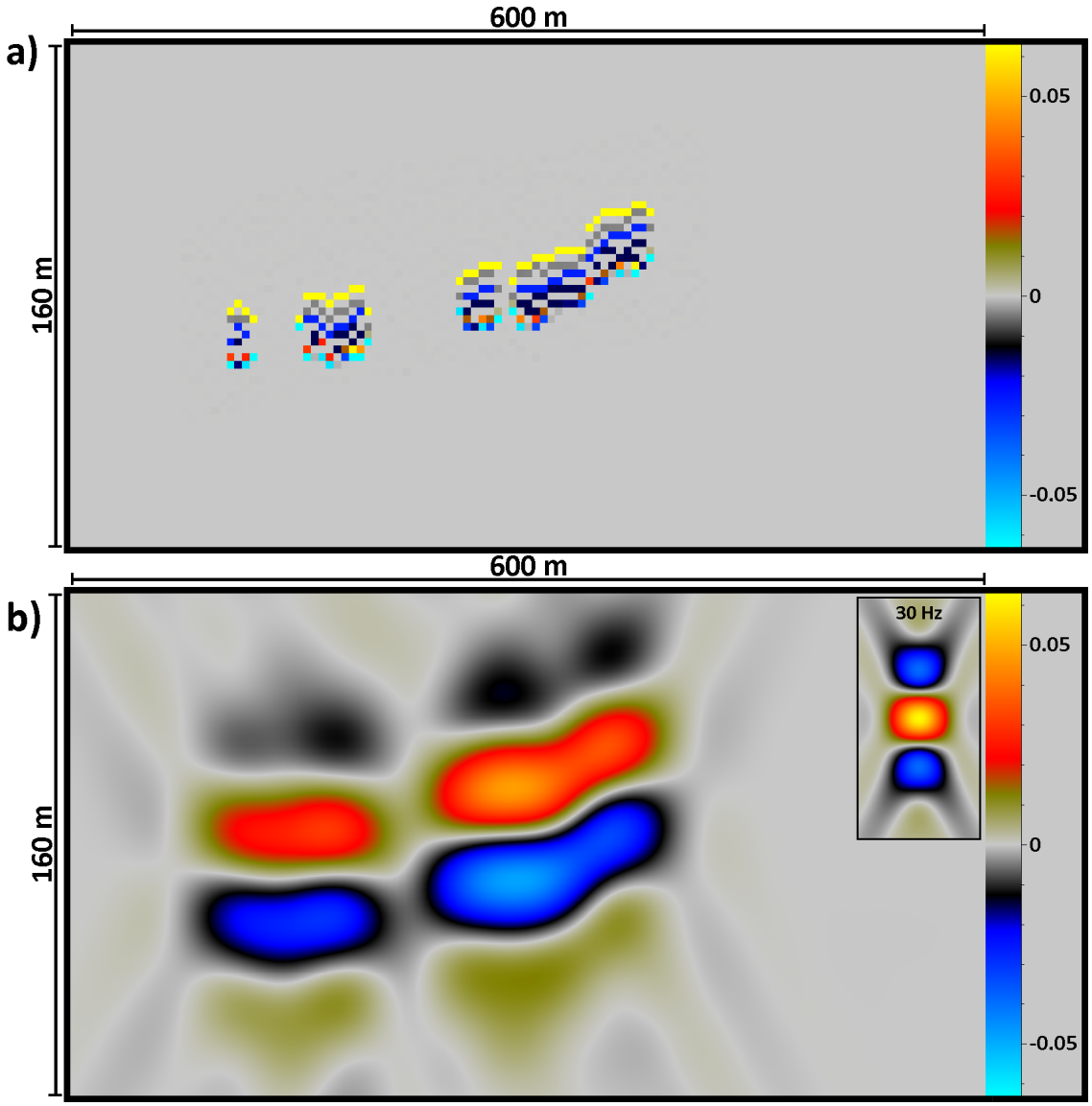

Figure 5.2-10: *The figure displays the reflectivity in a) and the corresponding synthetic seismic in b) from the vertical section (position displayed in figure 5.2-8). The 30 Hz PSF that is used in the 3D convolution with the reflectivity is displayed at the top right of b). The PSF is stretched vertically due to a vertical exaggeration of the synthetic seismic image..*

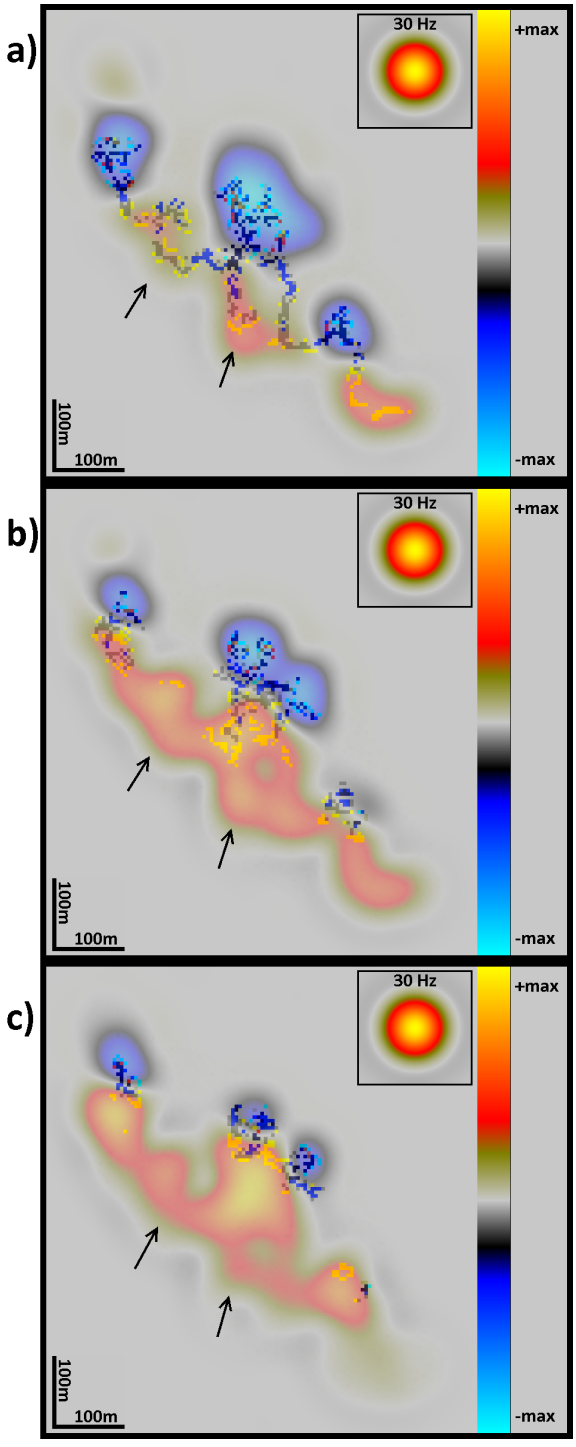

Figure 5.2-11: *Superposition plots of the reflectivity model and the corresponding synthetic seismic in the horizontal plane. (a) Displays a dual plot at a depth of 2048 m, (b) at 2038 m depth, and (c) at 2028 m depth. The black arrows indicate areas where seismic energy is recorded at zones with no reflectivity (b and c), which originate from the reflectivity in a section below (a).*

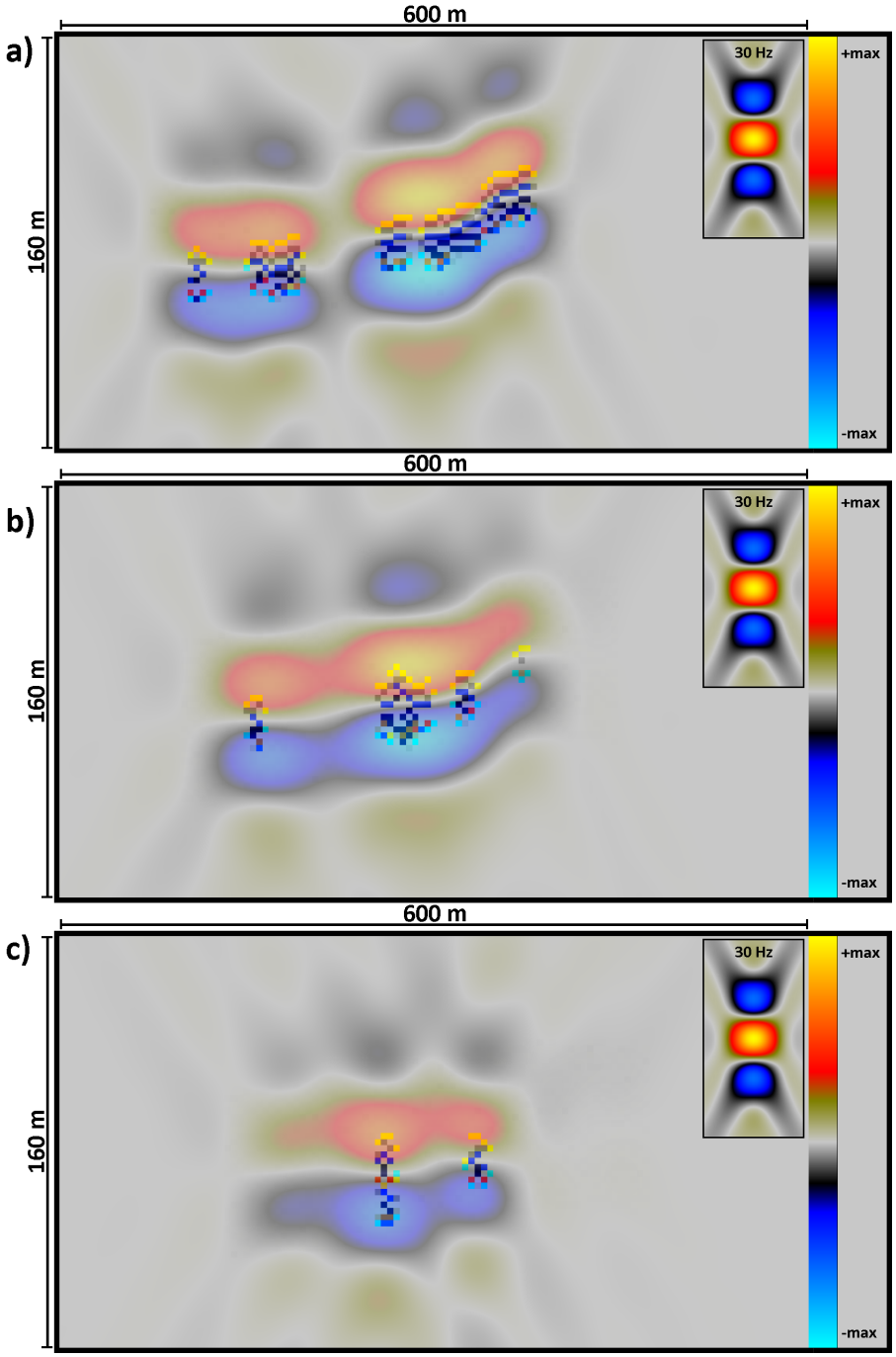

Figure 5.2-12: *Figures a-b display superposition plots in three different vertical sections, showing the effect of vertical and lateral resolution of the 3D synthetic seismic.*

High resolution case

To compare the seismic seen above with a higher resolution case, a 60 Hz PSF is now considered. All the other inputs are the same as shown in table 5.2-8. Figure 5.2-13 and 5.2-14 show that far more details can be distinguished from the 60 Hz PSF case, as expected. The structure of the paleocave and of some of the passages can be better interpreted (horizontal section). Where we, for the low-resolution case, barely could distinguish two different cave-units in figure 5.2-14a, we can can almost identify four different cave-units in the high-resolution case. Also, there are fewer interferences from the surrounding medium, which in the low-resolution case caused seismic energy to be projected further away from its "source".

3D convolution versus 1D convolution

A comparison between the 3D convolution versus 1D convolution was done to illustrate the benefits with a 3D convolution approach in terms of generating more realistic synthetic seismich. For the comparison, the same input parameters were used (besides the max reflector dip). From figure 5.2-15 and 5.2-16, the differences are noticeable. The 1D approach does not account at all for lateral resolution which causes the 1D convolution case to almost match the reflectivity model, except for the vertical resolution effect, and the dominating "smeared out" features in the 3D convolution case are not present in the 1D convolution case. Figure 5.2-16 displays very well how the the different seismic events almost connect with each other in figure 5.2-16a due to the lateral effect of the PSF, while these smooth lateral variations are non-existing for the 1D convolution case, where the lateral seismic events change abruptly (figure 5.2-16b). This do not represent realistic seismic images.

Also, the figures display synthetic seismic with a "bilinear" resampling option, introducing a fake cosmetic smoothing (adding a small lateral smearing), which is more prominent for the 1D convolution case. A pixelated resampling would therefore show a even more abrupt lateral change for the 1D convolution approach. The bilinear resampling was chosen due to a more "elegant" synthetic seismic display for the 3D convolution case, and therefore also chosen for the 1D case to get a proper comparison.

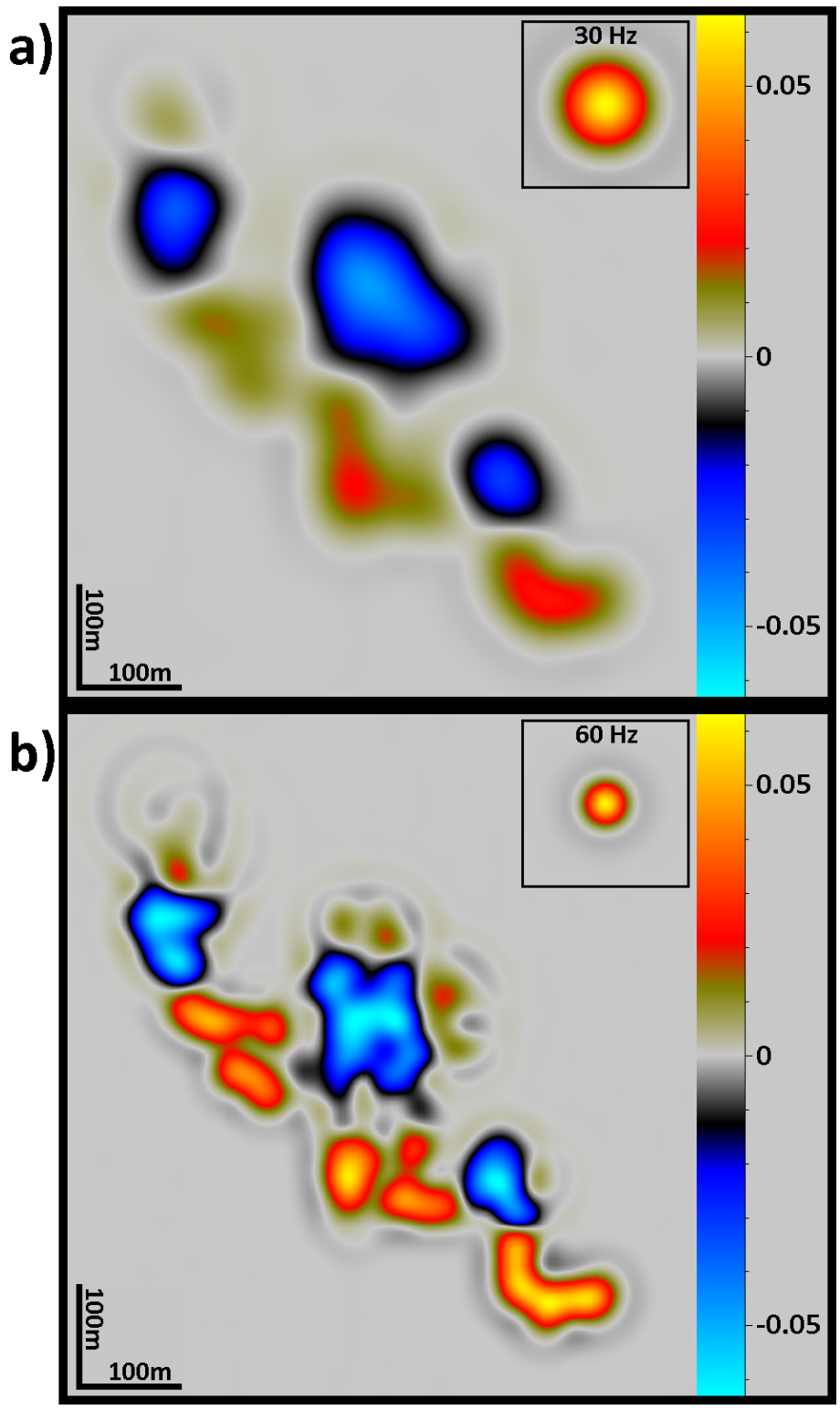

Figure 5.2-13: *Figure (a) represents the low resolution case with a 30 Hz PSF, while (b) represents a high resolution case with a 60 Hz PSF. Both are located in the horizontal plane.*

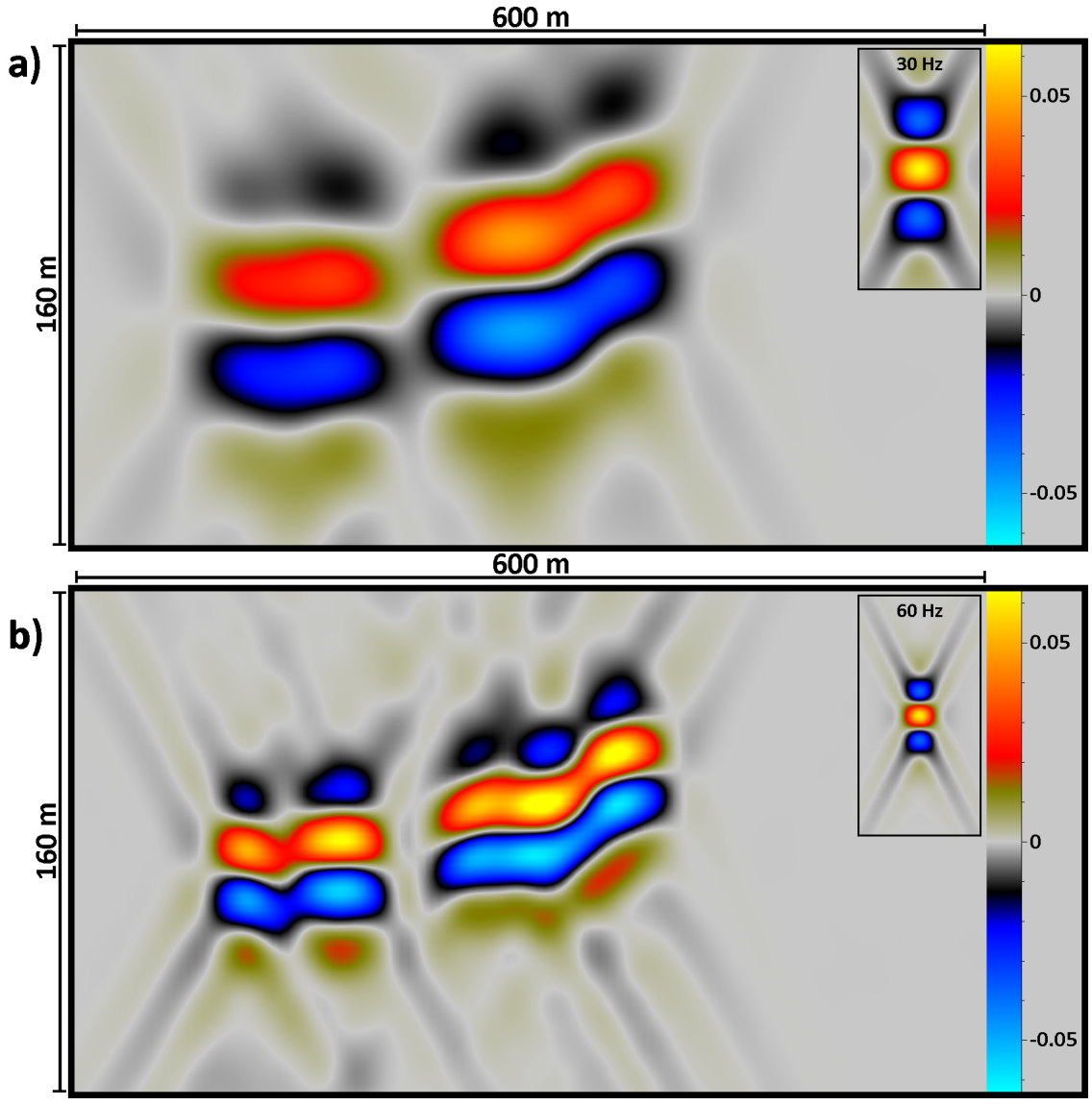

Figure 5.2-14: *Figure (a) represents the low resolution case with a 30 Hz PSF, while (b) represents a high resolution case with a 60 Hz PSF. Both are located in the vertical section displayed in figure 5.2-8.*

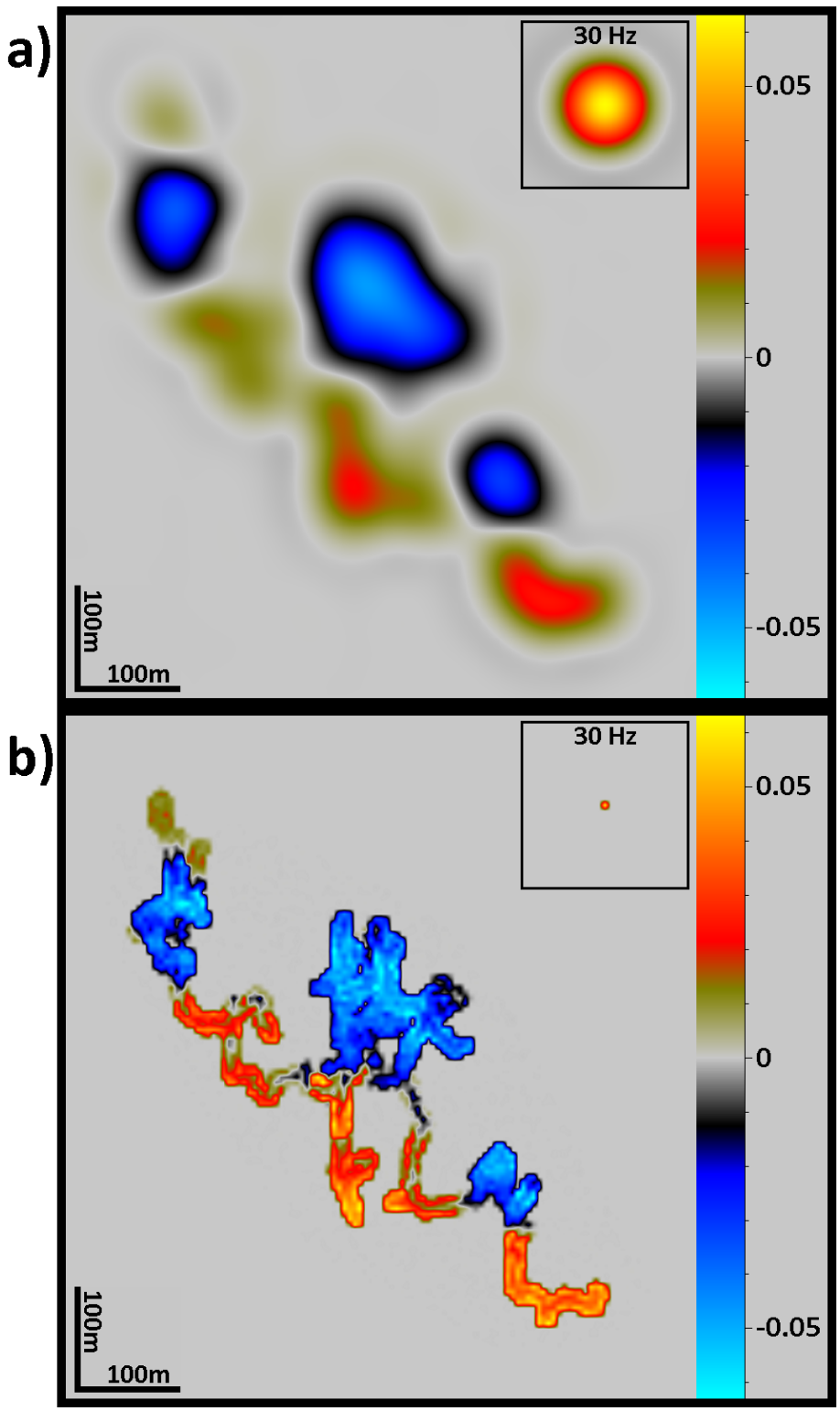

Figure 5.2-15: *The figures are displayed in the horizontal plane, where (a) represents synthetic seismic based on the 3D convolution approach, while b) represents synthetic seismic derived from a 1D convolution approach. Notice the difference between the 3D PSF in (a) and the 1D PSF in (b).*

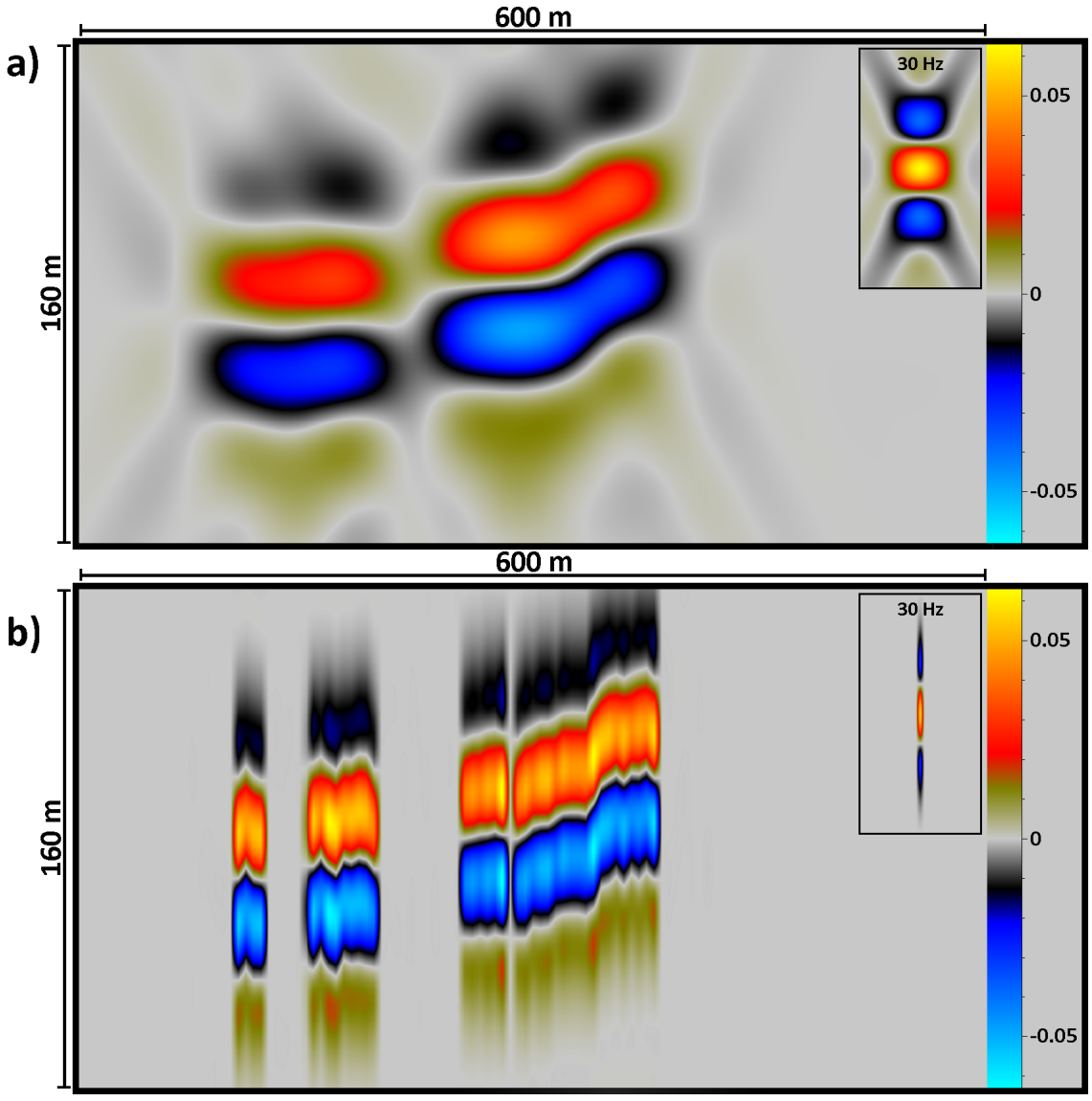

Figure 5.2-16: *(a) represents the 3D convolution based synthetic seismic, while (b) represents the 1D convolution based synthetic seismic. Both (a) and (b) are displayed in the vertical section displayed in figure 5.2-8.*

Chapter 6

Discussion

The aim of this thesis has been to provide a workflow related to modelling for seismic characterization of paleokarst reservoirs. The results presented in chapter 5 include three main steps for each input model. The first step concerns the geomodels described by porosity, fluid saturation and various mineral constituents, the second step involves a rock physics modelling adapted to the carbonate and paleokarst heterogeneities, and the last step consists of performing an effective and sufficient seismic forward modelling. I have considered a set of different scenarios in the rock physics and seismic modelling parts, though there could have been done much more research and more specific case studies, but due to time limitation this study has been constrained to focus on the specific cases presented in chapter 5. Potentially interesting considerations and applications related to this study will be further addressed later, after the conclusion.

6.1 The 2D and 3D input models

Considering the two different models presented in the results chapter, both were insightful based on their main purpose. They were generated using two completely different generation and import strategies, where one was derived form an image and the other one imported directly from Eclipse as a reservoir model, which shows the flexibility of the input.

The 2D palocave model derived from a large outcrop in the Franklin Mountains gave a more detailed information about the porosity and the geological composites of the paleocave and the surrounding strata, and as such could provide realistic properties representing true paleocave features. This outcrop is highly known and referred to in the world of paleokarst, hence the choice of using it for modelling. Also, no one

has, to the best of my knowledge, been modelling the outcrop seismically before.

The 3D model of the Setergrotta cave did not provide a detailed description of the composites in the paleocave passages since it was based on a collapse simulation and porosities were estimated throughout the model based on typical trends in collapsed paleocaves. However, the 3D model of the Setergrotta cave provided an exceptional opportunity to analyse the seismic response of a real cave geometry, while including reservoir-like effects via both the cave structure and a surrounding fracture network.

Generating the Franklin Mountains 2D model was one of the most time-consuming processes in terms of adding suitable petrophysical properties for the different model components. The import of the 2D model to the SeisRoX software did also cause small complications, where the 2D model had sharp contrasts between the different layers before the import, but was affected by an issue causing the SeisRoX software to possibly interpolate between the original grd points when extracting the properties for the modelling in the considered target, which led to a smooth transition between the different layers. This issue could be a result of a mismatch between the import grid of the target model in SeisRoX and the grid representing the original image.

The issue did cause a minor alteration to the computed reflectivity model, which is displayed in figure 6.1-1. This will probably have a limited effect on the corresponding synthetic seismic, in terms of a slightly weaker reflectivity, though it will not be a critical issue. The Setergrotta cave did not cause similar problems, and did on the contrary represent a robust input model, directly imported as an Eclipse reservoir file.

An issue related to the software was the reflectivity of very steep features. As seen in figure 6.1-2, the reflectivity of these steep features resulted in a non-continuous reflectivity, where a steep near vertical line was presented as scattered points. This is due to an aliasing effect that occurs as the modelling software only extracts the elastic properties along vertical lines in that type of gridded model when calculating the reflectivity. That being said, pure vertical structures would not be imaged in most actual seismics. One way of dealing with this issue could be to adjust the steep features in the model to be represented with a more curvy appearance, instead of straight lines, or start directly from the impedance models, but that would require a phase-shift correction to come back to a zero-phase signal (Lecomte pers.comm.).

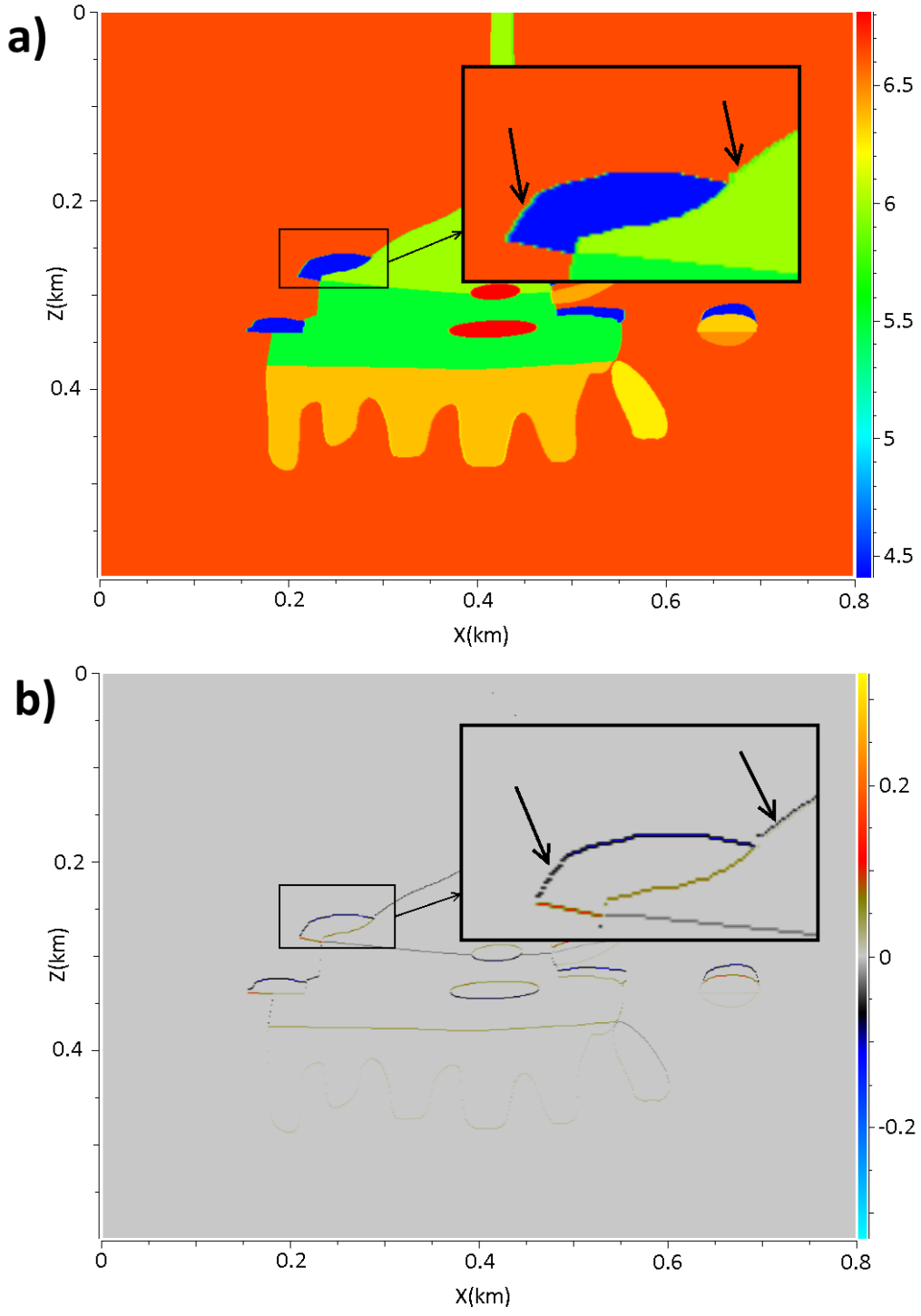

Figure 6.1-1: *The figures illustrate that the smooth transitions, made from interpolated properties at the layer boundaries, have an effect on the computed reflectivity. (a) displays the P-wave velocity of the 2D model, while (b) represent the corresponding reflectivity model. The black arrows indicate areas where a smooth transition occur. These artefacts only occur in some of the layer boundaries in the 2D model.*

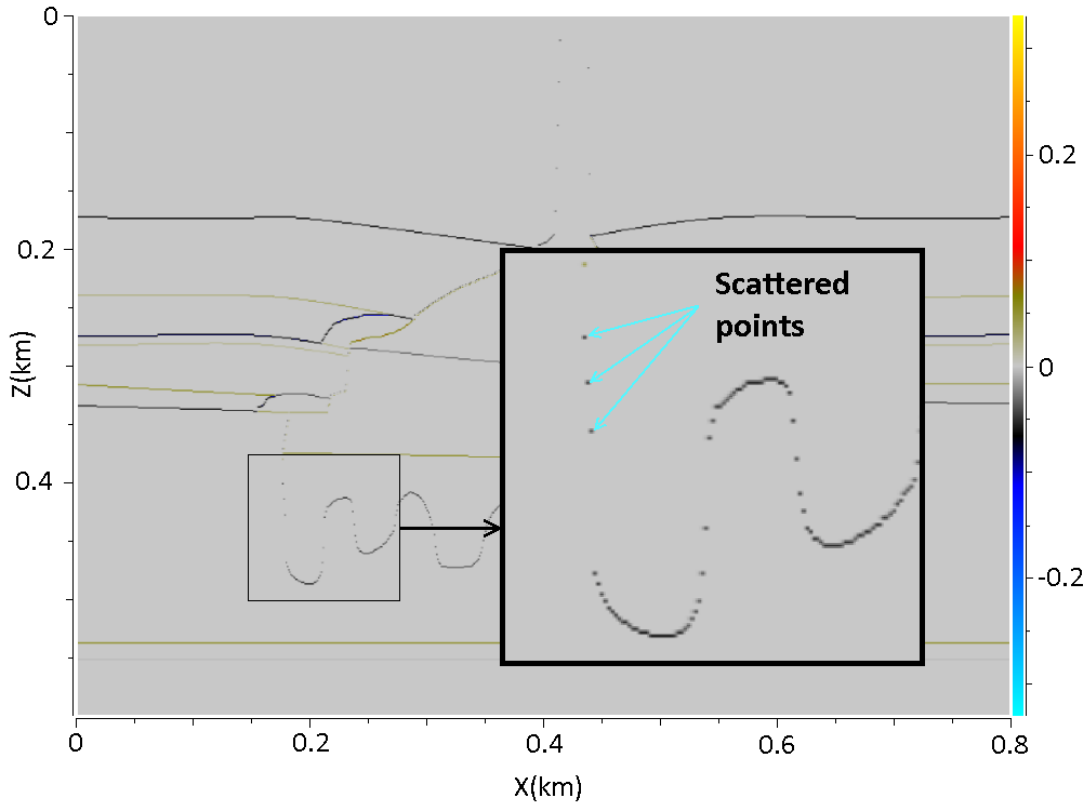

Figure 6.1-2: *A (near) vertical component will be displayed as points in the reflectivity model (this figure represents the Franklin Mountains paleocaves). The light blue arrows indicate scattered points where a steep, near vertical continuous line should have been displayed instead. These scattered points can also be seen on top of the GMS paleocave, where the points represent the vertical breccia pipe.*

6.2 Rock physics modelling

Xu and Payne (2009) stated that the pore geometry could influence the P-wave velocity by up to 40%, and considering the results in this study, that seems like a reasonable statement for the most extreme cases. The estimated P-wave velocities for the surrounding medium of the Setergrotta cave (figure 5.2-7 a) and b)), are equal to 4.69 km/s (aspect ratio = 0.01) and 5.78 km/s (aspect ratio = 0.1) which gives a difference of ca. 19%. For the Franklin Mountains case, a difference of ca. 26% in P-wave velocity has been registered in the 2D paleocave model, where the aspect ratio is the only parameter that has been changed (aspect ratio of 1.0 versus 0.01).

The pore geometry has been the most influential factor for determine the elastic properties representing a saturated reservoir. The hybrid rock physics model, called the Kite-model, used in this study has proved to be a valuable approach which deals with complex carbonate conditions, where the low-porosity zone controlled by the DEM method emphasizes the importance of the pore geometry, while the high-porosity zone, determined by the CCT, takes the relatively high velocity occurrences caused by cementation into account.

A drawback concerning the rock physics part in this study has been the import of the rock physics model into SeisRoX, where the fluid effects does not seem to be taken into account. Whether this is due to the imported rock physics file from the external program or if it is the SeisRoX software itself that does not manage to account for different fluids in that type of gridded model is temporarily unknown. The reason for questioning this, is that the bulk modulus of the oil saturated paleocaves in the Franklin Mountains 2D model does not seem to correlate with the output bulk modulus plot calculated by the rock physics modelling script (figure 6.2-1).

Oil saturation was included in the exported rock physics file representing the paleocave components, and further added to the corresponding blocks of the 2D model in SeisRoX, but the output bulk modulus does however display a brine saturated target. For the future, the link between an external rock physics modelling approach, such as the Kite-model, and the SeisRoX modelling software should be improved for a more efficient modelling workflow.

In the 3D Setergrotta model, one would probably expect a negative reflectivity when going from the medium surrounding the paleocave to the collapsed material occupying the paleocave passages, this due to an increase in porosity. This is true for the case where only one pore geometry is considered in the whole model, but when a pore geometry with a lower aspect ratio is introduced to the surrounding medium while the pore geometry inside the cave has a high aspect ratio, one may get a positive reflectivity between the surrounding medium and the cave composites.

Figure 5.2-7c and d illustrate this, where black arrows indicate areas with distinct changes in reflectivity. This will also affect the synthetic seismic.

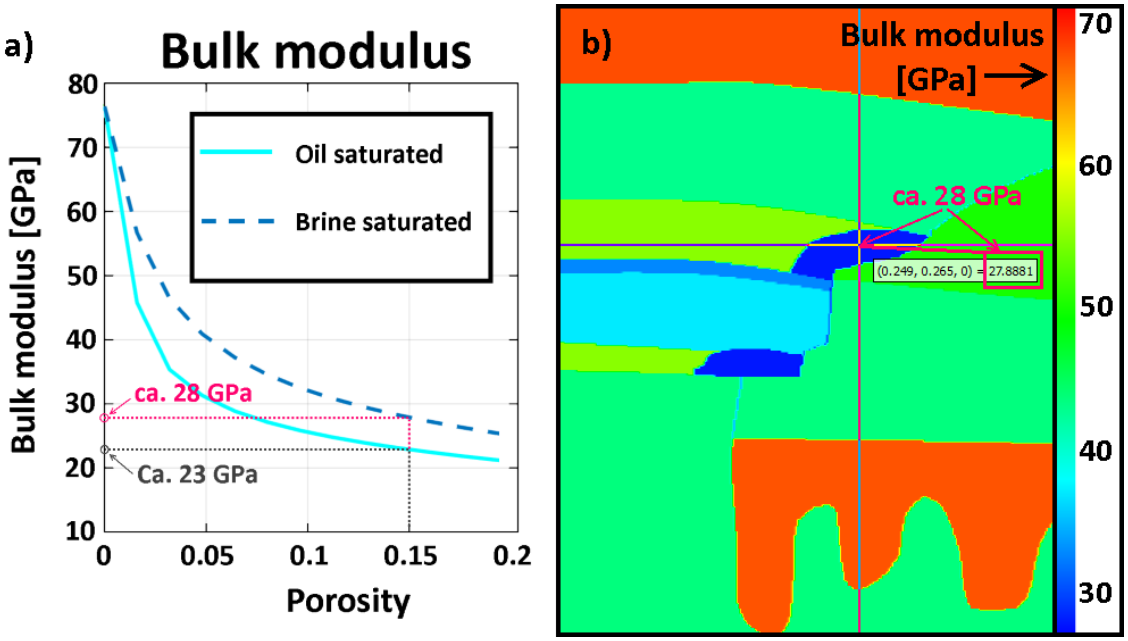

Figure 6.2-1: *The paleocave features in the Franklin Mountains 2D model case were saturated with oil, including the crackle breccia which has a porosity of 15%. Figure (a) displays the bulk modulus versus porosity computed in the ENTER program (rock physics modelling script). Figure (b) displays the bulk modulus computed in the SeisRoX software based on the added rock physics model provided from the ENTER program. The Bulk modulus (displayed in SeisRoX) does not correlate with the bulk modulus graph for a oil saturated target, computed by ENTER. The two graphs in figure (a) have the same input values except for fluid saturation, where the blue dashed line represents brine saturation, and the blue solid line represents oil saturation. The bulk properties for 15% porosity are displayed by the pink and grey dashed squares representing brine and oil saturation, respectively.*

6.3 Seismic forward modelling

Due to the high seismic velocities inherent in the carbonate minerals, the resolution of the seismic representing carbonate reservoirs is poor. Heterogeneities in carbonate reservoirs represented by fractures, fluids, more scattering, etc., cause a high loss of elastic energy. This will effects high frequencies more than the low frequencies. Therefore, a combination of seismic attenuation and high velocity will reduce resolution, hence lower frequencies are chosen for this type of reservoirs. One can argue that a higher frequency than the 30 Hz used in this study may be possible in shallow subsurface scenarios, but by choosing the 30 Hz frequency case, one can also consider these results as deep-lying carbonate paleokarst reservoirs at similar depths as described in Zeng et al. (2011b).

By comparing my results with previous related works (described in section 4.7), one can find some similarities. In Xu et al. (2016), the seismic response of cave features with various shapes and sizes were investigated in a physical (tank) modelling experiment. For instance, the seismic response of a spherical shaped conduit (diameter 60m) they presented can be compared with the synthetic seismic response of the spherical feature (phreatic tube) displayed in the 2D model of the Franklin Mountains paleocaves, where the seismic characteristics are very similar, though the feature in the Franklin Mountains case includes several component with different seismic properties and will therefore give a different seismic response than the feature presented in Xu et al. (2016). A reproduction of the experiment described in Xu et al. (2016), but by using the 2(3)D convolution approach, could be a possibility for a future study and a possible validation of the 2(3)D convolution method, though one could question the applicability of the material used in the physical modelling described in Xu et al. (2016).

One of the synthetic seismic models presented in Janson and Fomel (2011) describes a 3D model of a modern cave system similar to the 3D model of the Setergrotta cave system presented in this study. However, a major difference between the 3D cave model presented in Janson and Fomel (2011) and the 3D model of the Setergrotta cave is the seismic velocities outside the cave passages contra the seismic velocities inside the collapsed cave, which in the Setergrotta case was due to the considered low aspect ratio describing the pore geometry outside the collapsed cave passages. Rock physics were not considered in Janson and Fomel (2011), where the velocities were based on outcrop-based samples and one sonic velocity well, and where the velocity distribution was decided by variograms. The layered velocity model surrounding the 3D cave model in Janson and Fomel (2011) provided also an interesting feature to the 3D model and presented a more realistic 3D representation of a paleokarst reservoir.

A fracture model (figure 5.2-2) was included in the Setergrotta cave model, but from

the synthetic seismic section displayed in chapter 5 (figure 5.2-9b), the seismic response of these porosity variations was not easily detected due to stronger response of the cave. Figure 6.3-1 displays a horizontal slice from the Setergrotta cave model, above the paleocave features, where the seismic response is more distinguishable, though vertical resolution smearing from underlying cave features affects the displayed seismic (the strongest seismic events in figure 6.3-1). This illustrates the impact of the vertical resolution. The porosity variations throughout the whole 3D model, in terms of fractures, are expected to influence the synthetic seismic of the paleocave features, though it may not be visible.

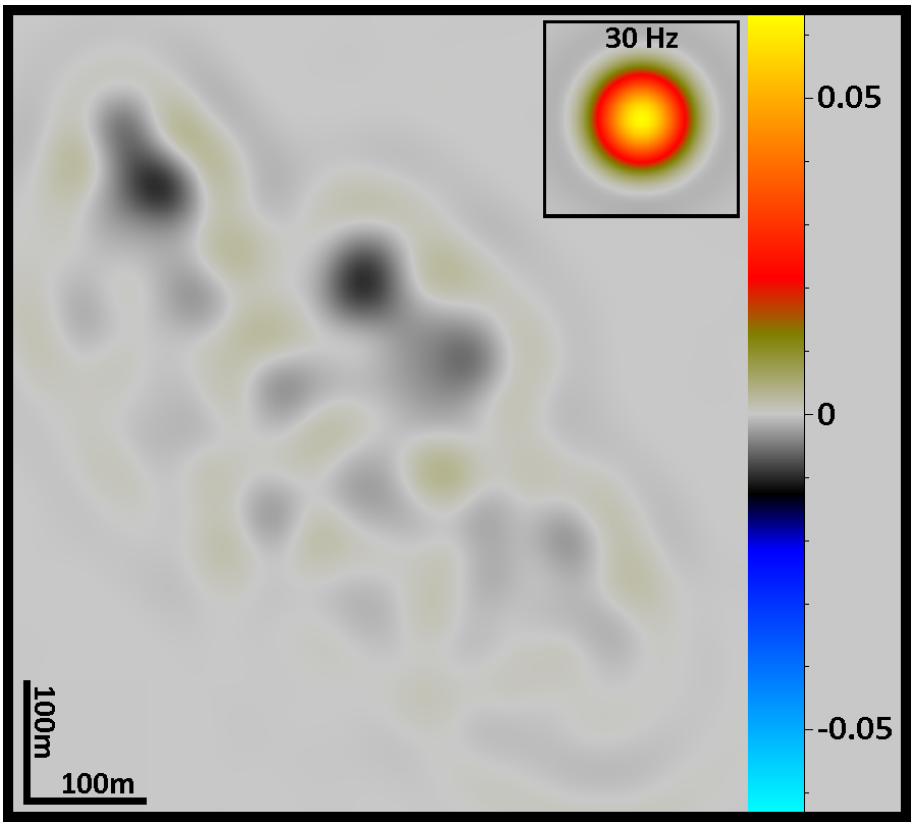

Figure 6.3-1: *The figure illustrates the synthetic seismic response of the fracture model included in the 3D model of the Setergrotta cave system. The amplitude scale is the same as the amplitude scales representing the synthetic seismic of the paleocave features in chapter 5. The two largest amplitudes (relatively strong black events) in this figure originate from a strong seismic event located below this section. This horizontal seismic section is located near the layer describing the porosity of the fracture model in figure 5.2-2.*

The comparison between the 3D convolution approach and the 1D convolution approach shows how significant the impact of not including lateral resolution effects

in the synthetic seismic is. By excluding the lateral resolution effects, an inaccurate representation of the seismic for a considered target is achieved.

Considering the efficiency in terms of computation time, the 2(3)D convolution approach used less than a minute computing the synthetic seismic (with a standard school computer: 64 GB installed RAM and 2.67 GHz and 2.66 GHz processors). This is considered quite efficient, though the 1D convolution method would use less time. It would still be worth considering the 2(3)D convolution over the 1D convolution due to the benefits that comes with a more realistic synthetic seismic image.

In this study, I have only considered normal incidence cases, but it is also important to consider the effects of amplitude versus offset (AVO) for paleokarst reservoirs. This is something that should be taken into account for similar studies in the future. When a non-zero incident angle is considered, wave conversions will occur (e.g. P-S), and the effect of S-wave velocities will play a role. To illustrate the effect of AVO, figure 6.3-2 displays how the reflectivity of a reflector may change due to an increasing incident angle. The properties describing the reflector is taken from the Setergrotta cave model. The P-P reflection coefficient decreases with ca. 37% from a normal incident angle (0°) to an incident angle of 30°.

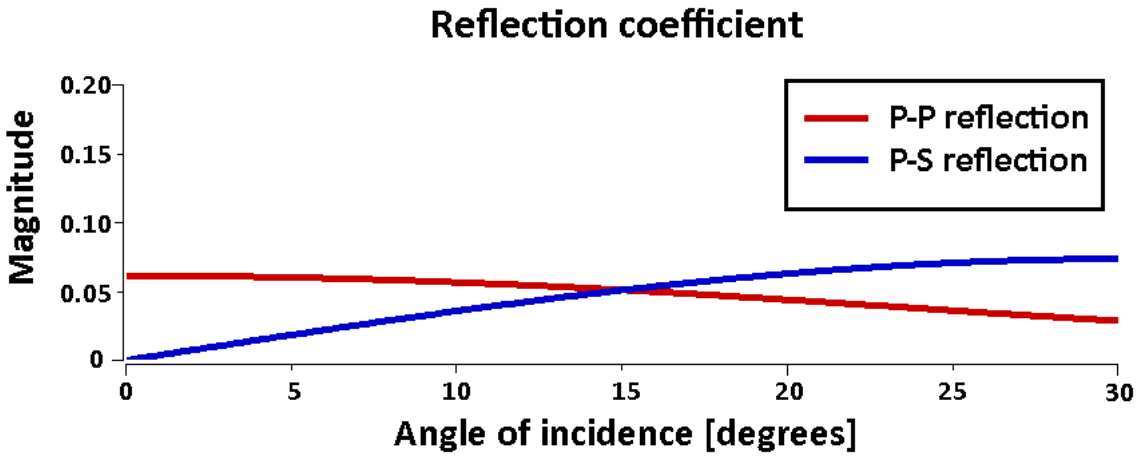

Figure 6.3-2: *The figure illustrates the effect of an increasing incident angle, and how this affects the reflection coefficient. The input properties describe the reflector on top of the 3D model representing the Setergrotta cave system. The red line represents P-wave reflection (P-P), while the blue line represents a mode conversion from a P-wave to a S-wave at the reflector. Incident angles up to 30° are considered.*

6.4 Reliability of the results

Several assumptions have been made throughout this study, mainly to be able look at different effects in a global modelling workflow, such as the various pore geometries and their distribution. The low aspect ratio representing the pore geometry of the background medium of the Setergrotta model was based on theories suggesting that a large fracture network is common in carbonates, especially surrounding collapsed paleocave features. This led to a quite low P-wave velocity of the surrounding medium (even lower than some parts of the collapsed paleocave interior). The reliability of that result will probably be questioned, though there has not been done much research including a similar rock physics modelling approach adapted to the heterogeneities found in carbonate paleokarst reservoirs.

The results are based on an isotropic medium, due to simplicity. This does not represent a true representation of the subsurface, and therefore the effect of anisotropy should be considered in future related work.

Other assumptions regarding the input paleocave models must also be considered when evaluating the reliability of the results. As mentioned earlier, the physical properties, such as the porosity in the Franklin Mountains 2D model, are based on approximations from interpretation of an outcrop and from an equivalent reservoir formation. The structure of the Franklin Mountains cave model is also highly simplified.

However, this study has provided a useful and preliminary overall workflow for modelling paleokarst reservoirs. If seismic data from a real paleokarst reservoir is provided in the future, one could compare with a model representing the same reservoir, and possibly test the validity of the presented workflow.

Chapter 7

Conclusion

The objective of the thesis was to provide a modelling workflow specifically aimed at seismic characterization of paleokarst reservoirs, which could then help establish guidelines for interpreters in terms of identifying paleokarst features in seismic images. This study has provided the following conclusions:

- The rock physics modelling results confirmed that the pore geometry is a key parameter in saturated carbonate paleokarst reservoirs. Pores with low aspect ratio, which represented fracture-like pores, gave a significantly lower seismic velocity compared to pores with high aspect ratio, which represented more spherical pores (moldic, intraparticle, vuggy pores). The Kite model provided therefore a valuable insight to the carbonate heterogeneities.

- The seismic forward modelling using a 2(3)D convolution method gave both fast modelling approach and the possibility to provide a realistic seismic representation of a very complex reservoir type.

- The input geo-models gave useful insight to various paleokarst features, though creating the 2D model of the paleocaves in the Franklin Mountains proved to be challenging in terms of determine relevant petrophysical properties for the different features in the model. The Setergrotta 3D model contributed with a robust model with realistic cave geometry and several petrophysical properties already included (from previous Msc thesis). Similar models representing paleokarst reservoirs will be valuable for future studies using the workflow presented in this thesis.

- By linking the rock physics modelling approach presented in this study with the 2(3)D convolution approach for seismic forward modelling, it has been demonstrated that the proposed modelling workflow aimed at complex carbonate reservoirs is a suitable approach for providing seismic characteristics

concerning paleokarst reservoirs.

7.1 Outlook

The presented workflow has been applied to two types of paleocave models in this study. The results demonstrated the potential of this type of modelling workflow, though improvements should by done to increase the efficiency and reliability in terms of linking the rock physics with the seismic modelling. Also, additional applications could be interesting to consider in terms of identifying seismic characteristics of paleokarst features. This section provides a few suggestions to future development and testing.

Authenticity of the input models

Improvements in terms of making the input models more realistic could be valuable and would provide a more reliable evaluation of the possible seismic characteristics. By including well log data from real paleokarst reservoirs (or an equivalent) in the input model, would give a more realistic representation of a background stratigraphy, similar to what was done in the 3D paleocave model in Janson and Fomel (2011). Rabbel et al. (2018) did include such a background stratigraphy based on well log data (density and sonic velocity) when modelling volcanic intrusions from outcrop data. The data was used to derive an acoustic impedance log, which was further used to generate a 1D layered model to represent that background stratigraphy.

Random noise (white and Gaussian distributed, then coloured according to seismic PSDM) could also be added to the 3D model, similar to what has been done in this thesis for the Franklin Mountain case (figure 5.1-16 and 5.1-17). The fracture network in the Setergrotta 3D model simulates similar random background noise, but here in the sense of surrounding structures of weak reflectivity, barely visible in comparison to the cave body itself.

A more complex cave network including several cave systems should be a possible scenario for future studies, where several cave conduits are distributed both in laterally and vertically directions over large distances. Loucks (1999) suggested a similar scenario, with fracture networks connecting the paleocave features, which implies a potentially quite extensive exploration target. As mentioned earlier, open paleocave conduits could potentially occur quite deep in the subsurface. In this study, only cases where the paleocaves are completely filled with collapse material have been considered. One could also study different scenarios regarding the paleocave

content varying from a completely filled conduit, from partially filled to an open conduit case.

Rock physics modelling parameter

The input rock physics properties in this study have been mainly based on the values presented in Avseth et al. (2014). Only one pore type has been considered for each rock physics model used in this thesis. A more complex pore shape distribution could be achieved by adding more than one pore shape within one rock physics model.

The fluid distribution within the paleocave models was very simplistic in this study, in lack of more information. A simple assumption that the paleocave features consisted of 100% fluid saturation with a homogeneous fluid mixing was considered. For future studies, one may consider what happens if different fluid occupy different parts of the pore space (patchy saturation), and how this may influence the seismic response. Varying oil-water contacts and gas-oil contacts could also be considered, in terms of simulating variations in reservoir conditions during production, and possibly establishing seismic characteristics related to this.

Anisotropy

The assumption of an isotropic medium made in this thesis does not necessarily reflect a realistic representation of a carbonate paleokarst reservoir. Anisotropy should therefore be considered in future related studies. Vertical or horizontal distribution of aligned fracture sets, representing a simple case of anisotropy called transverse isotropy, might be a good starting point for studying such anisotropy effects (Xu and Payne, 2009).

AVO

As previously discussed, AVO needs to be addressed in future studies related to the modelling workflow presented in this thesis. The introduction of S-wave velocity that comes with non-zero incident angles will have an impact on the seismic response.

Forecasting production behaviour

By considering a detailed input model, complex and realistic scenarios in terms of rock physics parameters with varying fluid contacts and/or fluid substitution, includ-

ing AVO effects, to provide a helpful guideline in forecasting production behaviour in a very complex reservoir type such as paleokarst reservoirs.

Bibliography

Adam, L., Batzle, M., and Brevik, I. (2006). Gassmann's fluid substitution and shear modulus variability in carbonates at laboratory seismic and ultrasonic frequencies. *Geophysics*, 71(6):F173–F183.

Agersborg, R., Johansen, T. A., and Jakobsen, M. (2008). Velocity variations in carbonate rocks due to dual porosity and wave-induced fluid flow. *Geophysical Prospecting*, 57(1):81–98.

Avseth, P., Johansen, T. A., Bakhorji, A., and Mustafa, H. M. (2014). Rock-physics modeling guided by depositional and burial history in low-to-intermediate-porosity sandstones. *GEOPHYSICS*, 79(2):D115–D121.

Avseth, P., Mukerji, T., Mavko, G., and Dvorkin, J. (2010). Rock-physics diagnostics of depositional texture, diagenetic alterations, and reservoir heterogeneity in high-porosity siliciclastic sediments and rocks — A review of selected models and suggested work flows. *GEOPHYSICS*, 75(5):75A31–75A47.

Berryman, J. G. (1992). Single-scattering approximations for coefficients in biot's equations of poroelasticity. *The Journal of the Acoustical Society of America*, 91(2):551–571.

Boggs, S. (2006). *Principles of sedimentology and stratigraphy*. Pearson Prentice Hall, Upper Saddle River, N.J, 4th ed edition.

Bredesen, K. (2012). Use of inverse rock physics modeling in reservoir characterization. Master's thesis, Department of Earth Science, University of Bergen.

Chopra, S. and Castagna, J. P. (2014). *AVO*. Society of Exploration Geophysicists.

Choquette, P. W. and Pray, L. C. (1970). Geologic Nomenclature and Classification of Porosity in Sedimentary Carbonates. *AAPG Bulletin*, 54(2):207–250.

Claerbout, J. F. (1985). *Imaging the earth's interior*. Blackwell, Oxford.

Coe, A. L., editor (2003). *The sedimentary record of sea-level change*. Open University ; Cambridge University Press, Milton Keynes, U.K. : Cambridge, U.K.

Decker, L., Janson, X., and Fomel, S. (2015). Carbonate reservoir characterization using seismic diffraction imaginga. *Interpretation*, 3(1).

Dvorkin, J. and Nur, A. (1996). Elasticity of high-porosity sandstones: Theory for two North Sea data sets. *GEOPHYSICS*, 61:1363 – 1370.

Elvebakk, G., Hogstad, K., Hunt, D. W., Pajchel, J., Rafaelsen, B., and Robak, H. (2003). Upper Carboniferous-Lower Permian Gipsdalen Group karstified reservoir carbonates of the Loppa High, Barents Sea; reservoir po. page 4, Ålesund, Norway.

Ford, D. and Williams, P. D. (2013). *Karst Hydrogeology and Geomorphology*. John Wiley & Sons.

Fossen, H. (2008). *Geologi. Stein, mineraler, fossiler og olje*. Fagbokforlaget.

Furnée, J. P. (2015). Geo-modelling and fluid flow simulation in paleokarst reservoirs. Master's thesis, University of Bergen, Department of Physics and Technology/Department of Earth Science, Uni Research, Centre for Integrated Petroleum Research.

Gallay, M., Hochmuth, Z., Kaňuk, J., and Hofierka, J. (2016). Geomorphometric analysis of cave ceiling channels mapped with 3-D terrestrial laser scanning. *Hydrology and Earth System Sciences*, 20(5):1827–1849.

Gassmann, F. (1951). Elastic waves through a packing of spheres. *Geophysics*, 16(4):673–685.

Gelius, L.-J. . and Johansen, T. A. . (2012). *Petroleum Geophysics, 2nd ed.* UniGEO, Bergen.

Gjøystdal, H., Iversen, E., Laurain, R., Lecomte, I., Vinje, V., and Åstebøl, K. (2002). Review of Ray Theory Applications in Modelling and Imaging of Seismic Data. *Studia Geophysica et Geodaetica*, 46(2):113–164.

Herron, D. A. (2011). *First steps in seismic interpretation*, volume nr. 16 of *Geophysical monograph series*. Society of Exploration Geophysicists, Tulsa, Okla.

Holtz, M. H. and Kerans, C. (1992). Characterization and categorization of West Texas Ellenburger reservoirs. In Candelaria, M. P. and Reed, C. L., editors, *Paleokarst, karst related diagenesis and reservoir development: examples from Ordovician-Devonian age strata of West Texas and the Mid-Continent: Permian Basin Section*, pages 31–44. SEPM Publication No. 92-33.

Hunt, D., Elvebakk, G., Rafaelsen, B., Pajchel, J., Hogstad, K., Robak, H., and Randen, T. (2003). Palaeokarst Recognition & 3d Distribution – New Insights from the Upper Palaeozoic, Loppa High, Barents Sea.

James, N. P. and Choquette, P. W. (1988). *Paleokarst*. Springer Science & Business Media.

Janson, X. and Fomel, S. (2011). 3-D Forward Seismic Model of an Outcrop-Based Geocellular Model. In Martinsen, O. J., Pulham, A. J., Haughton, P. D., and Sullivan, M. D., editors, *Outcrops Revitalized: Tools, Techniques and Applications*. SEPM Society for Sedimentary Geology.

Kearey, P., Brooks, M., and Hill, I. (2013). *An Introduction to Geophysical Exploration*. 3rd ed. Blackwell Science, Oxford.

Lauritzen, S.-E., Hestangen, H., Skutlaberg, S. M., and Øvrevik, R. (2005). The grønli-seter cave research project, rana, north norway. In *Proceedings of the 14th International Congress of Speleology, Athen-Kalamos, August 2005*, pages 1–6.

Lauritzen, S.-E. and Lundberg, J. (2000). 6.1. Solutional and Erosional Morphology. *Speleogenesis: Evolution of Karst Aquifers*, pages 408–436.

Lecomte, I. (2008). Resolution and illumination analyses in PSDM: A ray-based approach. *The Leading Edge*, 27(5):650–663.

Lecomte, I., Lavadera, P. L., Anell, I., Buckley, S. J., Schmid, D. W., and Heeremans, M. (2015). Ray-based seismic modeling of geologic models: Understanding and analyzing seismic images efficiently. *Interpretation*, 3(4):SAC71–SAC89.

Lecomte, I., Lavadera, P. L., Botter, C., Anell, I., Buckley, S. J., Eide, C. H., Grippa, A., Mascolo, V., and Kjoberg, S. (2016). 2(3)D convolution modelling of complex geological targets beyond – 1d convolution. *First Break*, 34(5):99–107.

Ledsaak, K. (2016). Geo_modelling of paleokarst reservoirs - from cave-survey to geocellular paleokarst model. Master's thesis, University of Bergen, Department of Earth Science.

Lønøy, A. (2006). Making sense of carbonate pore systems. *AAPG Bulletin*, 90(9):1381–1405.

Loucks, R. G. (1999). Paleocave carbonate reservoirs: Origins, burial-depth modifications, spatial complexity, and reservoir implications. *AAPG bulletin*, 83(11):1795–1834.

Loucks, R. G. (2007). A review of coalesced, collapsed-paleocave systems and associated suprastratal deformation. *Acta Carsologica*, 36(1).

Lucia, F. J. (1992). Carbonate Reservoir Models: Facies, Diagenesis, and Flow Characterization: Part 6. Geological Methods. 95:269–274.

Mavko, G., Mukerji, T., and Dvorkin, J. (2009). *The rock physics handbook: tools*

for seismic analysis of porous media. Cambridge University Press, Cambridge, UK ; New York, 2nd ed edition.

McDonnell, A., Loucks, R. G., and Dooley, T. (2007). Quantifying the origin and geometry of circular sag structures in northern fort worth basin, texas: Paleocave collapse, pull-apart fault systems, or hydrothermal alteration? *AAPG bulletin*, 91(9):1295–1318.

Melville, P., Al Jeelani, O., Al Menhali, S., and Grötsch, J. (2004). Three-dimensional seismic analysis in the characterization of a giant carbonate field, onshore abu dhabi, united arab emirates.

Målbakken, T. (2009). Paleocaves and collapse breccias in the Franklin Mountains; implications for paleokarst reservoirs. Master's thesis, Department of Earth Science, University of Bergen.

Moore, C. (2001). *Carbonate Reservoirs: Porosity Evolution and Diagenesis in a Sequence Stratigraphic Framework*. Developments in Sedimentology. Elsevier Science.

Mylroie, J. E. and Carew, J. L. (1990). The flank margin model for dissolution cave development in carbonate platforms. *Earth Surface Processes and Landforms*, 15(5):413–424.

Rabbel, O., Galland, O., Mair, K., Lecomte, I., Senger, K., Spacapan, J. B., and Manceda, R. (2018). From field analogues to realistic seismic modelling: a case study of an oil-producing andesitic sill complex in the Neuquén Basin, Argentina. *Journal of the Geological Society*, 175(4):580–593.

Rasolofosaon, P., Lucet, N., and Zinszner, B. (2008). Petroacoustics of carbonate reservoir rocks. *The Leading Edge*, 27(8):1034–1039.

Ringrose, P. and Bentley, M. (2015). *Reservoir Model Design: A Practitioner's Guide*. Springer Netherlands.

Sayago, J., Di Lucia, M., Mutti, M., Cotti, A., Sitta, A., Broberg, K., Przybylo, A., Buonaguro, R., and Zimina, O. (2012). Characterization of a deeply buried paleokarst terrain in the Loppa High using core data and multiattribute seismic facies classification. *AAPG Bulletin*, 96(10):1843–1866.

Sayers, C. M. (2008). The elastic properties of carbonates. *The Leading Edge*, 27(8):1020–1024.

Setså, R. (2018). Olje fra karst. Retrieved from `http://www.geoforskning.no/nyheter/olje-og-gass/1715-olje-fra-karst`.

Simm, R. and Bacon, M. (2014). *Seismic Amplitude : An Interpreter's Handbook*. Cambridge University Press, Cambridge.

Smith, T. M., Sondergeld, C. H., and Rai, C. S. (2003). Gassmann fluid substitutions; a tutorial. *Geophysics*, 68(2):430–440.

Stemmerik, L., Elvebakk, G., and Worsley, D. (1999). Upper Palaeozoic carbonate reservoirs on the Norwegian arctic shelf; delineation of reservoir models with application to the Loppa High. *Petroleum Geoscience*, 5(2):173–187.

Vanorio, T., Scotellaro, C., and Mavko, G. (2008). The effect of chemical and physical processes on the acoustic properties of carbonate rocks. *The Leading Edge*, 27(8):1040–1048.

Wang, Z. (1997). Seismic properties of carbonate rocks. *Carbonate seismology*, 6:29–52.

Wang, Z. Z. (2001). Fundamentals of seismic rock physics. *GEOPHYSICS*, 66(2):398–412.

White, E. L. and White, W. (1969). Processes of cavern breakdown. *National Speleological Society Bulletin*, 31(4):83–96.

Wilson, J. L. (1975). *Carbonate Facies in Geologic History*. Springer Science & Business Media.

Xu, C., Di, B., and Wei, J. (2016). A physical modeling study of seismic features of karst cave reservoirs in the Tarim Basin, China. *GEOPHYSICS*, 81(1):B31–B41.

Xu, S. and Payne, M. A. (2009). Modeling elastic properties in carbonate rocks. *The Leading Edge*, 28:66–74.

Zeng, H., Loucks, R., Janson, X., Wang, G., Xia, Y., Yuan, B., and Xu, L. (2011a). Three-dimensional seismic geomorphology and analysis of the Ordovician paleokarst drainage system in the central Tabei Uplift, northern Tarim Basin, western China. *AAPG Bulletin*, 95(12):2061–2083.

Zeng, H., Wang, G., Janson, X., Loucks, R., Xia, Y., Xu, L., and Yuan, B. (2011b). Characterizing seismic bright spots in deeply buried, Ordovician Paleokarst strata, Central Tabei uplift, Tarim Basin, Western China. *GEOPHYSICS*, 76(4):B127–B137.